Temporal Reflection of Optical Pulses on a Moving Boundary

by

Junchi Zhang

Submitted in Partial Fulfillment of the

Requirements for the Degree

Doctor of Philosophy

Supervised by

Professor Govind P. Agrawal

The Institute of Optics

Arts, Sciences and Engineering

Edmund A. Hajim School of Engineering and Applied Sciences

University of Rochester

Rochester, New York

2024

Table of Contents

Biographical Sketch

The author was born in Wuhan, Hubei Province, China. He attended Tsinghua University and graduated with a Bachelor of Engineering degree in Measurement & Control Technology and Instrument. He began doctoral studies in Optics at the University of Rochester in 2019. He was awarded a Horton Fellowship in 2023. He pursued his research in nonlinear fiber optics under the direction of Prof. Govind P. Agrawal.

The following publications were a result of work conducted during doctoral study:

Junchi Zhang, William R. Donaldson, and Govind P. Agrawal. Temporal reflection and refraction of optical pulses inside a dispersive medium: an analytic approach. J. Opt. Soc. Am. B, 38(3):997–1003, 2021.

Junchi Zhang, William R. Donaldson, and Govind P. Agrawal. Time-domain Fabry–Perot resonators formed inside a dispersive medium. J. Opt. Soc. Am. B, 38(8):2376–2382, 2021.

Junchi Zhang, William R. Donaldson, and Govind P. Agrawal. Impact of the boundary's sharpness on temporal reflection in dispersive media. Optics Letters, 46(16):4053–4056, 2021.

Junchi Zhang, William R. Donaldson, and Govind P. Agrawal. Temporal reflection of an optical pulse from a short soliton: impact of Raman scattering. J. Opt. Soc. Am. B, 39(7):1950–1957, 2022.

Sergey A. Ponomarenko, Junchi Zhang, and Govind P. Agrawal. Goos - Hänchen shift at a temporal boundary. Physical Review A, 106(6):L061501, 2022.

Junchi Zhang, William R. Donaldson, and Govind P. Agrawal. Raman-induced mode coupling in temporal waveguides formed by short solitons. Physical Review A, 107(3):033512, 2023.

Junchi Zhang, William R. Donaldson, and Govind P. Agrawal. Experimental observation of a Raman-induced temporal waveguide. Physical Review A, 107(6):063518, 2023.

Junchi Zhang, William R. Donaldson, and Govind P. Agrawal. Probing the decelerating trajectory of a Raman soliton using temporal reflection. Optics Express, 31(17):27621–27632, 2023.

Conference presentations:

Junchi Zhang, William R Donaldson, and Govind P Agrawal. Theory and Applications of Temporal Reflection in a Dispersive Medium, CLEO, San Jose, CA, May 2022

Junchi Zhang, William R Donaldson, and Govind P Agrawal. Impact of Raman Scattering on Temporal Reflection from a Short Soliton, Frontier in Optics, Rochester, NY, Oct. 2022

Junchi Zhang, William R Donaldson, and Govind P Agrawal. Generalized Energy Conservation Relation in a Space-Time Varying Medium, CLEO, San Jose, CA, May 2023

Junchi Zhang, William R Donaldson, and Govind P Agrawal. Impact of Raman scattering on temporal reflection at a solitonic boundary, Frontier in Optics, Tacoma, WA, Oct. 2023

Junchi Zhang, William R Donaldson, and Govind P Agrawal. Using Temporal Reflection for Probing the Trajectory of Raman Solitons inside a Photonic Crystal Fiber, CLEO, Charlotte, NC, May 2024

Acknowledgments

I'm very grateful to my advisor Prof. Govind Agrawal, who has guided me through the past five years with his expertise. I have benefited much from useful discussions with him.

Prof. William Donaldson, as my supervisor at the Laboratory for Laser Energetics, has helped me significantly during my experiments. I learned most of the experimental techniques from him and my experiments would not have been successful without him.

I would like to thank the final member of my thesis committee, Prof. William Renninger, for useful discussions.

I am also grateful for several scientists at the Laboratory for Laser Energetics. I would like to thank Dr. Jeremy Pigeon for providing me with some components for my experiments, as well as for insightful discussions. Robert Cuffney helped me prepare the photonic crystal fiber used in my experiments. I would also like to thank my colleagues and friends, including Luis Cortes Herrera, Wendao Xu, Yihan Liu, and Jing Cheng, for the useful discussion on both theory and experiments.

Finally, I would like to thank my parents for their support that helped me get through multiple difficulties encountered during my PhD program. They have both given me invaluable advice for my career and life.

Abstract

The temporal analog of the reflection of optical beams from a spatial boundary is an interesting scientific topic. A spatial boundary is an interface across which the refractive index changes in space. An optical beam, hitting such an interface, generates a reflected beam that travels backward. It turns out that there is a temporal analog of this effect that happens for optical pulses instead of spatial beams. When a moving boundary of index change is created in a dispersive medium, an optical pulse can interact with this boundary and undergo a temporal analog of spatial reflection.

In this thesis, I performed theoretical as well as experimental studies on this novel effect. I studied the temporal reflection's dependence on the moving boundary's properties and proposed several interesting phenomena, such as a temporal analog of focusing and collimation for optical pulses. Experimentally, using the optical Kerr effect to create a moving boundary by sending a strong pump pulse, I observed the temporal reflection of a weak probe pulse from the moving boundary in an optical fiber. Interesting effects were observed and studied, such as the trapping of a probe pulse by the pump pulse and probing the trajectory of the pump pulse through temporal reflection.

Contributors and Funding Sources

This work was supported by a dissertation committee consisting of Professor Govind Agrawal and Professor William Renninger of the institute of Optics and Dr. William Donaldson of the Laboratory for Laser Energetics.

This material is based upon work supported by the National Science Foundation under award number ECCS-1933328, and the Department of Energy [National Nuclear Security Administration] University of Rochester "National Inertial Confinement Program" under award number DE-NA0004144.

This report was prepared as an account of work sponsored by an agency of the U.S. Government. Neither the U.S. Government nor any agency thereof, nor any of their employees, makes any warranty, express or implied, or assumes any legal liability or responsibility for the accuracy, completeness, or usefulness of any information, apparatus, product, or process disclosed, or represents that its use would not infringe privately owned rights. Reference herein to any specfic commercial product, process, or service by trade name, trademark, manufacturer, or otherwise does not necessarily constitute or imply its endorsement, recommendation, or favoring by the U.S. Government or any agency thereof. The views and opinions of authors expressed herein do not necessarily state or reflect those of the U.S. Government or any agency thereof.

List of Figures

Chapter 1

Introduction

1.1 Reflection and Refraction

The phenomena of reflection and refraction of an electromagnetic wave are familiar to everyone. Using optics as an example, in daily life, we see reflections of light wherever some surface is present. The refraction of light happens as the light goes from one transparent medium to another one.

In physics, waves occur in many different contexts, such as acoustic waves, electromagnetic waves, quantum mechanical waves, and so on. In different contexts, the physics of waves shares some important similarities. One important property is that when the medium that it propagates in is homogeneous and time-invariant, the wave propagates in one direction, without changing its direction or velocity. A more sophisticated way of expressing the same idea is that the frequency and the wave-vector of a wave are conserved when the homogeneous, time-invariant medium possesses temporal and spatial translational symmetry.

In the case of reflection and refraction of waves on an interface between two media, the spatial translational symmetry is broken. As a result, the wave-vector of a wave is no longer conserved, and the wave can change its direction during reflection, or it can change its speed as it enters another medium, which is refraction. In all cases, the frequency of the wave is always preserved, as the system is time-invariant. This is indeed consistent with our daily experiences since the color of light does not change when it reflects or refracts through a transparent medium.

1.2 Temporal Analog of Reflection and Refraction

Contrary to the phenomenon of waves interacting with spatial structures, the phenomenon of wave propagation in a time-varying medium is far less familiar. When the medium that the wave propagates in changes its property in time, the time-invariant symmetry is broken, which can lead to a wide variety of novel phenomena. In recent years, there has been a growing research interest in this field. It is believed that a new degree of freedom in the manipulation of waves is possible by controlling the properties of materials in time [1, 2, 3, 4].

One of the most interesting phenomena is the dynamics of a wave interacting with a temporal interface. This topic was first studied back in 1958 by Morgenthaler [5]. A simple version of the problem is as follows: Assuming that an electromagnetic wave is propagating in a homogeneous medium with some constant permittivity and permeability. At some instance of time, the medium's properties are abruptly changed everywhere. What would happen to the wave propagating in the medium? This abrupt change of a medium's properties in time is called a temporal interface, or a temporal boundary. It is a direct analog of a spatial interface between two media, except that the medium property changes with time instead of space. It was found that, in general, when a wave interacts with a temporal boundary, it splits into two waves: one moves in the original direction, while the other moves in the opposite direction. This has been interpreted as the temporal analog of reflection and refraction. Contrary to its spatial counterpart, the reflected and refracted waves have a change in their frequency from that of the incoming wave, but their wave-vectors remain conserved. The reason is that the temporal boundary breaks the time-translational symmetry, but the space-translational symmetry is preserved.

Temporal boundaries have been studied both theoretically and experimentally across many different fields in physics. Theoretically, a variety of novel effects were proposed based on temporal interfaces, such as photonic time crystals [6, 7, 8, 9], temporal antireflection coatings [10] and photon pair production [11, 12]. Experimentally, temporal reflection has been observed for water wave [13], radio frequency wave [14, 15] and ultracold atoms [16]. However, for optical waves, only temporal refraction has been observed in epsilon-near-zero material [17, 18]. The challenge is that for temporal reflection to occur, the medium needs to change its refractive index with a large magnitude (order of unity), within a time scale that needs to be comparable to an optical oscillation period.

In 2015, Plansinis et al. proposed a different type of temporal analog of reflection [19]. Instead of considering a uniform index change that happens everywhere at the same time, here the index change is assumed to be moving at a speed close to the speed of light. We can imagine that there is a boundary of index change that is moving. It was found that reflection and refraction also take place when an input pulse, traveling at a different speed, collides with this moving boundary. In this case, the reflected pulse is still traveling in the forward direction, but its speed is changed because of a large frequency shift from the incident pulse frequency. This is completely different from the temporal reflection mentioned previously where the reflected light travels backwards. It turns out that this type of temporal reflection can be achieved much more easily experimentally. In fact, it was already studied in the field of nonlinear fiber optics as an optical analog of the event horizon of a black hole [20, 21, 22]. Experimentally, it is possible to create a moving index change by injecting a strong pump pulse, which increases the refractive index through the optical Kerr effect. The index change only happens over the duration of the pump pulse, i.e., the index change forms a boundary that co-propagates with the pump pulse. A weak probe pulse is then injected into the medium, and it can go through temporal reflection as it interacts with the index change created by the pump pulse.

During my PhD study, my research focused on extending the work of Plansinis [19] about the temporal reflection of light at a moving boundary of index change. I was involved in both the theory and experiments on temporal reflection, with emphasis on temporal reflection in optical fibers using the pump-probe scheme mentioned above. A large portion of my work focused on the dynamics of the temporal reflection of light on a boundary whose speed changes as it propagates. Compared to the temporal reflection with a boundary moving at a constant speed, a number of novel

and interesting effects, such as temporal pulse trapping, temporal pulse focusing and collimation, were discovered and explored.

1.3 Thesis Outline

In Chapter 2, I provide the mathematical formulation of the theory of temporal reflection. The two kinds of temporal reflections mentioned previously are analyzed, showing their similarities and differences. A model of pulse propagation in optical fibers is also given as a valuable tool for describing the temporal reflection in optical fibers. The numerical simulation techniques are also given.

In Chapter 3, I start from the simplest case of temporal reflection of waves at an ideally sharp boundary (shape given by a step function) and analytically derive the coefficients of reflection and transmission. A temporal version of the Goos-Hänchen shift is analyzed with the analytical results. Then, with a semi-analytical method, I perform analysis of temporal reflection at boundaries with shapes other than a step function, showing the effect of the boundary's sharpness on the reflectivity. I also use this method to discuss the possibility of a time-domain Fabry-Perot resonator for frequency shifting.

In Chapter 5, I consider the more realistic situation of temporal reflection in an optical fiber, using the pump-probe method. Here, I include the higher-order nonlinear effect that can affect the pump pulse propagation. It was found that the Raman effect of the fiber causes a continuous deceleration of the pump pulse, resulting in a constantly decelerating boundary. I discuss the novel effects such as temporal focusing, defocusing and collimation that take place as a probe pulse reflects off the decelerating boundary.

In Chapter 6, I consider a temporal waveguide formed by two pump pulses. Such temporal waveguide can trap a short probe pulse, which propagates without broadening from dispersion [23, 24]. The deceleration of the pump pulses produces a decelerating temporal waveguide. An analytical theory is developed for studying the temporal mode coupling dynamics of such a decelerating temporal waveguide.

In Chapter 7, I discuss the experimental work on temporal reflection. I use a photonic crystal fiber as the platform for achieving this effect, using the pump-probe scheme. The pump pulse forms a decelerating boundary as described in Chapter 5, and we experimentally show that this decelerating boundary leads to a trapping of the probe pulse. We observed a large wavelength shift (tens of nanometers) of the probe pulse with a high efficiency.

In Chapter 8, we utilize the temporal reflection effect as a way of probing the decelerating boundary itself. Here, we are interested in the space-time trajectory of this decelerating boundary. It is found that by performing the temporal reflection of a probe pulse on different parts of the boundary, and measuring the reflected pulse, it is possible to deduce the trajectory of the boundary. We also study further how the dynamics of the index boundary affects the temporal reflection. We show that by adjusting the parameters of the input pump pulse, the evolution of the pump pulse can be significantly affected. We observe a significant change in the temporal reflection when a probe pulse reflects off the pump pulse. Such change is analyzed both numerically and experimentally, showing a reasonably good agreement. We believe this technique can be developed as a diagnostic tool for complex nonlinear pulse propagation problems.

Chapter 2

Theoretical Background

In this chapter, I provide the theoretical background of the phenomenon of temporal reflection, as well as suitable models for studying the propagation of pulses in optical fibers, which are used as a platform for our experiments on temporal reflection. Some numerical simulation techniques are also described.

2.1 Maxwell's Equations

In general, the propagation of electromagnetic waves is governed by Maxwell's equations:

$$\begin{aligned} \nabla \cdot \mathbf{D} &= \rho \\ \nabla \cdot \mathbf{B} &= 0 \\ \nabla \times \mathbf{E} &= -\frac{\partial \mathbf{B}}{\partial t} \\ \nabla \times \mathbf{H} &= \mathbf{J} + \frac{\partial \mathbf{D}}{\partial t}. \end{aligned} \tag{2.1}$$

The charge density ρ and the current density $\mathbf{J}$ are both from the contributions of free carriers. Here, we assume that these two quantities vanish since we are considering a dielectric material.

The material properties are usually given phenomenologically by the constitutive relations:

$$\mathbf{D} = \varepsilon \mathbf{E} \ , \mathbf{B} = \mu \mathbf{H}. \tag{2.2}$$

The permittivity ε and permeability μ determine how the medium responds to the electric and magnetic fields by generating polarization and magnetization.

2.2 Temporal Boundary

We first introduce the simplest kind of temporal reflection with an ideally sharp temporal boundary. This problem was originally studied by Morgenthaler [5], and also discussed later by Mendonça

[25], and Xiao et al. [26] among other researchers. In this simple case, the material's dispersion is neglected, assuming that the response of the medium is instantaneous. To form a temporal boundary, the parameters ε and μ are both functions of time t. Physically, we assume that somehow, the material properties can change with time. Experimentally, this change is caused by an external modulation. For example, for a regular optical medium such as glass, the optical Kerr effect can increase the refractive index of the medium by sending in an external pump beam [27, 28]. In some crystals with non-centrosymmetric crystalline structures (such as lithium niobate), such modulation can also be created via the electro-optical effect by sending in an external radio-frequency wave. In the simple case of an ideal sharp temporal boundary, we assume that the material's properties go through a sudden change everywhere simultaneously:

$$\varepsilon(t) = \begin{cases} \varepsilon_1, \text{ for } t < 0 \\ \varepsilon_2, \text{ for } t > 0 \end{cases}, \ \mu(t) = \begin{cases} \mu_1, \text{ for } t < 0 \\ \mu_2, \text{ for } t > 0 \end{cases}. \tag{2.3}$$

Here we assume that the change in medium properties occurs at time $t = 0$. To calculate the changes of the electromagnetic wave at this temporal boundary, we need to use the boundary conditions of Maxwell's equations. However, it is important to keep in mind that the boundary conditions are different from the case of a spatial boundary. In the spatial case, the boundary conditions require that the transverse components of $\mathbf{E}$ and $\mathbf{H}$ along the spatial boundary are continuous [29]. For the temporal boundary considered here, this is not the case. One notices that Maxwell's equations Eq. (2.1), contain time derivatives of $\mathbf{D}$ and $\mathbf{B}$. For the equations to make physical sense, we require that these two time derivatives are finite. This requires that $\mathbf{D}(t) = \varepsilon(t)\mathbf{E}(t)$ and $\mathbf{B}(t) = \mu(t)\mathbf{H}(t)$ are continuous when ε and μ are suddenly changed. Clearly, $\mathbf{E}$ and $\mathbf{H}$ are going to experience sudden jumps at the temporal boundary.

With the boundary conditions, it is relatively straightforward to calculate the changes in a wave interacting with this temporal boundary. For simplicity, we consider an x-polarized wave propagating in the z-direction. Before the change in the medium, the wave propagates unaffected, so the electric and magnetic fields can be written as:

$$\text{for } t < 0\text{: } \begin{cases} E_x(z,t) = E_0 e^{i(kz-\omega_1 t)} \\ H_y(z,t) = \dfrac{E_0}{\eta_1} e^{i(kz-\omega_1 t)} \end{cases} \tag{2.4}$$

Here $\eta_1 = \sqrt{\mu_1/\varepsilon_1}$ is the impedance of the medium before the temporal boundary. The frequency and wave number of the wave are related by the refractive index of the medium: $\omega_1 = k/\sqrt{\varepsilon_1\mu_1}$. Note that we are using the standard notion of complex electric and magnetic fields. It should be kept in mind that only the real part of the complex field represents the actual physical field.

At $t = 0$, when switching occurs, the temporal boundary conditions require that $D_x(z, t = 0_+) = D_x(z, t = 0_-) = \varepsilon_1 E_0 e^{i(kz-\omega_1 t)}$ and $B_y(z, t = 0_+) = B_y(z, t = 0_-) = \mu_1 \frac{E_0}{\eta_1} e^{i(kz-\omega_1 t)}$. Thus, after switching, the plane wave still has a wave-vector of k. This is because the temporal boundary does not break the spatial translational symmetry. To match the boundary conditions, we note that there are two solutions of plane waves that have the same wave-vector k. The field after switching ($t > 0$) should consist of a superposition of these two waves:

$$\text{for } t > 0\text{: } \begin{cases} E_x(z,t) = E_r e^{i(kz+\omega_2 t)} + E_t e^{i(kz-\omega_2 t)}, \\ H_y(z,t) = -\dfrac{E_r}{\eta_2} e^{i(kz+\omega_2 t)} + \dfrac{E_t}{\eta_2} e^{i(kz-\omega_2 t)}, \end{cases} \tag{2.5}$$

where $\omega_2 = k/\sqrt{\varepsilon_2\mu_2}$ and $\eta_2 = \sqrt{\mu_2/\varepsilon_2}$. The field here contains two parts: one with a positive frequency ω_2 and the other with a negative frequency $-\omega_2$. The negative frequency simply means that this part of the field propagates in the backward direction. In order to satisfy the temporal boundary conditions, the relation between the electric fields before and after the switching can be derived:

$$\begin{cases} E_r = \frac{1}{2}\left(\frac{\varepsilon_1}{\varepsilon_2} - \sqrt{\frac{\varepsilon_1\mu_1}{\varepsilon_2\mu_2}}\right)E_0 \\ E_t = \frac{1}{2}\left(\frac{\varepsilon_1}{\varepsilon_2} + \sqrt{\frac{\varepsilon_1\mu_1}{\varepsilon_2\mu_2}}\right)E_0 \end{cases} \tag{2.6}$$

Since the field E_r associated with a negative frequency propagates in the backward direction, this wave is called the temporal reflected wave. The field E_t is called the temporal refracted wave since it continues to propagate in the forward direction. Eq. (2.6) thus gives the reflection and refraction coefficients in the temporal case. It is worth noting that both the reflected and refracted waves experience frequency shifts from the incident frequency. This frequency shift is a direct result of the temporal boundary breaking the time-translational symmetry of the system.

Although we have just derived the frequency shifts for the temporal reflection, there is an intuitive way to show this kind of phenomenon graphically. It turns out that the resulting picture is useful in more general situations, applicable to the reflection of a spatial boundary, a temporal boundary, or a moving boundary. We know that a wave propagating in a medium satisfy the dispersion relation, which is a relation between its wave-vector and its frequency. For a 1-dimensional wave propagating in a non-dispersive medium, the dispersion relation is: $\omega = \pm k/\sqrt{\varepsilon\mu}$. The two signs correspond to two directions of propagation. In a graph with ω and k as the two axes, these dispersion relations form two straight lines. Now, consider we have two media separated by some kind of boundary, we would have two sets of dispersion relations, or four lines as shown in Fig. 2.1 (c) and (d) for the spatial and temporal boundaries shown in part (a) and (b). Here, the blue lines are the dispersion lines of the medium that the incoming wave is in. The red lines are the dispersion of the medium on the other side of the boundary.

To analyze how the scattering at a boundary works, we first consider a spatial boundary, shown

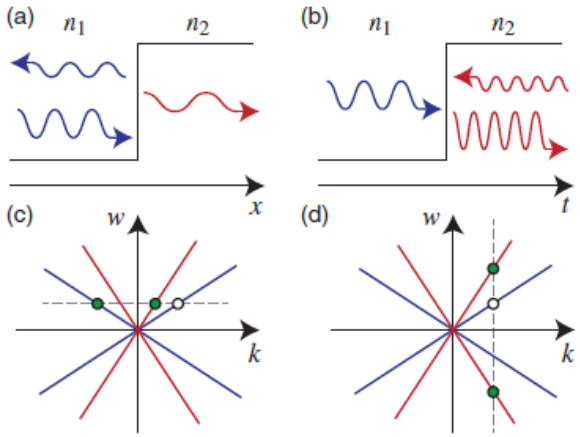

Figure 2.1: This figure is from [1]. (a) and (b) are the schematics showing a spatial reflection and a temporal reflection. (c) and (d) show the dispersion relations of the medium and how the boundary transfer the input wave to the reflected and transmitted waves.

in Fig. 2.1 (a) and (c). As we are all familiar, the spatial boundary does not change the frequency of light. In other words, the frequency of the reflected and transmitted light will have the same frequency as the input light. Suppose we mark down the incident wave on the dispersion diagram as in Fig. 2.1 (c), where the white circle stands for the incident wave. The reflected wave and transmitted wave need to have the same ω. Thus, we simply draw a horizontal line in this diagram, which intersects with both the blue and red dispersion lines, giving 3 crossings. However, only two intersections are physically allowed (the green circles). The intersection with the blue line's backward branch stands for the reflected wave. This is consistent with our experience that a reflected wave should travel backwards, and should remain in the medium that the incident wave comes from. The intersection with the red line gives two intersections, but only the intersection with the forward branch is allowed, which gives the transmitted wave. The intersection with the backward branch is not allowed because an incident wave (that travels towards the boundary) cannot excite a wave on the other side of the boundary that travels towards the boundary. Also see Fig. 2.1 (a) for clarity, there should be no red arrow pointing to the left.

On the other hand, for a temporal boundary, the wave-vector k is now conserved while the frequency is not. Thus, if we want to find the reflected and refracted waves, we need to draw a vertical line and find the intersections as done in Fig. 2.1 (d). This also gives us three intersections. However, in this case, the intersection with the blue line's backward branch is forbidden. This comes from the causality consideration. In the case of a temporal boundary, before the switching, only the incident field exists. A temporal boundary cannot affect the incident field since it happens before the temporal boundary. Thus, in this case, both the reflected and refracted wave exist on the other side of the boundary (green circles in the figure), which is different from the spatial reflection case.

The graphical way of representing the scattering process on the dispersion diagram provides important physical intuitions other than predicting the frequency and wave-vectors of the reflected and transmitted waves. If we take a closer look at the spatial reflection case shown in Fig. 2.1 (c), we can interpret the reflection and refraction as the coupling from the incident state (white circle) to the reflected and transmitted state (green circle). The reflected wave apparently has a larger wave-vector shift from the incident wave. This wave-vector difference comes from the sharp edge of the spatial boundary. It is natural to expect that the edge needs to be sharp enough compared to this wave-vector difference. In other words, if the boundary is not an ideal step-function boundary, but has some spatial extent, this spatial extent needs to be small compared to the wavelength of the wave, so that the reflection can be significant. If the boundary is smooth such that its spatial extent covers many wavelengths of the wave, the reflection will be insignificant. In practice, the spatial boundaries between different materials are indeed very sharp compared to the optical wavelength, and indeed we have significant reflections from those boundaries.

Let us now turn to the temporal case. By analogy with the spatial case, the reflected wave has a large frequency shift from the incident wave, as shown in Fig. 2.1 (d). Note that when evaluating this frequency shift, the reflected wave frequency needs to be taken as negative, as was done in Eq. (2.5). Then, we expect that if the temporal boundary is not an ideal step-function boundary, but it has some rise time, this rise time needs to be small compared to the optical oscillation period in order for the reflection to be significant. This is a key challenge in realizing the temporal reflection experimentally. It is very hard to modulate a material's refractive index at such high speed, and also with a significant index change. The current experimental works are achieved in the low-frequency regions, using the water waves [13], RF waves [14, 15] or cold atoms [16]. For optical

waves, only temporal refractions have been observed in epsilon-near-zero materials [17, 18], which takes advantage of a large relative index change.

Here, I have provided a very basic introduction to the temporal reflection effect. A large amount of work has been done in this area. For example, the treatment of dispersion in a time-dependent medium has been considered by Solís et al. [30] and Hayran et al. [31]. The quantum optical formalism of temporal reflection has also been discussed by Mendonça et al. [11] and Prain et al. [12], showing that such temporal reflection can produce entangled photon pairs (in the forward and backward direction) from the vacuum. Further, the idea of using periodic temporal modulation to form a photonic time crystal has been a hot research topic [6, 7, 8, 9]. There are also some excellent reviews on the topic of photonics of a time-varying medium [1, 2, 3].

2.3 Moving Boundary and Dispersion

In this section, we discuss the phenomena that can happen in the case of a moving boundary, while including the effects of material dispersion.

In the previous sections, we focused on two types of boundaries: a spatial boundary and a temporal boundary. In fact, these two boundaries are special cases of a moving boundary. Suppose the medium is being modulated by some kind of external traveling wave moving with velocity v_b, then the medium refractive index can be expressed as:

$$n(z,t) = n\Big(t - \frac{z}{v_b}\Big). \tag{2.7}$$

A spatial boundary can be obtained by setting $v_b = 0$, while a temporal boundary can be obtained by setting $v_b = \infty$.

Suppose we have an electromagnetic wave traveling in the medium but with a speed different from v_b. This wave is referred to as the incident wave. Then, the incident wave can collide with the moving boundary. The interesting question is then, what kind of waves would be generated after the wave has interacted with this moving boundary? This case is different from the purely spatial and temporal boundaries because the moving boundary breaks both the spatial and temporal translational symmetry. As a result, we would expect that both the wave-vector and frequency are not conserved during the interaction. Instead, we need to consider the boundary conditions, meaning that some quantities need to remain continuous across the boundary. In fact, for the case of a moving boundary, the boundary condition needs to be modified from those used for a purely spatial or temporal boundary [32]. However, the exact forms of the boundary conditions are unimportant if we only wish to calculate the frequencies and wave-vectors of the waves generated from the incident wave colliding with the moving boundary.

For an incident plane wave (with wave-vector k_i and frequency ω_i), the waves generated from the collision are also plane waves. We denote that the generated waves have wave-vectors k_j and frequency ω_j. Here j is a subscript to denote different generated waves. Thus, all the field quantities (such as electric field and magnetic field) associated with the plane wave j must be proportional to $e^{i(k_j z - \omega_j t)}$. The boundary condition requires that, along the moving boundary, some field quantities need to be continuous across the boundary. This must be true for every point on the moving boundary. Since the field quantities of each wave are proportional to $e^{i(k_j z - \omega_j t)}$,

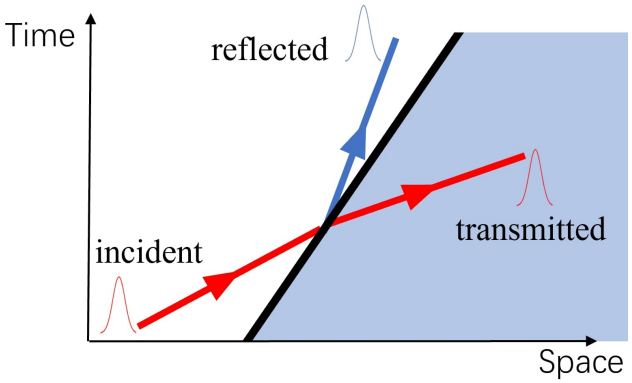

Figure 2.2: Schematic of temporal reflection on a moving boundary with dispersive medium. Both sides are assumed to be dispersive in this figure.

we need to make sure that the phase differences of the different waves must remain the same all along the boundary, otherwise, the boundary condition is impossible to satisfy at every point on the boundary. This is true both for the waves that are generated on the same side of the boundary as the incident wave, or the waves the are generated on the other side.

We now consider the phase difference between the incident wave and the wave j. The requirement of the phase difference being constant along the boundary can be written mathematically in the following way:

$$d(k_i z - \omega_i t) = d(k_j z - \omega_j t), \text{ for } dz = v_b dt \tag{2.8}$$

After simplification, we obtain the following relation:

$$\frac{\omega_i - \omega_j}{k_i - k_j} = v_b \tag{2.9}$$

This relation is called phase continuity relation [4]. It is very powerful because it applies to boundaries moving at any velocity, with any arbitrary boundary profile, and it also applies to boundaries formed in a dispersive medium. We can easily check that the phase continuity leads to both the frequency conservation in the spatial boundary case, as well as the wave-vector conservation in the temporal boundary case when setting v_b to 0 and ∞ respectively.

Using the phase continuity relation, we can qualitatively understand the temporal reflection, as suggested by Plansinis et al. [19]. Consider that we have a dispersive medium, and within this medium, we create a moving boundary of index change by applying some external modulation. Then, a light pulse in the medium, traveling at some velocity different from this moving boundary, can collide with the boundary. It was found that, if the boundary velocity is close to the speed of light in this dispersive medium, a different kind of reflection can take place. This phenomenon is shown in Fig. 2.2. An incident pulse, traveling faster than the moving boundary, collides with the boundary. After hitting the boundary, the incident pulse splits into two pulses. One penetrates through the boundary, which we call the transmitted pulse. However, the other one does not penetrate through the boundary and it can be thought of as a reflected pulse. The reflected pulse, however, is very different from the temporal reflection in Section 2.2. Here, the reflected pulse still travels in the forward direction, but it slows down so that it moves slower than the boundary. Such an effect is impossible to achieve in a non-dispersive medium, because light can only travel

at the same speed. Here, the reflected pulse has a frequency shift that slows it down because of the medium's dispersion.

We can also analyze this phenomenon with the help of the dispersion diagram and the phase continuity relation in Eq. (2.9). Fig. 2.3 shows this graphically. The physical picture shown in Fig. 2.2 corresponds to Fig. 2.3a. The blue curve represents the dispersion relation of the medium that the incident pulse is in. The red curve is the dispersion on the other side of the boundary. To find the transmitted and reflected waves, we first draw the point that corresponds to the incident wave, as shown by the black circle. Then, from Eq. (2.9), we draw a line that has a slope equal to the velocity of the boundary v_b, which is the dashed line in this figure. Next, we find the intersection of this line with the dispersion curves on both sides of the boundary, giving us in total of 3 intersections. Only two intersections are physically allowed, which are shown by the green circles. The intersection with the original dispersion curve (blue one) is the solution of the reflected wave. As we can see from the figure, it still lies on the forward-moving branch, and also its group velocity ($d\omega/dk$) is smaller than the boundary velocity v_b. These are consistent with the sketch Fig. 2.2. The green circle on the red curve gives the transmitted wave since it lies on the other side of the boundary. The other intersection of the dashed line with the red curve is unphysical since it corresponds to a wave that is traveling slower than the boundary, yet it needs to exist in the blue region in Fig. 2.2. This wave cannot be excited by the incident light given here.

Although this reflection process really involves a spatial-temporal boundary, the author or Ref. [19] still referred to it as a temporal analog of reflection of optical beams, or temporal reflection for short. Thus, I will also use the term temporal reflection for this process. However, it is important to know the difference between this type of temporal reflection with the one that really involves a purely temporal boundary.

In the second type of temporal reflection, there is one phenomenon that is not possible for the reflection at a purely temporal boundary. If the index change created by the moving boundary is large enough, it is possible to achieve a temporal analog of total internal reflection. As shown in Fig. 2.3b, there is no intersection of the dashed line with the red curve. In this situation, the wave

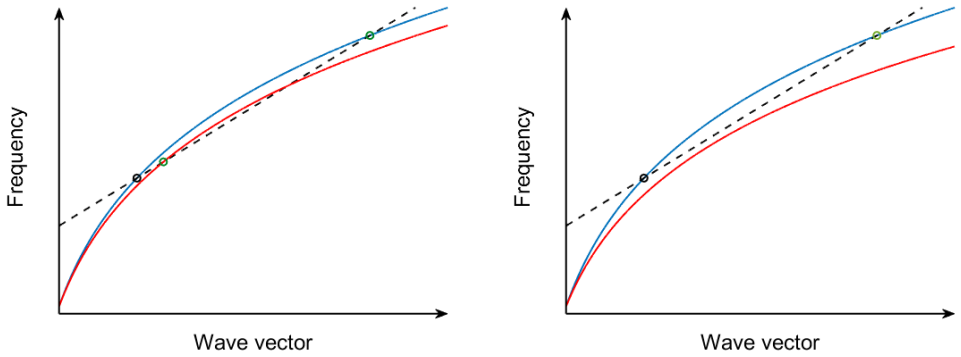

Figure 2.3: Phase continuity relation for moving boundary inside dispersive medium. The blue curve represents the dispersion relation of the medium that the incident pulse is in. The red curve is the dispersion on the other side of the boundary. (a) small index change, transmitted wave exists. (b) large index change, no transmitted wave.

on the other side of the boundary is evanescent, similar to the total internal reflection on a glass-air interface.

Experimentally, it is much easier to achieve the second type of temporal reflection than the one involving a purely temporal boundary. The main reason is that the index change required is small and the boundary does not need to be sharp compared with the optical oscillation frequency. This is because of the possibility of total reflection as shown in Fig. 2.3b. It was estimated in [19] that an index change on the order of 10^{-7} was enough to achieve a total reflection with a large frequency shift of a few THz. Furthermore, when the index change is large enough for total reflection, the reflectivity would always be 1 regardless of the boundary's sharpness. This is because no transmitted state is allowed on the other side of the boundary, so light must be reflected completely, even when the boundary is not sharp. These two reasons show that the extreme requirement of the modulation speed and strength in the case of a purely temporal boundary is not present in this second type of temporal reflection. This is the reason I focused on this type of temporal reflection during my PhD research. From now onward, the term temporal reflection will almost exclusively refer to the type that involves the formation of a moving boundary inside a dispersive medium.

2.4 Pulse Propagation in Optical Fibers

To realize the temporal reflection in practice, silica fibers are commonly used because they exhibit both chromatic dispersion and Kerr nonlinearity. In fact, the phenomenon was first studied in optical fibers as an optical analog of the event horizon of a black hole [20, 21, 22, 33]. For this reason, we discuss the theory of nonlinear pulse propagation in optical fibers in this section.

Optical fibers are waveguides that confine light inside their central core through total internal reflection. An important concept for any waveguide is the mode, which is a specific form of the transverse field distribution that can maintain its shape as it propagates along the waveguide [34]. Usually, only a finite number of modes are supported by a particular waveguide at a specific wavelength of operation. In my research, I focused on achieving temporal reflection in a single-mode waveguide. In a single-mode fiber, the wave propagation is very similar to that of plane waves, making the problem much simpler mathematically.

Here, we consider optical pulses linearly polarized in the x-direction and propagate in the z-direction. The electric field can be written in the form:

$$\mathbf{E}(\mathbf{r},t) = \frac{1}{2}\hat{x}\Big\{F(x,y)A(z,t)\exp[i(\beta_0 z - \omega_0 t)] + c.c.\Big\}. \tag{2.10}$$

We can separate the transverse profile $F(x,y)$ of the mode with its longitudinal profile $A(z,t)$, since we assume that the fiber supports a single mode. We assume that the mode profile does not change much within the bandwidth of the pulse. The rapid oscillation structure of the field is separated out by the factor $\exp[i(\beta_0 z - \omega_0 t)]$, which represents the carrier wave of the pulse. ω_0 is a reference frequency (should be close the the central frequency of the pulse's spectrum), and β_0 is the propagation constant of the fiber at the reference frequency ω_0. The propagation constant serves the same role as the wave-vector k discussed in Section 2.3. The pulse shape is governed by the envelope function $A(z,t)$, which should vary much more slowly compared to the optical period $2\pi/\omega_0$. In general, the propagation of pulses inside an optical fiber is governed by the following

equation [28]:

$$\frac{\partial A}{\partial z}+\sum_{n=1}^{\infty}\frac{i^{n-1}}{n!}\beta_n\frac{\partial^n A}{\partial t^n}+\frac{\alpha}{2}A=N[A], \tag{2.11}$$

where the coefficients $\beta_n=\frac{d^n\beta}{d\omega^n}\Big|_{\omega_0}$ are the dispersion parameters of the fiber. In practice, we perform a polynomial fitting of the measured dispersion relation so that the summation over n is limited to a few terms. α represents the attenuation of the waveguide. On the right side of the equation, $N[A]$ stands for a nonlinear operator on the pulse shape. It depends on the specific type of nonlinearity that affects the propagation of the pulses.

First, it is important to develop some physical intuition for this pulse propagation equation. If the nonlinearity is weak enough that it can be neglected, then Eq. (2.11) can be solved easily in the frequency domain, which leads to the solution:

$$\tilde{A}(z,\omega)=\tilde{A}(0,\omega)\exp[-\frac{\alpha z}{2}+i(\sum_{n=1}^{\infty}\frac{\beta_n}{n!}\omega^n)z]. \tag{2.12}$$

Here, the $\tilde{A}(z,\omega)=\frac{1}{2\pi}\int_{-\infty}^{\infty}A(z,t)\exp(i\omega t)dt$ is the Fourier transform of the pulse shape. Using the relation between the electric field and the envelope function in Eq. (2.10), we obtain the electric field in the frequency domain:

$$\begin{aligned}\tilde{\mathbf{E}}(\mathbf{r},\omega)&=\frac{\hat{x}}{2}F(x,y)\exp(i\beta_0 z)\tilde{A}(z,\omega-\omega_0)\\&=\frac{\hat{x}}{2}F(x,y)\tilde{A}(0,\omega-\omega_0)\exp[-\frac{\alpha z}{2}+i(\beta_0+\sum_{n=1}^{\infty}\frac{\beta_n}{n!}(\omega-\omega_0)^n)z]\\&=\frac{\hat{x}}{2}F(x,y)\tilde{A}(0,\omega-\omega_0)\exp[-\frac{\alpha z}{2}+i\beta(\omega)z],\end{aligned} \tag{2.13}$$

which shows that the electric field with frequency ω propagates with a propagation constant $\beta(\omega)=\beta_0+\sum_{n=1}^{\infty}\frac{\beta_n}{n!}(\omega-\omega_0)^n$, which is what one expects. This means that the terms on the left side of Eq. (2.11) simply describe the linear propagation of the pulses, including the effect of dispersion and losses. In this derivation, we assumed that the envelope $A(z,t)$ has a narrow frequency bandwidth such that the Fourier transforms of the two terms in Eq. (2.10) do not overlap in the frequency domain. This assumption almost always holds for optical fields. For a hyperbolic secant pulse centered at 800 nm with a temporal FWHM of 30 fs, we can find that the total energy of the spectral component that gets overlapped with the other side contains only about 10^{-54} of the total energy. This is completely negligible.

When the pulse intensity is large enough, nonlinear effects must be taken into account, which modifies the pulse propagation equation through the operator $N[A]$. In the case of materials possessing centro-symmetric structures, or amorphous structures, the lowest-order nonlinear effect is the third-order nonlinearity. In the presence of third-order nonlinearity, the electric flux density D in Eq. (2.1), in the linearly polarized case, can be written as:

$$D=\varepsilon E+P_l+P_{nl}=\varepsilon_0(1+\chi^{(1)})E+\varepsilon_0\chi^{(3)}E^3, \tag{2.14}$$

where $\chi^{(n)}$ is the n-th order susceptibility of the medium. The linear susceptibility determines the refractive index of the medium: $n_0=\sqrt{1+\chi^{(1)}}$. If we represent the field as was done in Eq.

(2.10), we can write the nonlinear polarization with the third order nonlinearity in the form:

$$P_{nl} = \frac{\varepsilon_0 \chi^{(3)}}{8}\Big\{F^3(x,y)A^3(z,t)\exp[i(3\beta_0 z - 3\omega_0 t)] + 3|F(x,y)|^2|A(z,t)|^2F(x,y)A(z,t)\exp[i(\beta_0 z - \omega_0 t)] + c.c.\Big\}, \tag{2.15}$$

In this equation, we have a component that oscillates at the frequency of $3\omega_0$, which in principle can excite a third harmonic wave. However, this process requires a phase-matching condition [27], which is generally not satisfied. Thus, we can safely neglect this term and only keep the term that oscillates at frequency ω_0. For this second term, we can write it more compactly by using the connection of the electric field with the intensity:

$$P_{nl} = \frac{3\chi^{(3)}}{2n_0 c} IE \tag{2.16}$$

with the intensity given as $I(\mathbf{r},t) = \frac{1}{2}n_0\varepsilon_0 c|F(x,y)|^2|A(z,t)|^2$. This should be the instantaneous intensity of the field, averaged over multiple optical cycles, but the averaging time is small compared to the time scale of the envelope function A. In the expression above, we can see that the nonlinear polarization has a similar form as the linear polarization, but the susceptibility now has a dependence on the field intensity. Thus, effectively, we have:

$$\chi_{eff} = \chi^{(1)} + \frac{3\chi^{(3)}}{2n_0\varepsilon_0 c} I \tag{2.17}$$

This effective change of the susceptibility leads to an effective refractive index of the medium:

$$\begin{aligned} n_{eff} &= \sqrt{1+\chi_{eff}} \\ &= \sqrt{1+\chi^{(1)} + \frac{3\chi^{(3)}}{2n_0\varepsilon_0 c} I} \\ &= \sqrt{1+\chi^{(1)}} \times \sqrt{1 + \frac{3\chi^{(3)}}{2(1+\chi^{(1)})n_0\varepsilon_0 c} I} \\ &\approx \sqrt{1+\chi^{(1)}} \times (1 + \frac{3\chi^{(3)}}{4(1+\chi^{(1)})n_0\varepsilon_0 c} I) \\ &= n_0 + \frac{3\chi^{(3)}}{4n_0^2\varepsilon_0 c} I \\ &= n_0 + n_2 I, \end{aligned} \tag{2.18}$$

where we define a nonlinear refractive index as $n_2 = \frac{3\chi^{(3)}}{4n_0^2\varepsilon_0 c}$. Thus, the third-order nonlinearity creates an effective change in the refractive index, which is proportional to the intensity of the field. The nonlinear refractive index of silica glass is about 2.6×10^{-20} m^2/W [28].

Since the instantaneous intensity of the field can modify the refractive index of the medium, and also modify the propagation constant of the mode, the nonlinear term on the right-hand side of Eq. (2.11) should take the form of $i\Delta\beta(t)A$. And the propagation constant change $\Delta\beta(t)$ is determined

by the instantaneous intensity of the field. To evaluate the change of the propagation constant from the nonlinear refractive index, one can use the first order perturbation theory. To see this, we can first write the eigenvalue equation that the mode $F(x,y)$ satisfies. Under the weakly-guided approximation, the mode profile satisfies:

$$\beta^2(\omega_0)F = \frac{\partial^2 F}{\partial x^2} + \frac{\partial^2 F}{\partial y^2} + n^2(\omega_0,x,y)\frac{\omega_0^2}{c^2}F, \tag{2.19}$$

where β is the propagation constant of the mode and $n(\omega_0,x,y)$ is the local refractive index. Eq. (2.19) is analogous to the eigenstate problem in quantum mechanics, with the refractive index distribution playing the role of the potential. When the refractive index is changed because of the optical Kerr effect from the intensity of the pulse, this change leads to a perturbation of Eq. (2.19). Using first-order perturbation theory in quantum mechanics [35], the eigenvalue β^2 needs to be corrected with the following expression:

$$(\beta+\Delta\beta)^2 - \beta^2 = \frac{2\omega_0^2}{c^2}\frac{\int n\Delta n|F(x,y)|^2dxdy}{\int |F(x,y)|^2dxdy} \tag{2.20}$$

where $\Delta n(x,y) = n_2 I(x,y)$ is the perturbation of the refractive index. The refractive index $n \approx n_0$ has only a weak dependence on the transverse position (x,y), thus it can be taken out of the integral. The change in the propagation constant $\Delta\beta$ is then given by (to the first order of the perturbation):

$$\begin{aligned}\Delta\beta &= \frac{\omega_0^2 n_0}{c^2\beta}\frac{\int \Delta n|F(x,y)|^2dxdy}{\int |F(x,y)|^2dxdy} \\ &\approx \frac{\omega_0}{c}\frac{\int \Delta n|F(x,y)|^2dxdy}{\int |F(x,y)|^2dxdy}\end{aligned} \tag{2.21}$$

Usually, one would prefer to work in the unit where the field envelope A is defined such that the $|A|^2$ equals the instantaneous power of the light in the mode. Using this convention, the local, instantaneous intensity is given by:

$$I(x,y,z,t) = \frac{|F(x,y)|^2}{\int |F(x,y)|^2dxdy}|A(z,t)|^2. \tag{2.22}$$

Since the change of index is given by $\Delta n(x,y) = n_2 I(x,y)$, substituting Eq. (2.22) into Eq. (2.21), the nonlinear term in Eq. (2.11) is given by:

$$N[A] = i\Delta\beta A = i\gamma(\omega_0)|A|^2A = i\frac{\omega_0 n_2}{cA_{eff}}|A|^2A \tag{2.23}$$

We defined another coefficient $\gamma(\omega_0)$, which is called the nonlinear coefficient of the waveguide. A_{eff} is defined as the effective area of the mode, with the expression:

$$A_{eff} = \frac{(\int\int |F(x,y)|^2dxdy)^2}{\int\int |F(x,y)|^4dxdy} \tag{2.24}$$

Combining Eq. (2.11) and Eq. (2.23) allows us to solve for the pulse propagation dynamics with some given input pulse shape $A(z=0,t)$. This is usually done numerically.

I would like to comment on the derivation of $\Delta\beta$ above. Essentially, we start from an eigenvalue equation Eq. (2.19), and use perturbation theory to calculate the change of the propagation constant using perturbation theory. The eigenvalue equation is obtained by assuming that the field is monochromatic, which is not true for the study of pulse propagation. The justification for the derivation above is that we assumed that the pulse envelope varies much more slowly compared to the optical oscillation cycle. Thus, the derivation above is performed using the quasi-monochromatic assumption, since the change of $\Delta n = n_2 I$ is slow compared to the optical cycle.

We should comment on the physical significance of Eq. (2.23). This term adds a nonlinear phase shift to the pulse. The amount of phase shift depends on the pulse's instantaneous power. For this reason, this effect is often called self-phase modulation. The time-dependent phase created by the self-phase modulation usually results in a spectral broadening of the pulse.

The self-phase modulation term in Eq. (2.23) assumes that the third-order nonlinear response of the medium is instantaneous. This is typically true for the medium's response that comes from the motion of bound electrons. However, another significant contribution comes from molecular vibrations in the medium. These molecular vibrations will provide a delayed response, which turns out to describe the phenomenon of Raman scattering. Raman scattering is an inelastic scattering effect, that can transfer light from a high frequency to a low frequency, or equivalently, the low-frequency component of a pulse experiences a gain from the presence of a high-frequency component. This gain has been measured experimentally as a function of the frequency offset between the two fields [36]. The gain spectrum was used to deduce a response function of the Raman effect, which can be used for modeling pulse propagation in the presence of Raman effect.

Here, I would not go into details of the derivation of the Raman effect's modeling. For details, the reader can turn to Chapter 2 of Ref. [28]. The most general form of the nonlinear operator that goes into the pulse propagation equation is given by:

$$N[A](z,t) = i\gamma(\omega_0)\left(1+\frac{i}{\omega_0}\frac{\partial}{\partial t}\right)\Big((1-f_R)|A(z,t)|^2A(z,t) + f_R A(z,t)\int_0^\infty h_R(t')|A(z,t-t')|^2dt'\Big) \tag{2.25}$$

The expression looks complicated, but we can understand the physical origin of each term. First, we have a nonlinear coefficient $\gamma(\omega_0)$, which comes from the Kerr effect that we derived earlier. The second term in the first bracket containing a time derivative is a correction because the nonlinear coefficient is in general a function of the frequency, and needs to be modified when the pulse bandwidth is large. This term leads to the effect of self-steepening, which is a mechanism that changes the pulse's group velocity based on the intensity, leading to the formation of a steep edge in the pulse shape [37, 38, 39]. In the second bracket, we have two terms that can both be interpreted as the index change of the medium caused by the field intensity. The first term is an instantaneous index change, which comes from the response of bound electrons, as discussed earlier. The second term comes from the molecular contribution, which is non-instantaneous. It is the convolution of the field intensity with a response function $h_R(t)$. The response function is causal, meaning that $h_R(t<0)=0$. For regular silica glass, the response time is on the order of 20-30 fs. For pulses much longer than this time scale, this part of the response can also be regarded as instantaneous.

The response function $h_R(t)$ was determined experimentally by measuring the Raman gain spectrum. There are several approximate formulas that mimic the experimental results [40, 41, 42].

Throughout this thesis, the response function used in the simulations is given by [42]:

$$h_R(t>0) = (1-f_b)(\tau_1^{-2}+\tau_2^{-2})\tau_1 \exp\big(-\frac{t}{\tau_2}\big)\sin\big(\frac{t}{\tau_1}\big) + f_b\frac{2\tau_b - t}{\tau_b^2}\exp\big(-\frac{t}{\tau_b}\big) \tag{2.26}$$

The parameters in this model are: $\tau_1 = 12.2$ fs, $\tau_2 = 32$ fs, $\tau_b = 96$ fs, $f_R = 0.245$, $f_b = 0.21$. Fig. 2.4 shows this response function.

Eq. (2.11), combined with Eq. (2.25) and Eq. (2.26) gives us a complete mathematical model for the simulation of pulses propagating inside optical fibers. However, since the pulse propagates at the speed of light in the fiber, it is important to define a reduced time in the following expression:

$$\tau = t - \beta_1 z, \tag{2.27}$$

where β_1 is the inverse of the group velocity of the mode at ω_0. The time τ is the reduced time. Using τ as the variable for time, we obtain the following equation for the pulse propagation:

$$\frac{\partial A}{\partial z} + \sum_{n=2}^{\infty}\frac{i^{n-1}}{n!}\beta_n\frac{\partial^n A}{\partial \tau^n} + \frac{\alpha}{2}A = N[A](z,\tau) \tag{2.28}$$

The only change is that the β_1 term is eliminated from the equation. The form of the nonlinear operator remains the same since this operator is time-invariant of the input. Eq. (2.28) is the main tool that we used for simulating propagation of pulses in optical fibers.

2.5 Numerical Techniques

The equation that we wish to solve is Eq. (2.28), with a given initial condition $A(z=0,\tau)$. There are many ways to handle this problem. For example, the split-step Fourier method is widely used

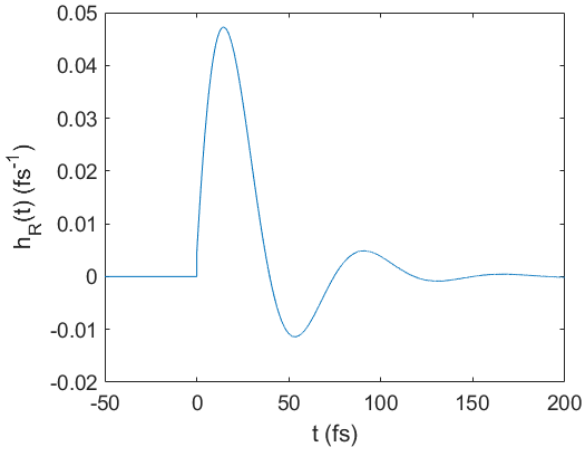

Figure 2.4: Raman response function given by Eq. (2.26).

[28]. During my research, I preferred another method called the 4-th order Runga-Kutta method [43], which is conveniently packaged in MATLAB. Most of the simulations were performed based on the Rung-Kutta method.

Runga-Kutta method is a numerical scheme for integrating a set of ordinary differential equations, from its initial condition. To use this method for solving the pulse propagation equation, we need to discretize the partial differential equation into a set of ordinary differential equations. We found that this is more easily handled in the frequency domain, as the dispersion operators become multiplicative in this domain.

We perform Fourier transform on both sides of Eq. (2.28). Note that this Fourier transform is with respect to the reduced time τ. We obtain:

$$\frac{\partial \tilde{A}(z,\omega)}{\partial z} - i\sum_{n=2}^{\infty}\frac{\beta_n}{n!}\omega^n\tilde{A}(z,\omega) + \frac{\alpha}{2}\tilde{A}(z,\omega) = \mathscr{F}\{N[A]\}(z,\omega). \tag{2.29}$$

It is worth noting that the Fourier domain amplitude $\tilde{A}$ is not equal to the one that we used before, where we performed the Fourier transform with respect to the actual time t.

The equation above can be further simplified by introducing a different variable:

$$\tilde{B}(z,\omega) = \tilde{A}(z,\omega)\exp\Big[\big(\frac{\alpha}{2} - i\sum_{n=2}^{\infty}\frac{\beta_n}{n!}\omega^n\big)z\Big] \tag{2.30}$$

Then, we can rewrite the propagation equation in terms of $\tilde{B}$:

$$\frac{\partial \tilde{B}(z,\omega)}{\partial z} = \mathscr{F}\{N[A]\}(z,\omega)\exp\Big[\big(\frac{\alpha}{2} - i\sum_{n=2}^{\infty}\frac{\beta_n}{n!}\omega^n\big)z\Big] \tag{2.31}$$

Without nonlinearity, $\tilde{B}$ would be stationary. This form of the equation is more easily handled by the differential equation solvers because it removes the fast oscillatory phase (with respect to z) of $\tilde{A}$.

To actually solve the equation numerically, we can discretize the time-axis by sampling within a time window uniformly. This automatically gives us a sampling in the frequency domain, using the algorithm of fast Fourier transform. Thus, the partial differential equation has been transformed into a set of coupled ordinary differential equations for $\tilde{B}(z,\omega_i)$, with $i = 1,2,...,N$, and N is the number of sampling points. The right-hand side of Eq. (2.31) can be evaluated numerically, by transforming $\tilde{B}(z,\omega)$ into $A(z,t)$, and the nonlinear terms are more efficiently evaluated in the time domain. There are many solvers available that can solve for this kind of equation. In my PhD research, I mostly used the function ode45 of MATLAB, which uses an explicit Runga-Kutta (4,5) formula and has the capabilities for adaptive step size adjustment.

Chapter 3

Temporal Reflection Analysis

In this chapter, I provide some analytical and semi-analytical treatments for the temporal reflection in a dispersive medium from a moving boundary. Hopefully, it would provide some intuition of this effect.

3.1 Modeling of a Temporal Boundary

The problem we are considering is already discussed qualitatively in Section 2.3: a pulse is traveling inside a dispersive medium. We apply some external traveling wave modulation, that changes the index of the medium, forming a moving boundary. We consider only a 1-dimensional problem and assume that this index change takes the following form:

$$\Delta n(z,t) = \Delta n(t - z/v_b). \tag{3.1}$$

The index change creates a boundary traveling at the velocity v_b. In this chapter, we assume that this boundary of index change remains the same shape during propagation. Usually, the index profile Δn is constant for t very large or very small. There is a finite transition region where the index change actually takes place. Therefore, we can interpret that this index change creates a boundary of some shape that separates two homogeneous regions.

When the index change is not too large, the interaction of the pulse with the boundary becomes easy to model. In this case, the primary effect of the boundary to the pulse is a phase modulation. Taking the analogy with the self-phase modulation term Eq. (2.23), we can write the pulse propagation equation as:

$$\frac{\partial A}{\partial z} + \sum_{n=1}^{\infty} \frac{i^{n-1}}{n!} \beta_n \frac{\partial^n A}{\partial t^n} + \frac{\alpha}{2} A = iB(t - z/v_b)A. \tag{3.2}$$

We used the same form of the pulse propagation equation as in Eq. (2.11). The nonlinear term is replaced by the phase modulation term caused by the moving boundary. $B = \omega_0 \Delta n/c$ is the change of propagation constant induced by the index change. We will neglect the dispersion that is higher than second order, and also neglect the medium's attenuation. Also, it is useful to redefine a reduced time:

$$\tau = t - z/v_b, \tag{3.3}$$

so that the arrival time of the boundary in this frame is the same at different positions. Using τ as the time variable, the pulse propagation equation can be written:

$$\frac{\partial A}{\partial z} + \Delta\beta_1 \frac{\partial A}{\partial \tau} + \frac{i\beta_2}{2}\frac{\partial^2 A}{\partial \tau^2} = iB(\tau)A, \tag{3.4}$$

where $\Delta\beta_1 = \beta_1(\omega_0) - 1/v_b = 1/v_g(\omega_0) - 1/v_b$, representing the difference between the inverse of the group velocity of the medium at reference frequency ω_0 and that of the moving boundary.

It is worth noting that the reference ω_0 is just an arbitrary frequency that should be close to the actual frequency of the light pulse, such that the Taylor expansion of the dispersion relation at ω_0 makes sense. We will see later how one can choose ω_0 such that the analysis becomes easier. We would also only be discussing the case of $\beta_2 > 0$, since the method here can be applied in the same way to the case of $\beta_2 < 0$.

First, we present a numerical solution of Eq. (3.4) from Ref. [19], to develop some understanding of the phenomenon. In this simulation, an ideal step-like boundary is assumed by taking $B(t)$ to be a Heaviside step function. Fig. 3.1 shows the result. In the reference frame that we use here, the boundary is essentially purely temporal. An incident pulse is sent from one side, which interacts with the boundary and splits into two pulses, a reflected pulse and a transmitted pulse. We can see that in the spectral domain, both pulses are spectrally shifted from the incident pulse. Note that this figure demonstrates the same physics as the sketch showed in Fig. 2.2. The only difference is that here, we are employing a coordinate transformation Eq. (3.3), so that in Fig. 3.1, the boundary appears to be purely temporal. We call this new coordinate a moving frame. We stress that the reflected pulse is not moving backward (one might think so from Fig. 3.1) because the results are shown in a moving frame. Rather, the incident pulse splits into two parts moving at different speeds such that the reflected part never crosses the boundary.

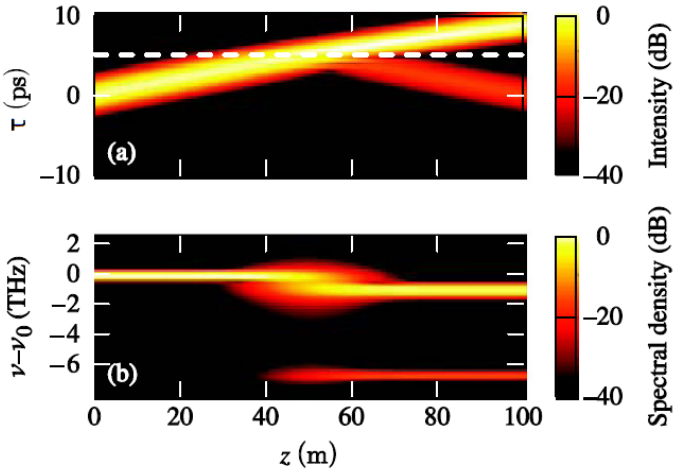

Figure 3.1: Simulation of Eq. (3.4) from [19]. This shows the evolution of an incident pulse interacting with a moving boundary. Top: evolution of the temporal pulse shape. Bottom: evolution of the spectral shape. The white dashed line is the boundary.

3.2 Two Analogies

As we discussed previously, the ω_0 is just some reference frequency to define the pulse envelope, the actual value of this frequency has some arbitrariness. We can choose ω_0 such that the group velocity at this frequency is equal to the velocity of the moving boundary. In this case, $\Delta\beta_1 = 0$ should be satisfied in Eq. (3.4). This simplifies the equation and leads to:

$$\frac{\partial A}{\partial z} + \frac{i\beta_2}{2}\frac{\partial^2 A}{\partial \tau^2} = iB(\tau)A, \tag{3.5}$$

Here, it is instructive to discuss two kinds of analogies that we will use to understand this physical effect. First, we recall that in 1 dimension, the paraxial scalar wave diffraction equation has the following form:

$$\frac{\partial U}{\partial z} - \frac{i}{2k}\frac{\partial^2 U}{\partial x^2} = 0. \tag{3.6}$$

Here U is the beam's envelope. This equation describes the diffraction of beam in free space, or homogeneous medium, and the propagation direction is z and k is the wave-vector in the medium. If there are also some small index variations in the medium, the equation can be modified:

$$\frac{\partial U}{\partial z} - \frac{i}{2k}\frac{\partial^2 U}{\partial x^2} = i\Delta n(z,x)k_0 U. \tag{3.7}$$

It is clear that this equation has the same mathematical form as Eq. (3.5). This suggests an analogy between the physics of beam propagation with pulse propagation. Comparison between Eq. (3.5) with Eq. (3.7) suggests that the pulse propagation is analogous to the beam diffraction (left-hand side of the equation) while the interaction of the pulse with a moving boundary is analogous to the interaction of a beam with a spatial boundary of index change. Such analogy is called space-time duality and it was first discovered in the 1960s [44, 45, 46]. This idea is useful because we can now use the results of the more familiar beam propagation to predict and understand the phenomenon that happens for pulse propagation. There are a number of techniques developed based on this idea, such as frequency to time conversion [47, 48, 49] and time lens [50, 51, 52, 53].

A second analogy to make is that Eq. (3.5) also has the same form as Schrödinger's equation in quantum mechanics, with $B(\tau)$ playing the role of a potential. This allows us to treat the effect of temporal reflection as the analog of quantum scattering in 1-dimension.

3.3 Step-like Boundary

We first analyze the effect when with an ideal step-like boundary. This can be modeled by taking $B(\tau) = \beta_B H(\tau)$, and $H(\tau)$ is the Heaviside step function that takes the value 1 when τ is positive, and 0 when τ is negative. The boundary is assumed to be sharp in this case.

To analyze the temporal reflection of an incident light pulse on this boundary, as shown in Fig. 3.1, we use the analogy of this problem with quantum mechanics. As this problem is analogous to the quantum mechanical scattering of a particle wave on a sharp boundary, we can use the method in the quantum problem [54].

First, we search for the solution of the "time-independent Schrödinger's equation". In our case, we write the solution as $A(z,\tau) = \exp(i\beta' z)A_T(\tau)$. This is possible because equation Eq. (3.5) has translational symmetry in z. Notice that this can be interpreted as the wave-vector conservation in the moving frame. It can be shown that it is equivalent to the phase continuity relation Eq. (2.9) viewed in the laboratory frame. We write the solution for $A_T(\tau)$ as:

$$A_T(\tau) = \begin{cases} e^{-i\delta\tau} + Re^{-i\delta_r\tau}, \text{ for } \tau < 0 \\ T^{-i\delta_t\tau}, \text{ for } \tau > 0. \end{cases} \tag{3.8}$$

Physically, this solution describes an incident plane wave from $\tau < 0$ side towards the moving boundary. The reflection from this boundary results in a reflected wave and a transmitted wave, with amplitudes R and T. Notice that when $\beta_2 > 0$, we require that $\delta > 0$ from Eq. (3.8) so that the incident wave has a group velocity that travels slower than the boundary. Since $A(z,\tau) = \exp(i\beta' z)A_T(\tau)$ satisfies Eq. (3.5), each plane wave component should satisfy the dispersion relation of the medium that it propagates in. This leads to the following equation:

$$\beta' = \frac{\beta_2\delta^2}{2} = \frac{\beta_2\delta_r^2}{2} = \frac{\beta_2\delta_t^2}{2} + \beta_B. \tag{3.9}$$

We can obtain the relation between the frequencies of the three waves:

$$\delta_r = -\delta,\ \delta_t = \sqrt{\delta^2 - \frac{2\beta_B}{\beta_2}}. \tag{3.10}$$

The signs of δ_r and δ_t are chosen such that the reflected and transmitted waves are both traveling away from the boundary.

To find the coefficients R and T, we match the boundary condition at $\tau = 0$ so that both A_T and $\partial A_T/\partial\tau$ are continuous across the boundary. This must be true to avoid infinity in Eq. (3.5). By evaluating A_T and $\partial A_T/\partial\tau$ on two sides of the boundary with A_T given by Eq. (3.8) and making them continuous, we obtain two equations involving R and T. The solution is given by:

$$\begin{aligned} R &= \frac{\delta - \sqrt{\delta^2 - 2\beta_B/\beta_2}}{\delta + \sqrt{\delta^2 - 2\beta_B/\beta_2}} \\ T &= \frac{2\delta}{\delta + \sqrt{\delta^2 - 2\beta_B/\beta_2}} \end{aligned} \tag{3.11}$$

Fig. 3.2 shows the reflection and transmission coefficients at the sharp boundary as a function of input frequency offset $\Delta\nu = \delta/(2\pi)$ from the group velocity matching frequency ω_0. The parameters used here are: $\beta_2 = 5$ ps^2/km and $\beta_B = 0.5$ m^{-1}. This corresponds to an index change of only 8×10^{-8} if the wavelength is at 1 μm. A larger $\Delta\nu$ stands for a larger group velocity mismatch. As we can see, for $\delta < \sqrt{2\beta_B/\beta_2}$, the transmitted field frequency becomes imaginary, meaning that there is no transmitted wave. In this region, the reflectivity is 1 and the transmission coefficient has no clear physical meaning. This is the temporal analog of total internal reflection. When the group velocity mismatch becomes large enough, the total reflection condition does not hold, and then the reflectivity decreases rapidly as the group velocity mismatch becomes even

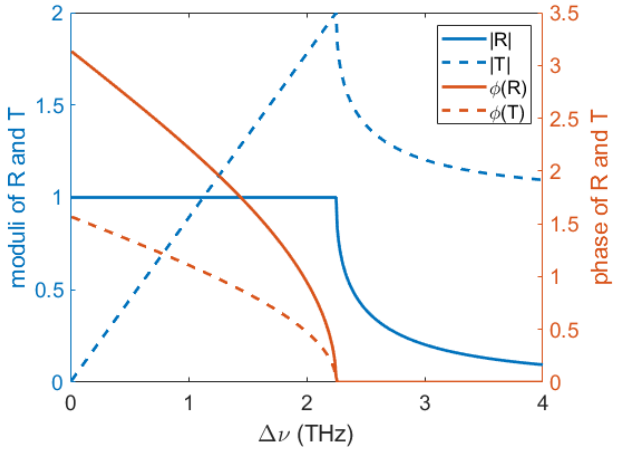

Figure 3.2: Frequency dependence of the reflection and transmission coefficients. Solid and dashed curves show, respectively, the modulus and phase of these two quantities.

larger. It is important that such a small index change is able to induce a large frequency shift through temporal reflection.

The preceding discussion applies to each specific frequency component of a pulse. We can use it to study how an incident pulse gets reflected and transmitted at the temporal boundary. Consider an incident pulse with the slowly varying amplitude:

$$A(z=0,\tau)=A_{in}(\tau). \tag{3.12}$$

We can decompose it into plane waves of different frequencies using the Fourier transform:

$$\tilde{A}_{in}(\delta)=\int A_{in}(\tau)e^{i\delta\tau}d\tau. \tag{3.13}$$

The evolution of each plane-wave component is governed by Eq. (3.8). The total field can be calculated by integrating over the input pulse's spectrum to obtain:

If $\tau < T_B$:

$$A(z,\tau)=\frac{1}{2\pi}\int \tilde{A}_{in}(\delta)e^{i[\beta'(\delta)z-\delta\tau]}d\delta+\frac{1}{2\pi}\int R(\delta)\tilde{A}_{in}(\delta)e^{i[\beta'(\delta)z-\delta_r\tau]}d\delta, \tag{3.14}$$

If $\tau > T_B$:

$$A(z,\tau)=\frac{1}{2\pi}\int T(\delta)\tilde{A}_{in}(\delta)e^{i[\beta'(\delta)z-\delta_t\tau]}d\delta. \tag{3.15}$$

This equation can be used to find the shapes and spectra of the reflected and transmitted parts of any input pulse.

To validate our analytic theory of temporal reflection and refraction, we consider a Gaussian pulse with the amplitude $A_{in}(\tau)=e^{-\frac{1}{2}(\tau/T_w)^2-2\pi i\Delta\nu_i\tau}$ and choose $T_w=1$ ps, and $\Delta\nu_i=3.18$ THz. This pulse is reflected at the boundary located at $T_B=5$ ps as it propagates inside a dispersive medium. We use the same parameters as those used in Fig. 3.2. We solved Eq. (3.5) numerically using the split-step Fourier method [28]. We also used our analytic theory to calculate the reflected and transmitted coefficients as a function of frequency and carry out the integrations in Eqs. (3.14) and (3.15). The results are compared in Fig. 3.3. As is evident, the two methods produce identical results and indicate that our analytical approach is valid.

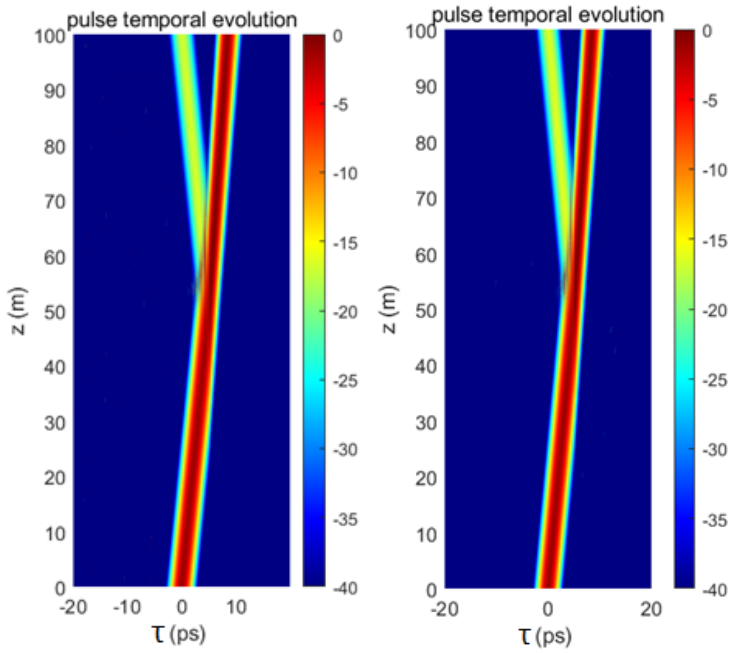

Figure 3.3: Solution of pulse propagation equation Eq. (3.5) using (left) analytical theory Eqs. (3.14) and (3.15), compared with (right) purely numerical solution. The relative power $|A(z,\tau)|^2$ is plotted on a 40dB decibel scale.

3.4 Reflected and Transmitted Pulses

In this section, we investigate the properties of reflected and transmitted pulses produced after a pulse interacts with the moving boundary. The reflected and transmitted pulses can be calculated using Eqs. (3.14) and (3.15). It is not possible to obtain an exact form without approximations.

Consider that the input pulse spectrum $\tilde{A}_{in}(\delta)$ is centered around some value δ_i, and it is relatively narrowband, such that the reflection and transmission coefficients $R(\delta)$ and $T(\delta)$ can be approximated as constants within the input pulse spectrum. Here, we assume that total reflection condition is not satisfied so that R and T are both real. Furthermore, we assume that the transmitted frequency is given by the Taylor expansion of Eq. (3.10) $\delta_t \approx \delta_t(\delta_i) + S(\delta - \delta_i)$, to the first order. $S = (d\delta_t/d\delta)\big|_{\delta=\delta_i}$. Then, we can first calculate the reflected and transmitted pulse shapes at $z = 0$:

$$A_r(\tau) = R(\delta_i)A_{in}(-\tau),\ A_t(\tau) = T(\delta_i)A_{in}(S\tau)e^{-i\delta_t(\delta_i)\tau + iS\delta_i\tau} \tag{3.16}$$

We can see that the reflected pulse is a time-reversed version of the input pulse, while the transmitted pulse has some change in its width due to the fact that the frequency of the incident wave and transmitted wave have a nonlinear relation. The time-reversal feature of the reflected pulse may have applications in subwavelength focusing and dispersion compensation [55, 56, 57].

Eq. (3.16) is derived by substituting $z = 0$ into Eqs. (3.14) and (3.15). It may seem contradictory since at $z = 0$, there should be only the incident pulse. Actually, the reflected and transmitted pulses, that appear at some finite z can be calculated by doing a linear propagation of the pulses obtained from Eq. (3.16). We write Eq. (3.16) in this way to separate the effect of the boundary from the effect of dispersion during the propagation of the transmitted and reflected pulses.

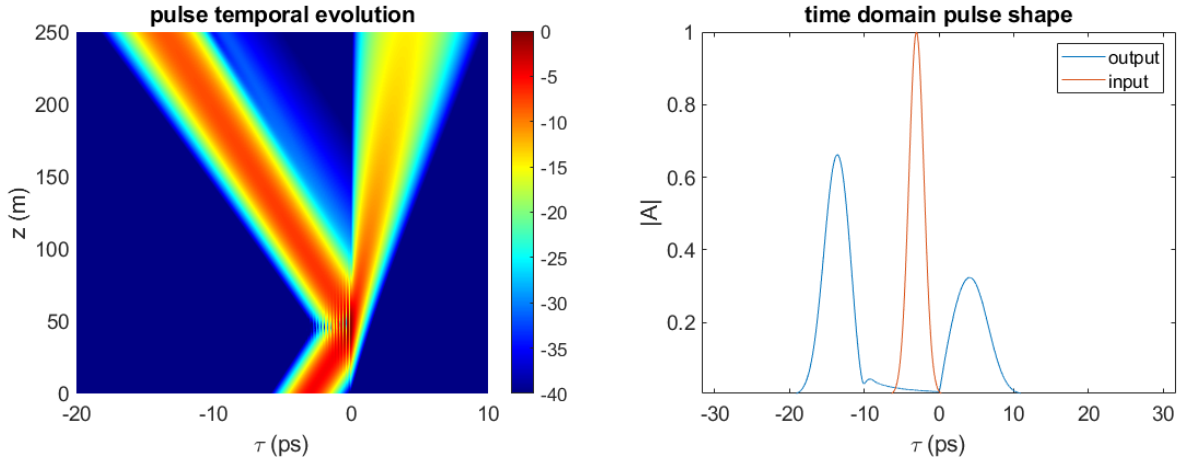

(a) (b)

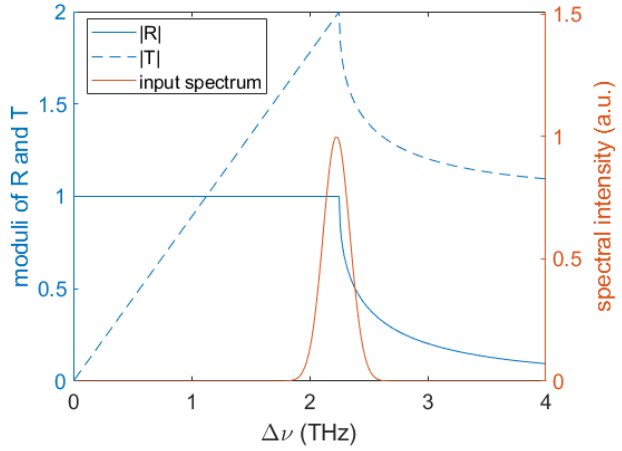

(c)

Figure 3.4: (a) Simulation of temporal reflection. The input pulse's central frequency lie at the critical point of total reflection. (b) The output pulse shape compared with the input pulse shape. (c) Input spectrum compared to $|R|$ and $|T|$.

It is also worth noting that the assumption that R and T are constant within the input pulse's spectral bandwidth might not hold when the input pulse is too short, or when the spectrum lies near the critical point of total reflection (See Fig. 3.2), where R and T changes quickly as the input frequency changes. The result of this usually leads to some distortion of the reflected and transmitted pulse shapes compared with the input pulse.

As an example, we performed simulations with an input pulse spectrum centered at the critical point, where the coefficients R and T changes rapidly as the input frequency changes. The parameters chosen are the same as in Fig. 3.3, except that $\Delta\nu_i = 2.23$ THz. The results are shown in Fig. 3.4. We can clearly see that the reflected pulse and transmitted pulse shapes are distorted compared with the input Gaussian shape, as the result of the rapid change of R and T across the spectrum of the input pulse.

Eq. (3.16) assumes that the total reflection condition is not satisfied, meaning that $R(\delta_i)$ and $T(\delta_i)$ are both real. If the total reflection condition is satisfied for all spectral components of the

input pulse, there would be no transmitted pulse. The reflected pulse shape needs to be re-derived since now, R is a complex number. From Eq. (3.11) shows that when $\delta^2 - 2\beta_B/\beta_2 < 0$, R is a complex number with modulus 1. We can write $R = \exp[i\phi_R(\delta)]$. If the input pulse spectral width is small enough, we can perform a Taylor expansion of the phase ϕ_R around the input pulse central frequency δ_i, and keep up to the first order term:

$$\phi_R(\delta) \approx \phi_R(\delta_i) + \frac{d\phi_R}{d\delta}\Big|_{\delta=\delta_i}(\delta - \delta_i) \tag{3.17}$$

$$= \phi_R(\delta_i) - \frac{2}{\sqrt{2\beta_B/\beta_2 - \delta^2}}(\delta - \delta_i) \tag{3.18}$$

Here, we define $\tau_{GH} = 2/\sqrt{2\beta_B/\beta_2 - \delta^2}$. Then, the reflected pulse shape is obtained from Eq. (3.14) (also at $z = 0$ to eliminate the effect of dispersion in propagation):

$$A_r(\tau) = e^{i(\phi_R(\delta_i) + \tau_{GH}\delta_i)} A_{in}(-\tau + \tau_{GH}) \tag{3.19}$$

The reflected pulse now has a temporal offset, or an additional delay τ_{GH}, which is not present when the total reflection condition is not satisfied. This delay is the temporal version of Goos-Hänchen (GH) shift [58, 59, 60, 61]. The conventional GH shift takes place when a beam undergoes total internal reflection at a spatial interface between two media. The reflected beam center is shifted from its geometrical optics trajectory. The time domain GH shift that we describe here is another demonstration of the concept of space-time duality.

We performed simulation using $\beta_2 = 0.05$ ps^2/m and $\beta_B = 1$ m^{-1}. The input pulse has a Gaussian shape with a full width at half maximum (FWHM) of 6 ps. The input pulse leads the boundary by 14 ps. The frequency offset from the group velocity matching frequency (with the moving boundary) is $\Delta\nu_i = 0.8$ THz. The result is shown in Fig. 3.5. In (a), the time domain

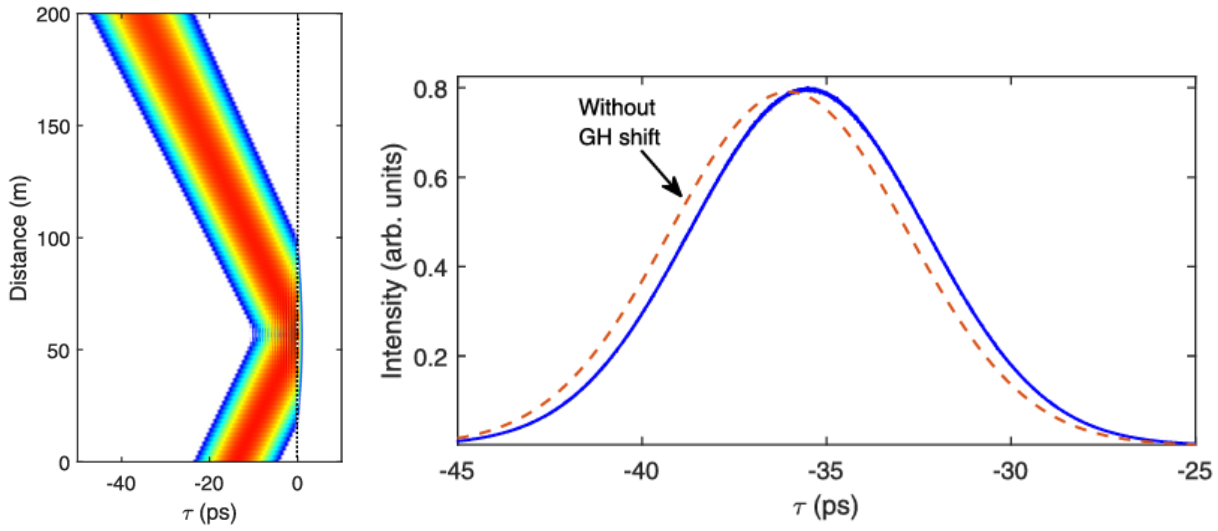

(a) (b)

Figure 3.5: (a) Simulation of an input pulse undergoing total reflection from a moving boundary. (b) Demonstration of the time domain Goos-Hänchen shift.

evolution shows that the pulse is completely reflected by the moving boundary, with no transmitted field. In (b), the output pulse shape is shown, compared with a calculation of the output pulse if the GH shift is not present, visualizing the effect of GH shift. The red dashed curve is calculated by sending a "mirrored" light pulse of the input pulse with respect to the boundary, and letting the mirrored pulse propagate (in this case there is no boundary present) for the same amount of distance (200m in this case). The GH shift from analytical calculation should be 0.516 ps, while the shift from the numerical simulation is 0.524 ps (evaluated from the center of mass), showing a good agreement.

3.5 Boundary with a Finite Rise Time

In the previous sections, we considered the reflection of an incident pulse at an ideally sharp boundary, with its shape described by a Heaviside function. Such assumption needs to be re-examined from a practical point of view, since any boundary that can be generated must have a finite rise time. In this section, we perform an analysis of the temporal reflection of an incident pulse at a boundary with a finite rise time.

We use the pulse propagation equation given in Eq. (3.5):

$$\frac{\partial A}{\partial z} + i\frac{\beta_2}{2}\frac{\partial^2 A}{\partial \tau^2} = i\beta_B s(\tau) A. \tag{3.20}$$

To model a boundary with finite rise time, on the right-hand side $\beta_B = (\omega_0/c)\delta n$ is proportional to the magnitude of index change, and $s(\tau)$ governs the shape of the boundary with values in the range 0–1. For the present, we leave $s(\tau)$ unspecified and only note that its value rises from 0 to 1 over a finite duration related to the rise time of the boundary.

We still consider a plane wave solution, similar to the discussion for the sharp boundary case. This is done by solving the "time-independent Schrödinger's Equation", where the solution A should be in the form of $\exp(i\beta' z)A_T(\tau)$. The boundary shape function $s(\tau)$ should tend to 0 as $\tau \to -\infty$, and tend to 1 as $\tau \to +\infty$. The equation governing A_T is given by:

$$\beta' A_T + \frac{\beta_2}{2}\frac{d^2 A_T}{d\tau^2} = \beta_B s(\tau) A_T, \tag{3.21}$$

which does not always have an analytical solution. We need to use numerical techniques to solve for the reflection and transmission coefficients of this boundary $s(\tau)$. Here, we use a staircase approximation, by breaking the continuous $s(\tau)$ into a number of discrete steps, in each step we can assume that $s(\tau)$ is a constant (See Fig. 3.6). In this way, we can calculate a transfer matrix that relates the amplitudes of the waves across the boundary.

To be more specific, we consider that in the n-th segment (τ_n, τ_{n+1}), $s(\tau) = s_n$. Then, inside this segment, the solution should be:

$$A_T(\tau) = A_{n+} e^{-i\delta_n \tau} + A_{n-} e^{i\delta_n \tau} \text{ for } \tau \in (\tau_n, \tau_{n+1}), \tag{3.22}$$

where the frequency $\delta_n = \sqrt{2(\beta' - \beta_B s_n)/\beta_2}$ is obtained so that $A_T(\tau)$ satisfies Eq. (3.21) in each segment. We write $A_T(\tau) = A_+(\tau) + A_-(\tau)$, by separating the two parts of the previous equation.

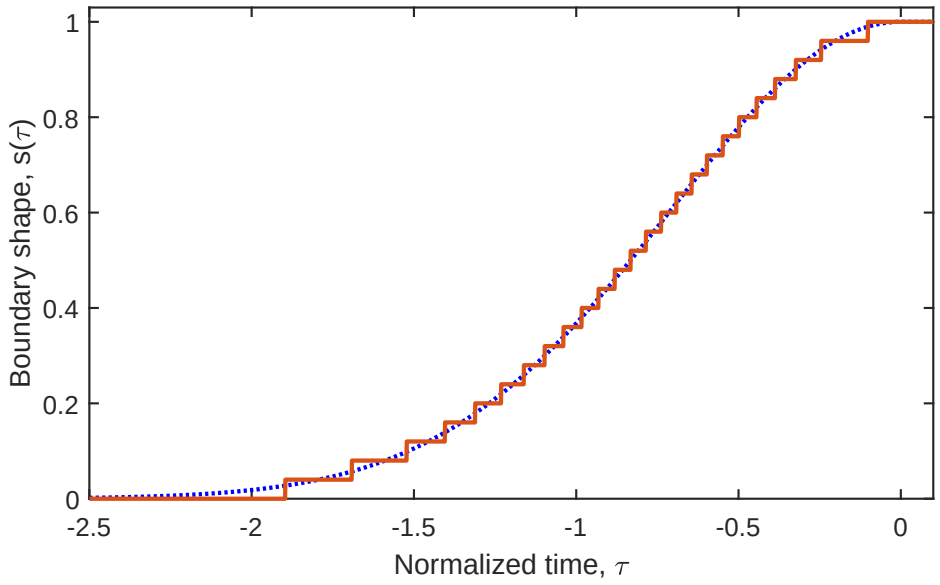

Figure 3.6: staircase approximation: break the continuous boundary function into a number of discrete steps.

We then have:

$$\frac{dA_T}{d\tau} = -i\delta_n A_+ + i\delta_n A_- \text{ for } \tau \in (\tau_n, \tau_{n+1}), \tag{3.23}$$

At the boundaries between two segments, we match the boundary conditions to ensure that both A_T and $dA_T/d\tau$ are continuous. Thus, we can relate the values of A_+ and A_- across the boundary in the following form:

$$\begin{pmatrix} A_+(\tau_{n,-}) \\ A_-(\tau_{n,-}) \end{pmatrix} = \begin{pmatrix} \frac{\delta_n+\delta_{n+1}}{2\delta_n} & \frac{\delta_n-\delta_{n+1}}{2\delta_n} \\ \frac{\delta_n-\delta_{n+1}}{2\delta_n} & \frac{\delta_n+\delta_{n+1}}{2\delta_n} \end{pmatrix} \begin{pmatrix} A_+(\tau_{n,+}) \\ A_-(\tau_{n,+}) \end{pmatrix}, \tag{3.24}$$

The values of A_+ and A_- within a single segment can be related by another matrix:

$$\begin{pmatrix} A_+(\tau_{n,+}) \\ A_-(\tau_{n,+}) \end{pmatrix} = \begin{pmatrix} e^{i\delta_n(\tau_{n+1}-\tau_n)} & 0 \\ 0 & e^{-i\delta_n(\tau_{n+1}-\tau_n)} \end{pmatrix} \begin{pmatrix} A_+(\tau_{n+1,-}) \\ A_-(\tau_{n+1,-}) \end{pmatrix}, \tag{3.25}$$

We denote the matrix in Eq. (3.24) as T_n and the matrix in Eq. (3.25) as P_n. We can then relate the field at any two points using matrix multiplications. This method is analogous to the calculation of reflectivity of a multi-film dielectric stack [34].

If we wish to consider the reflectivity of the whole boundary, we assume that for $\tau < \tau_0$ $s(\tau) = 0$ and for $\tau > \tau_N$, $s(\tau) = 1$. We discretize the boundary into N segments. Since we consider that the incident wave comes from the $\tau < \tau_0$ side, the solution should contain both the incident and reflected wave for $\tau < \tau_0$ while it should contain only the transmitted wave for $\tau > \tau_N$. The amplitudes of the three waves can be related by the matrix multiplication:

$$\begin{pmatrix} A_{in} \\ A_r \end{pmatrix} = T_0 P_0 T_1 P_1 \ldots T_{N-1} P_{N-1} T_N \begin{pmatrix} A_t \\ 0 \end{pmatrix}. \tag{3.26}$$

We denote the matrix product in the middle as M. This is the transfer matrix of the entire boundary. Then, the reflection and transmission coefficients are given by:

$$R = \frac{A_r}{A_{in}} = \frac{M_{21}}{M_{11}}, T = \frac{A_t}{A_{in}} = \frac{1}{M_{11}}. \tag{3.27}$$

It is worth noting that the same transfer matrix can also be obtained by directly solving Eq. (3.21) numerically (using, for example, the Runga-Kutta method), with the appropriate boundary conditions.

Using the method described above, we study the impact of the boundary's shape and sharpness on the reflectivity. One simple way to consider boundaries with different rise times is to employ a specific shape controlled by the super-Gaussian function,

$$s(\tau) = \begin{cases} \exp[-(\tau/T_0)^{2m}], & \text{for } \tau < 0, \\ 1, & \text{for } \tau \geqslant 0, \end{cases} \tag{3.28}$$

such that $s = 1$ at the boundary location $\tau = 0$. The parameter m governs the boundary's sharpness. Increasing m makes the boundary sharper.

We calculated the reflectivity of boundaries with the same index change, or the same $\beta_B = 0.5$ m^{-1}, but different sharpness. The boundaries are discretized into 500 segments. The result is shown in Fig. 3.7. On the left, we show these different boundary shapes, which are obtained with $T_0 = 0.5$ ps, but different m to create different sharpness. Note that in Fig. 3.7 the shape functions $s(\tau)$ has been shifted compared to the expression given in Eq. (3.28) to better visually compare the boundaries with different sharpness. Reflectivities $|R|^2$ are calculated for different incident waves, that have some frequency offset from the group velocity matching frequency. The dispersion parameter is given by $\beta_2 = 5$ $\mathrm{ps}^2/\mathrm{km}$. As seen from Fig. 3.7, all the different boundaries have the same critical frequency $\Delta\nu_c$ for total reflection. When the frequency offset is larger than this critical frequency, the reflectivities decreases with the increase of the frequency offset $\Delta\nu$. The slower the boundary is (less sharp), the more rapidly the reflectivities fall off. For boundaries with a long rise time, the reflectivity is almost a step function of the incident frequency.

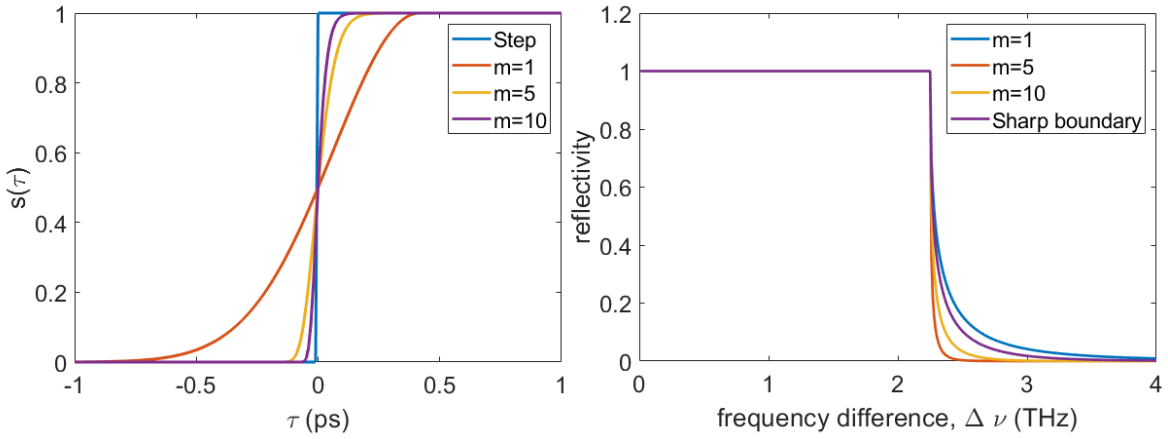

Figure 3.7: Left: boundaries with different sharpness by varying m. Right: reflectivity of the different boundaries as a function of incident wave frequencies.

We perform numerical simulations for incident pulses, instead of monochromatic waves. We consider an input pulse:

$$A_{in}(\tau) = \exp\left(\frac{1}{2}\left(\frac{\tau}{T_1}\right)^2\right)\exp(-i2\pi\Delta\nu_i\tau), \tag{3.29}$$

with $\Delta\nu_i = 3.2$ THz and $T_1 = 2$ ps. The boundary has a shape given in Eq. (3.28) for $m = 1$ and $T_0 = 0.5$ ps. Here, we consider two different index changes, with $\beta_B = 0.95$ m^{-1} and 1.05 m^{-1} respectively. The result is shown in Fig. 3.8. We see partial reflection in both cases. However, a small amount of change in β_B (10%) leads to a big amount of change in the overall reflectivity (14.5% to 94%). The reason is that for a boundary not quite sharp, the reflectivity becomes almost a step function of the incident frequency. The critical frequency depends on the amount of index change β_B. We chose the parameters so that the central frequency of the incident pulse is larger than the critical frequency for the small β_B, but smaller than the critical frequency for the larger β_B. The reflection is not 100% because, even though the TIR condition is satisfied for the central frequency of the pulse, a portion of the pulse's spectrum lies outside the TIR region because of a relatively large bandwidth of the pulse. For wider pulses with a smaller bandwidth, the change from full transmission to total reflection becomes more dramatic and exhibits a switch-like behavior in the sense that a relatively small change in the refractive index produces large changes in the reflected energy of the incident pulse.

3.6 Time-Domain FP Resonator

Here, we discuss the possibility of constructing an analog of the Fabry-Perot resonator (FPR) based on the concept of temporal reflections.

The conventional FPR consists of two partially reflecting mirrors separated by some distance. When the two mirrors have high reflectivities, the transmission spectrum has an array of peaks. If

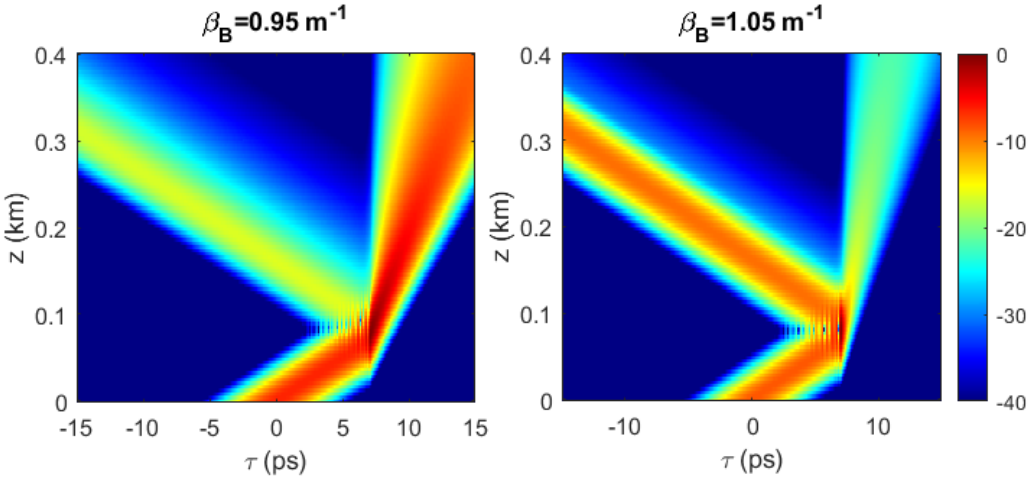

Figure 3.8: Simulation of temporal reflection on a boundary with finite rise time with two different index changes.

there is no loss, the peak transmission is 100% at the resonance frequencies of the FPR.

For our case, we consider two moving boundaries separated in time by some delay. Since each moving boundary can reflect light through temporal reflection, we expect the two moving boundaries to form a FPR from temporal reflection.

We assume that the boundary shape function is in the following form:

$$s(\tau) = s_0(\tau) + s_0(\tau - T_c). \tag{3.30}$$

Unlike the previous case, here $s_0(\tau)$ is assumed to be a pulse, meaning that it goes to 0 for $\tau \to \pm\infty$. A single pulse forms a boundary that results in temporal reflection. Two pulses should create a time domain FPR.

We use the transfer matrix method described in Section 3.5. As shown in Fig. 3.9, a single boundary has a transfer matrix given by M. Then, the transfer matrix of the entire structure is given by matrix multiplication:

$$M_{FP} = \begin{pmatrix} M_{11} & M_{12} \\ M_{21} & M_{22} \end{pmatrix} \begin{pmatrix} e^{i\delta T} & 0 \\ 0 & e^{-i\delta T} \end{pmatrix} \begin{pmatrix} M_{11} & M_{12} \\ M_{21} & M_{22} \end{pmatrix}. \tag{3.31}$$

M_{ij} is the matrix elements of M, and δ is the incident wave frequency offset from the group velocity matching frequency ω_0. Using the transfer matrix, the transmissivity of the FPR is found to be:

$$T_{FP} = \frac{1}{|[M_{FP}]_{11}|^2} = |M_{11}^2 e^{2i\delta T} + M_{12}M_{21}|^{-2}, \tag{3.32}$$

It is possible to simplify this expression using the properties of matrix M. Since the matrix M is found from Eq. (3.21), we notice that if A_T is a solution to this equation, so is A_T^*, which is the

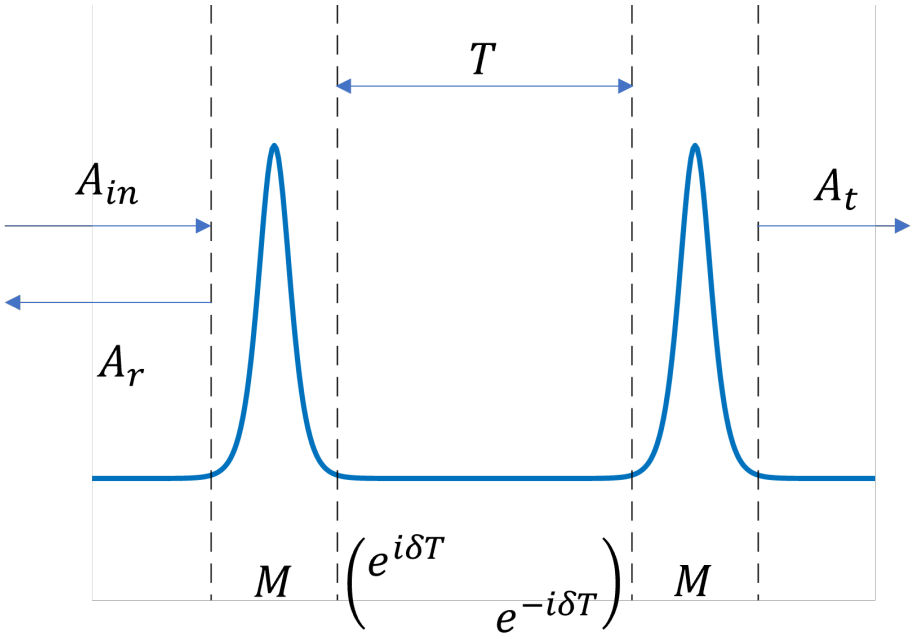

Figure 3.9: sketch of time domain FPR formed by two boundaries.

complex conjugate of A_T. Since M should correctly relate the amplitudes of the forward wave and backward wave of both A_T and A_T^*, it can be shown that:

$$\begin{pmatrix} M_{11} & M_{12} \\ M_{21} & M_{22} \end{pmatrix} = \begin{pmatrix} M_{22}^* & M_{21}^* \\ M_{12}^* & M_{11}^* \end{pmatrix}. \tag{3.33}$$

Furthermore, a single boundary's reflectivity and transmissivity should add up to 1, i.e.,

$$\left|\frac{M_{21}}{M_{11}}\right|^2 + \left|\frac{1}{M_{11}}\right|^2 = 1 \tag{3.34}$$

Note that this relation holds since the refractive index on both sides of the boundary is assumed to be the same. It would not hold for the boundaries discussed in the earlier sections.

Using the two relations above, we can simplify Eq. (3.32) considerably. Denote $M_{11} = |M_{11}|\exp(i\phi_0)$, and $\Gamma = M_{21}/M_{11}$ as the amplitude reflection coefficient of a single pump pulse, we obtain:

$$\begin{aligned} T_{FP} &= \frac{1}{|M_{11}|^4 + |M_{12}|^2|M_{21}|^2 + M_{11}^2 M_{12}^* M_{21}^* e^{2i\delta T} + M_{11}^{*2} M_{12} M_{21} e^{-2i\delta T}} \\ &= \frac{1}{|M_{11}|^4} \frac{1}{1 + \frac{|M_{21}|^4}{|M_{11}|^4} + \frac{|M_{21}|^2}{M_{11}^{*2}} e^{2i\delta T} + \frac{|M_{21}|^2}{M_{11}^2} e^{-2i\delta T}} \\ &= (1-|\Gamma|^2)^2 \frac{1}{1 + |\Gamma|^4 + 2|\Gamma|^2 \cos\left(2(\delta T + \phi_0)\right)} \\ &= \left(1 + \frac{4|\Gamma|^2}{(1-|\Gamma|^2)^2} \cos^2 \frac{\phi}{2}\right)^{-1}, \end{aligned} \tag{3.35}$$

where we defined the phase ϕ:

$$\phi = 2\delta T + 2\phi_0. \tag{3.36}$$

The transmissivity of the FPR that we consider has a similar form compared with a conventional spatial FPR. Similar to the spatial case, when we consider the transmissivity of the FPR as a function of the incident wave frequency δ, multiple peaks with 100% transmission occur when the resonance condition, $\phi = (2m+1)\pi$, is satisfied, where m is an integer. Also, similar to a spatial FPR, the larger is the value of the single boundary reflectivity $|\Gamma|^2$, the sharper the transmission peak becomes. However, there is one critical feature that makes a temporal FPR quite different from a spatial slab. Whereas the reflectivity at two spatial interfaces is nearly constant over a wide spectral range in the spatial case, it changes rapidly in the temporal cases because $|\Gamma|^2$ depends on the incident frequency δ.

As an example, we assume that a single boundary has the form of $s_0(\tau) = \text{sech}^2(\tau/T_0)$. This corresponds to the scenario where one uses an optical soliton to create a moving boundary that can reflect weaker light pulses at another wavelength. We set the maximum change of propagation constant as $\beta_B = 1.2\ \text{m}^{-1}$, which corresponds to a maximum index increase of only $\Delta n = 3\times10^{-7}$. We use $T_0 = 50$ fs and the two boundaries are separated by $T_c = 1.4$ ps. The dispersion parameter is given: $\beta_2 = 5\ \text{ps}^2/\text{km}$. We calculated the transfer matrix of each boundary by dividing it into 500 segments from $-4T_0$ to $4T_0$. We used this matrix to calculate both $|\Gamma|^2$ and the transmissivity T_{FP} of the FPR as a function of incident wave frequency δ, and the result is shown in Fig. 3.10.

From the figure, the transmissivity of the FPR T_{FP} does show an array of peaks as the incident frequency changes. These peaks have a transmissivity of 1 since they satisfy the resonance condition. Another interesting feature here is that the peaks have less and less finesse as $\Delta\nu$ increases. This can be understood by the change of the single boundary reflectivity $|\Gamma|^2$ as $\Delta\nu$ increases. When the incident wave has a larger frequency offset from the group velocity matching frequency, its velocity difference compared with the boundary becomes larger, and the reflectivity drops down, which leads to the decrease of the resonance peaks' finesse.

Next, we simulated the transmission of a pulse through the FPR at the peak and valley of one transmission peak in Fig. 3.10 by solving (3.20) numerically. We used an input Gaussian-shape pulse:

$$A(0,\tau) = \exp(-\tau^2/(2T_0^2))\exp(-2\pi i\Delta\nu_i\tau), \tag{3.37}$$

with $T_0 = 20$ ps. The frequency $\Delta\nu_i$ is chosen so that the pulse's spectrum lies lie at the peak or valley of the transmission curve of the FPR. The result is shown in Fig. 3.11. (a) shows the temporal evolution of the pulse when its frequency is at the transmission peak of the FPR while (b) shows the result when the incident frequency is at the transmission valley. (d) shows the incident spectrum together with the transmission curve of the FPR.

As predicted by our transfer-matrix method, the pulse is almost completely transmitted when its spectrum is centered at the transmission peak. In contrast, it is mostly reflected when its spectrum is centered at the transmission valley. In both cases, there is some energy leakage due to the finite width of the resonator. The reason for almost perfect transmission and reflection is related to a relatively large width of the probe pulse, chosen to ensure a narrow spectrum that fits within the bandwidth of the transmission peak.

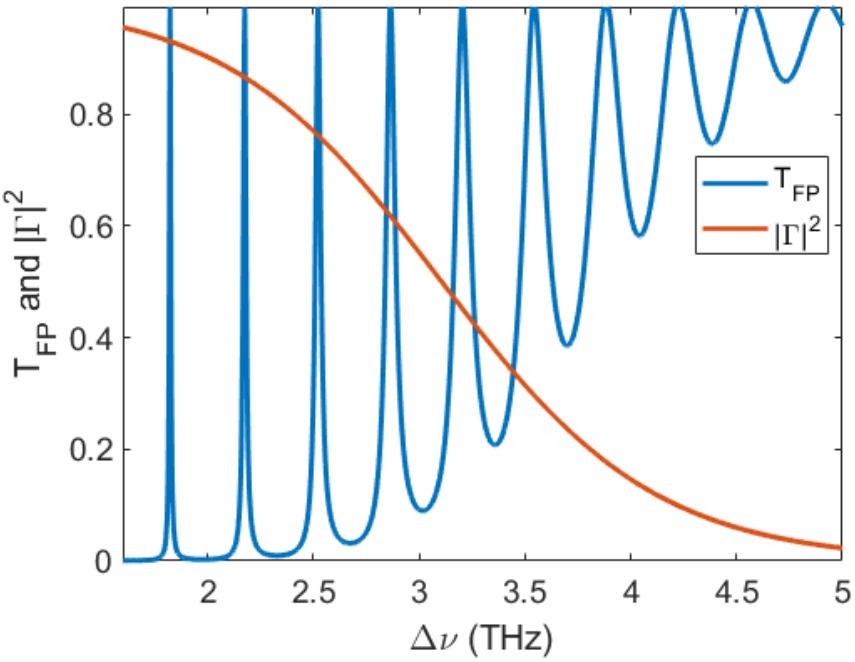

Figure 3.10: Frequency dependence of T_{FP} (blue line) and $|\Gamma|^2$ (orange line) for a temporal FPR formed using two boundaries that have sech^2 shape, induced by optical solitons.

When the probe pulse becomes shorter than 10 ps, its spectrum becomes wider than the transmission peak, and the FPR behaves like an optical filter. To verify this, we simulated the case of a probe pulse with $T_0 = 2$ ps, and the results are shown in Fig. 3.12. We see that only a part of the pulse is transmitted even though the pulse's spectrum is centered at the peak with 100% transmission. This is so because the probe spectrum is wider than the transmission peak, as seen at the bottom of Fig. 3.12, resulting in a significant amount of reflection. Both the reflected and transmitted pulses have long tails, caused by multiple reflections occurring inside the FPR. We also show the spectrum of the transmitted pulse together with the transmission curve of the FPR. The transmitted spectrum is narrower than that of the incident pulse and fits within the transmission peak, as expected on the physical ground. These results indicate clearly that a temporal FPR can be used as an optical filter.

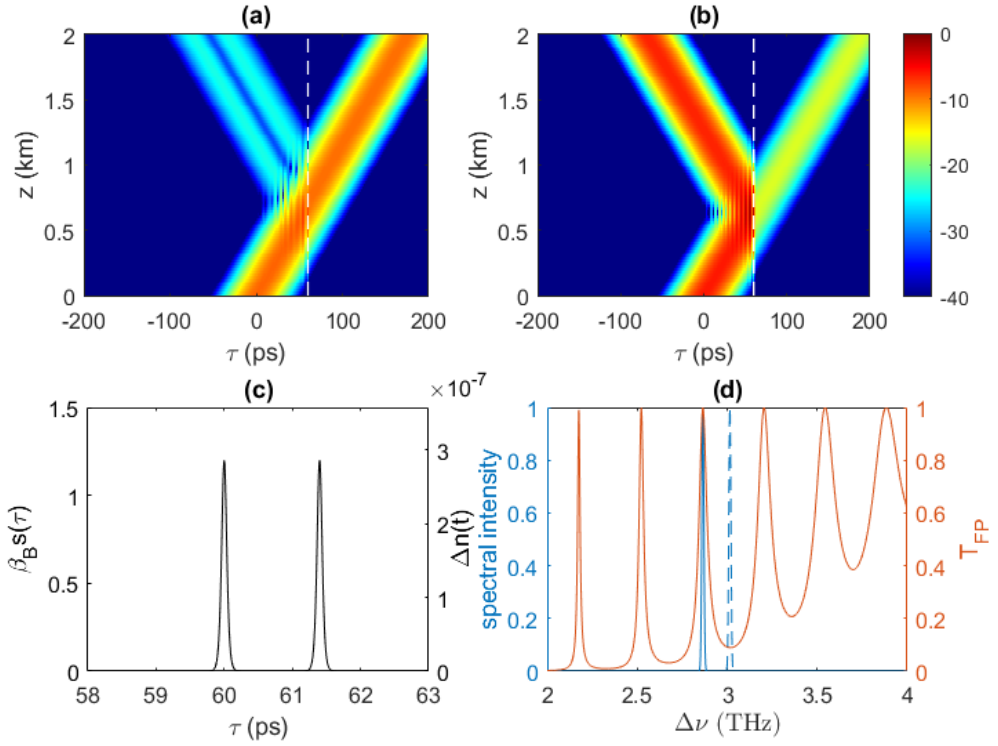

Figure 3.11: Temporal evolution of a 20-ps Gaussian pulse when its spectrum is centered at (a) a transmission peak and (b) a transmission valley. (c) shape of the FPR formed by two boundaries (d) Location of pulse spectra within the transmission curve (red) of the FPR. The blue solid line is the incident spectrum in (a) and the dashed line is the incident spectrum in (b); spectral intensity is plotted.

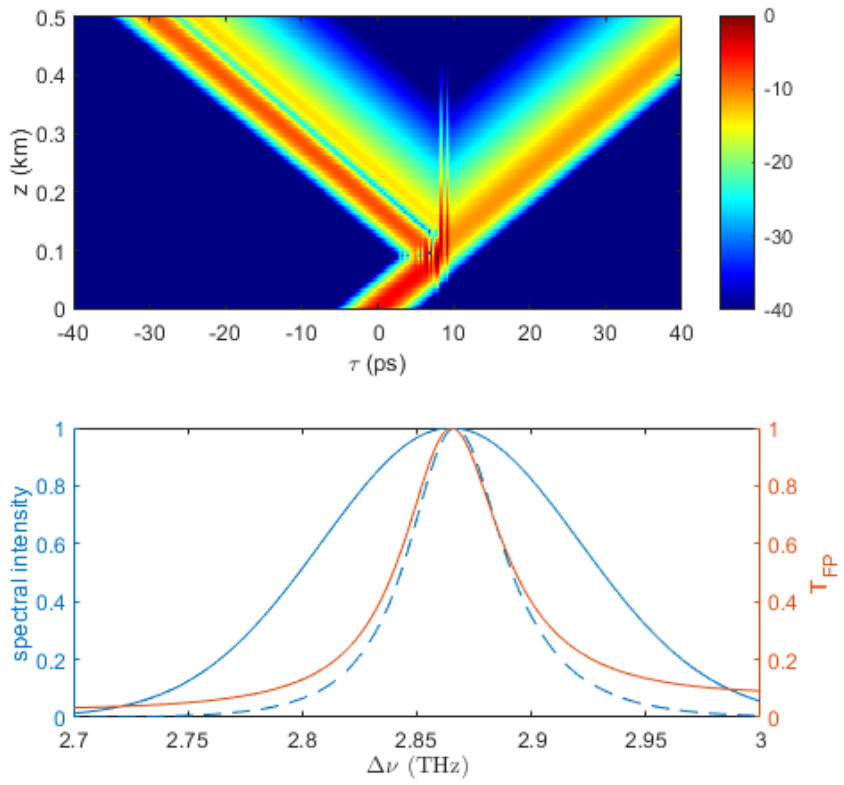

Figure 3.12: Top: Temporal evolution of a 2-ps Gaussian pulse when its spectrum is centered at a transmission peak of the FPR. Bottom: Spectra of the incident (blue solid line) and transmitted pulses (blue dashed line) superposed on the transmission curve of the FPR (red).

3.7 Conclusion

In this chapter, we discussed the phenomenon of temporal reflection at a moving boundary in a dispersive medium, where an incident pulse can split into reflected and transmitted pulses with some amount of frequency shifts from the incident pulse. Remarkably, this type of temporal reflection results in a forward-traveling reflected wave, which is different from the temporal reflection with a purely temporal boundary that changes the index everywhere simultaneously. In the latter case, the reflected light travels backwards.

We proposed a mathematical model for describing temporal reflection, and studied a few examples using this model. We show that the temporal reflection in our case requires a much smaller index change to result in a significant reflection, with a large frequency shift. Using our model, we derived the reflection and transmission coefficients for a sharp boundary as a function of incident wave frequency, showing the possibility of total reflection, as a temporal analog of total internal reflection for a glass-air spatial interface.

We also studied the temporal reflections with boundaries that have some rise time. Using the transfer matrix method, we studied the impact of the boundary's sharpness on temporal reflection, showing that the total reflection condition is not influenced by the boundary's rise time, but when

the total reflection condition is not satisfied, the increase of the boundary's rise time leads to a decrease in the reflectivity. For boundaries that have a large rise time (not sharp), the reflectivity approaches a step function of the incident wave frequency.

We demonstrated that the temporal analog of a spatial FPR might be constructed from two moving boundaries. We showed that sharp resonance peaks can form when the reflectivity of a single boundary is high and the resonance condition is satisfied. We showed from numerical simulation, that such FPR can serve as an optical filter. We also believe that other types of optical phenomena that happen for a spatial beam should have their counterparts for temporal pulses.

Chapter 4

Boundary Formed by Short Pulses

In Chapter 3, we studied the phenomenon of temporal reflection at a moving boundary whose shape function is given with some assumptions. The dynamics of the boundary itself was not considered. Starting from this chapter, we consider more realistic situations and take into account how the boundary is induced and how its shape might change. To be more specific, we focus on using the optical Kerr effect to create an index change using a strong pump pulse. The pump pulse causes the index to increase, and this boundary of index change can reflect another weaker probe pulse. It is then important to consider the evolution of the pump and probe pulses together.

When an ultrafast laser pulse is used as a pump pulse to create a boundary with a fast rise time, chromatic dispersion and multiple nonlinear effects become important. We found that the most important higher-order nonlinear effect is stimulated Raman scattering, which causes the spectrum of the pump pulse to continuously shift to the longer wavelengths. Combined with the dispersion, this continuous frequency shift causes the pump pulse to reduce its speed as it propagates, creating a boundary with deceleration. We also found that the temporal reflection of a probe pulse from such a boundary can result in several more interesting phenomena, that are not possible for pulses reflecting on a boundary with constant velocity.

In this chapter, we first discuss how the pump pulse evolves as it propagates in the medium. Its evolution determines both the shape and the speed of the boundary formed by the pump pulse. Then, we discuss how the probe pulse reflects at this boundary and the interesting phenomena that can occur.

4.1 Optical Solitons

For temporal reflection to occur, one would prefer creating a moving boundary that does not change its shape as it propagates. This was assumed to be the case in Chapter 3. If we choose to send a strong pump pulse to induce the boundary from Kerr effect, this pump pulse would also experience the dispersion and nonlinearity of the medium. For the pump pulse to maintain its shape during propagation in the presence of dispersion and nonlinearity, we consider using an optical soliton as the pump pulse.

Soliton is a special type of pulse that maintains the same shape during propagation in a nonlinear and dispersive medium. The discovery of soliton dates back to 1834, when Scott Russell

observed a heap of water that propagated without distortion for several kilometers [62]. In the 20th century, solitons were discovered in many other areas of physics [63, 64, 65]. A lot of work has been done in the field of fiber optics [66, 67, 68], where the nonlinearity comes from the optical Kerr effect.

The simplest equation that describes an optical soliton takes into account both the second-order dispersion and the Kerr effect. The pulse propagation is governed by the nonlinear Schrodinger's equation [28]:

$$\frac{\partial A}{\partial z} + \frac{i\beta_2}{2}\frac{\partial^2 A}{\partial \tau^2} = i\gamma|A|^2 A. \tag{4.1}$$

There is an analytical way of solving Eq. (4.1) using a technique called inverse scattering method [69, 70]. However, this method is mathematically involved and it only applies to a few types of equations. With the presence of higher-order nonlinearity, one has to use numerical approaches.

Normally, we consider a medium with a positive Kerr effect ($\gamma > 0$). In this case, a bright optical soliton exists when the dispersion is anomalous, or $\beta_2 < 0$. The solution for a bright soliton is given by:

$$A(z,\tau) = \sqrt{\frac{|\beta_2|}{\gamma T_1^2}}\operatorname{sech}\Big(\frac{\tau}{T_1}\Big)\exp\Big(i\frac{|\beta_2|z}{2T_1^2}\Big). \tag{4.2}$$

The soliton does not change its pulse shape as it propagates, which is a result of exact balancing of the dispersion and Kerr effect (also called self-phase modulation here because Kerr effect modulates the phase of the pulse depending on its own power). T_1 is the temporal width of the soliton, which determines the peak power of the soliton as $P = |\beta_2|/(\gamma T_1^2)$. There is also a nonlinear phase shift during the propagation of the soliton, which comes from the fact that the Kerr effect increases the index of the medium.

In general, dispersion causes the pulse to broaden since different parts of the spectrum travels at different speed, while the Kerr effect causes the pulse to spectrally broaden. In the case of a fundamental soliton, the two effects completely balance out each other. To develop a qualitative understanding of this balancing, we can use the analogy of pulse propagation with quantum mechanics. Eq. (4.1) has the same form as the standard 1-dimensional Schrodinger's equation, except that here, the potential is proportional to $|A|^2$. Suppose A has the form of a pulse, then we find that if $\beta_2 < 0$, the potential created by $|A|^2$ term is effectively a potential well, which supports localized eigenmodes. For a fundamental soliton Eq. (4.2), the potential well created by $|A|^2$ has a mode with the shape A, thus the pulse shape remains stationary as it propagates. In other words, the pulse is trapped by the potential created by itself.

There are also higher-order solitons when the input is given by:

$$A_N(0,\tau) = NA(0,\tau) \tag{4.3}$$

where N is an integer specifying the soliton's order. As a higher-order soliton propagates, it does not maintain its shape, but the pulse shape is periodic in the propagation distance z, with periodicity $z_0 = \pi T_1^2/(2|\beta_2|)$.

One other nice property of fundamental soliton is that it is stable against perturbations. When the input pulse shape does not have the exact form given in Eq. (4.2), if the deviation is not too large, the pulse still evolves into a fundamental soliton. However, as the pulse adjusts its shape, some energy of the pulse is shed away as a dispersive wave. The amount of energy lost is

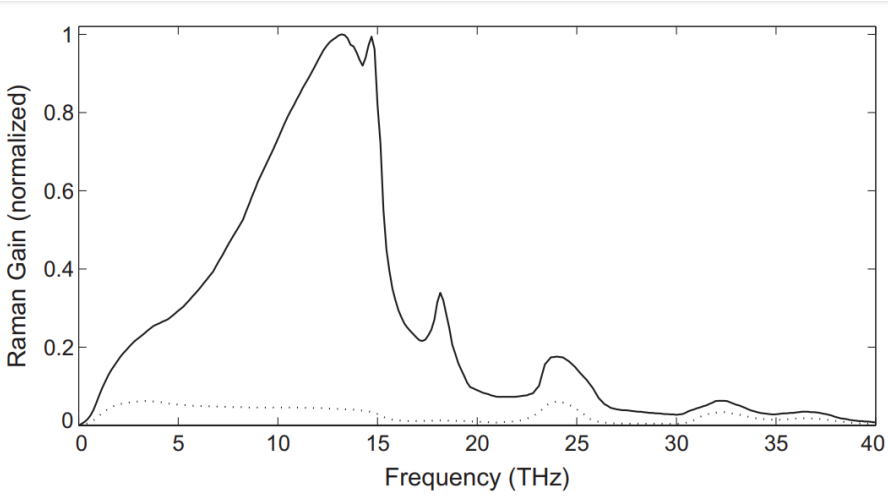

Figure 4.1: Raman gain as a function of frequency offset [36].

greater when the pulse shape deviates more from the form of a fundamental soliton. Fundamental solitons are also stable against other types of perturbations during their propagation, such as higher-order dispersion, higher-order nonlinear effects, losses, and so on. On the contrary, higher-order solitons are generally not stable against higher-order effects, and they generally break into multiple fundamental solitons of different energies [71, 72]. This process is called the soliton fission.

With the nice properties of stationary pulse shape and stability, for temporal reflection, we will choose to use a fundamental soliton as the pump pulse to create the refractive index boundary.

4.2 Raman Scattering

Eq. (4.1) that supports an exact fundamental soliton has neglected higher-order dispersion and higher-order nonlinearity. When the soliton that we launch into the medium is short enough (below 1 ps), then the higher-order nonlinear effects need to be considered. For our purposes, the most important higher-order nonlinearity is Raman scattering.

Raman scattering is an inelastic scattering process discovered by Indian physicist C. V. Raman [73], where an incoming photon (pump) is converted into a phonon of a molecular vibration mode, and a scattered photon with less energy, or smaller frequency. This photon is usually called the Stokes photon. If a Stokes photon is already present, then the presence of the Stokes photon increases the rate of Raman scattering. This process is called stimulated Raman scattering (SRS). In SRS, there is an effective gain of the Stokes wave from the pump wave. The gain experienced by the Stokes wave is proportional to the intensity of the pump wave, and also related to the frequency offset between the pump wave and Stokes wave [27].

In optical fibers, because of the amorphous structure of silica glass, the Raman gain spectrum has a large bandwidth [36] as shown in Fig. 4.1. The classical theoretical treatment of Raman scattering can be formulated as a kind of third-order nonlinearity [74, 75]. It enters the pulse propagation equation with the last nonlinear term in Eq. (2.25). The Raman scattering is considered as a delayed response (with the response function $h_R(t)$) to the input light pulse intensity. It can

be considered as the response of molecular vibrations driven by the laser pulse. When the laser pulse's temporal width is comparable to the oscillation frequency of the vibrations, the response is large but non-instantaneous.

For ultrashort solitons in optical fibers (sub 100fs), the effect of Raman scattering is extremely important. When a femtosecond pulse is injected into a fiber, its spectrum is wide enough that Raman scattering can happen among its own spectral components, with the result that its spectrum shifts continuously toward the red side when it propagates in the anomalous dispersion region as a soliton. This effect is also called intrapulse Raman scattering. The spectral shift leads to a deacceleration of the soliton and a continuous reduction in the speed of the pulse. When only the second-order dispersion is considered, the shape and width of the soliton do not change (approximately) during propagation, but its central frequency red-shifts linearly with the propagation distance z [76]. To be more specific, we consider the pulse propagation equation in the following form:

$$\frac{\partial A}{\partial z}+\frac{i}{2}\beta_2\frac{\partial^2 A}{\partial \tau^2}=i\gamma A(z,\tau)\int_{-\infty}^{\infty}R(\tau')|A(z,\tau-\tau')|^2 d\tau', \tag{4.4}$$

where the nonlinear response function $R(\tau)$ is given:

$$R(\tau)=(1-f_R)\delta(\tau)+f_R h_R(\tau). \tag{4.5}$$

Eq. (4.4) is the same as Eq. (2.28), except that the higher-order dispersion, losses, and self-steepening are neglected. We found that the effect of self-steepening is usually weak compared to the other effects and it is reasonable to neglect it here. For the propagation of soliton alone, the higher order dispersion can also be neglected since we assume that its spectrum does not extend too wide. Fiber losses are also neglected because of the relatively short lengths (< 0.1 km) required for this work. In Eq. (4.4), the first term is the instantaneous response from the Kerr effect and the second term is the delayed response from the Raman effect. The coefficient f_R and the form of $h_R(\tau)$ are given in Chapter 2 (see Eq. (2.26)). In Eq. (4.4), we only take into account the second-order dispersion, the Kerr effect and Raman effect. Assuming that the medium has anomalous dispersion ($\beta_2<0$) and the input pulse shape $A_1(0,\tau)=\sqrt{P_1}\mathrm{sech}(\tau/T_1)$ corresponding to a fundamental soliton (P_1 is determined by the relation $P_1=|\beta_2|/(\gamma T_1^2)$), then the approximate solution at a distance z can be written as [77]:

$$A_1(z,\tau)=\sqrt{P_1}\mathrm{sech}\Big(\frac{\tau-q_p}{T_1}\Big)e^{-i\Omega_p\tau+i\phi_p}, \tag{4.6}$$

where the Raman-induced frequency and temporal shifts are given by

$$\Omega_p=-\frac{8T_R|\beta_2|z}{15T_1^4},\qquad q_p=\frac{4T_R\beta_2^2 z^2}{15T_1^4}=az^2. \tag{4.7}$$

Here $T_R\approx 3$ fs is a time constant determined by the Raman response function. We introduced a coefficient $a=4T_R\beta_{21}^2/(15T_1^4)$ to simplify the notation.

From Eq. (4.6), the Raman effect causes the input soliton to continuously red shift, with the amount of shift linear about the propagation distance. In the time domain, we also see that the pulse has some delay q_p that is proportional to z^2. This happens because as the soliton red shifts, it slows down because of the anomalous dispersion. Note that in Eq. (4.6), we worked in a moving

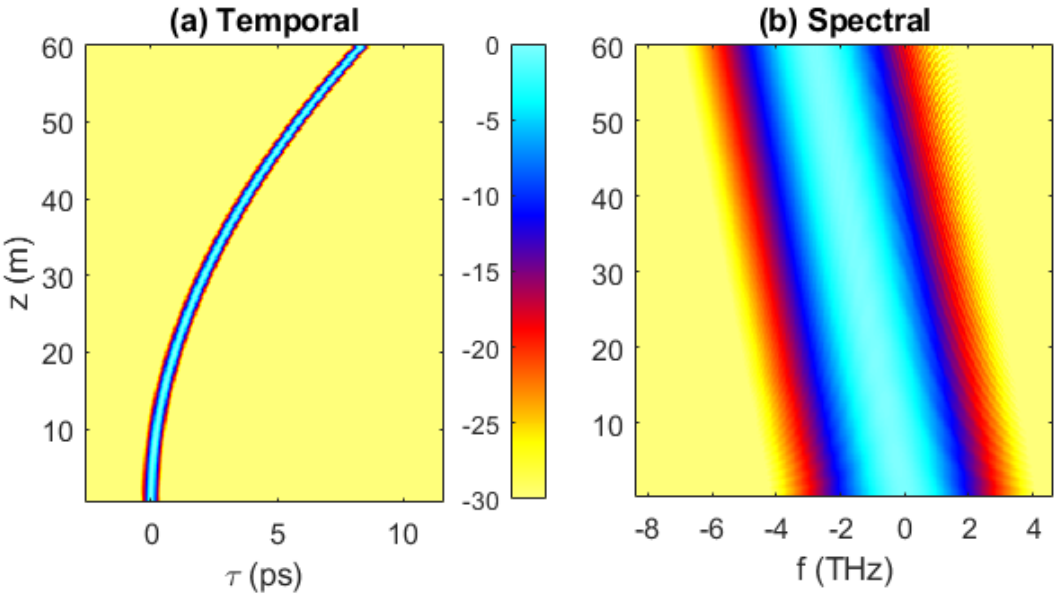

Figure 4.2: Evolution of the input soliton with the presence of Raman effect.

frame defined by $\tau = t - \beta_1 z$, where β_1 is the inverse of the group velocity at the incident soliton's central frequency. For a pulse that does not slow down, the delay would be 0 for all z.

We also performed a numerical simulation using Eq. (4.6). The value of β_2 is -15.7 ps^2/m. The input pulse shape $A(0,\tau)$ is a fundamental soliton given by Eq. (4.2) (evaluated at $z = 0$), with $T_1 = 100$ fs. The nonlinear coefficient is $\gamma = 1.3$ W^{-1}km^{-1} (In fact, γ does not affect the dynamics of propagation as long as the power scales inversely with it). These parameters are appropriate for a 1.5-μm pulse propagating in a regular single-mode fiber. The results for a 60-m-long optical fiber are shown in Fig. 4.2, where we show the evolution of the shape and spectrum of the soliton. As expected, the soliton's spectrum in part (b) shifts continuously toward the red side through Raman scattering. As a result of this shift, the pump pulse slows down inside the fiber with a delay that varies as z^2, resulting in a bent trajectory in part (a). We shall now study the temporal reflection of a probe pulse on the boundary created by the decelerating soliton.

4.3 Temporal Reflection

We consider using optical fiber to achieve the temporal reflection. The index boundary is created by the soliton via the Kerr effect. We would call the soliton the pump pulse. Another probe pulse (much weaker) is also launched into the fiber, and it can interact with the index boundary created by the pump. To model their interaction, we use Eq. (2.28), and neglecting the self-steepening term:

$$\frac{\partial A}{\partial z} - \sum_{m\geq 2} \frac{i^{m+1}}{m!}\beta_m \frac{\partial^m A}{\partial \tau^m} = i\gamma A(z,\tau)\int_{-\infty}^{\infty} R(\tau')|A(z,\tau-\tau')|^2 d\tau', \tag{4.8}$$

where γ is the nonlinear parameter and β_m is the mth order dispersion parameter at some reference frequency ω_1 and is defined $\beta_m = d^m\beta/d\omega^m\,|_{\omega_1}$. The pulse's envelope $A(z,t)$ is related to the

electric field as

$$E(z,t) = \frac{1}{2}\{A(z,t)\exp[i(\beta(\omega_1)z - \omega_1 t)] + c.c.\}, \tag{4.9}$$

Like before, the reduced time τ is related to the real time t by:

$$\tau = t - \beta_1(\omega_1)z. \tag{4.10}$$

The only additional thing that we included compared to Eq. (4.4) is that the higher-order dispersion is taken into account. We need to include it here because the envelope A here contains both the pump pulse as well as the probe pulse. They will be spectrally separated far enough that inclusion of only the second-order dispersion is not enough.

To realize temporal reflection, the group-velocity difference between the pump and probe pulses should be relatively small, as we have seen in Chapter 3. One way to achieve this is to notice that a single-mode silica fiber has its zero-dispersion wavelength around 1310 nm, where β_2 vanishes. As β_2 has different signs on the opposite sides of this wavelength, for any wavelength of the pump, a wavelength exists on the opposite side that has the same group velocity. Fig. 4.3 shows how the group index n_g varies with wavelength for silica fiber. The group velocity is related to it as $v_g = c/n_g$. For example, if we choose the pump's wavelength near 1500 nm, where solitons can form, the group velocity at 1145 nm will match that of the pump pulse. In practice, the central wavelength of the probe pulse should be in the range 1145 ± 20 nm to ensure a relatively high reflectivity.

The fact that the probe pulse lies in the normal-dispersion region is also important. This is because the pump pulse increases the index during its duration. As discussed in Chapter 3, a

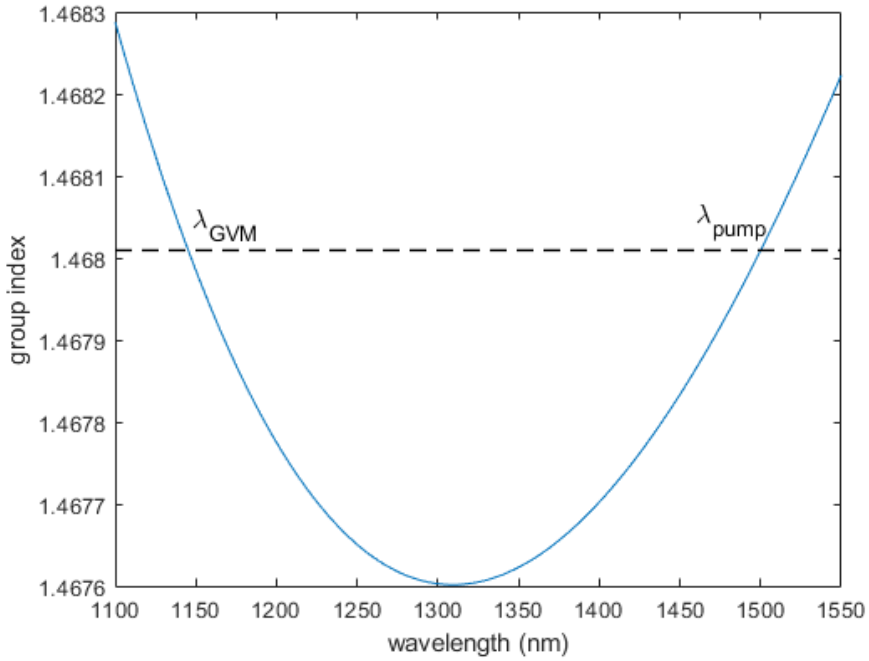

Figure 4.3: Group index of a single mode fiber. For a 1500nm pump soliton, the group velocity matching wavelength λ_{GVM} is 1145nm.

boundary with a positive index change can only satisfy the total reflection condition if the probe pulse is in the normal-dispersion region (see the discussion regarding Eq. (3.11)). For a boundary with a finite duration, such as the boundary induced by a pump pulse, perfect total reflection is not possible because of the presence of tunneling. Nonetheless, we still expect a higher reflectivity if the probe pulse lies in the normal-dispersion region.

We choose the pump pulse to be around 1500 nm, and the probe pulse to be in the range 1145 ± 20 nm. Then, the pump and probe pulses are widely separated in the spectral domain, and we can consider their envelopes separately. Suppose the input pump pulse central frequency is ω_1, while the probe pulse central frequency is near the group velocity matched frequency of ω_1, denoted as ω_2. We use frequency ω_2 to define the probe pulse envelope. Thus, the envelope A in Eq. (4.8) can be decomposed into the pump and the probe parts as:

$$A(z,\tau) = A_1(z,\tau) + A_2(z,\tau)e^{i(\Delta\beta z - \Delta\omega\tau)}, \tag{4.11}$$

where $\Delta\omega = \omega_2 - \omega_1$, $\Delta\beta = \beta(\omega_2) - \beta(\omega_1) - \beta_1(\omega_1)\Delta\omega$, and the subscripts 1 and 2 stand for the pump and probe envelopes, respectively. Substituting the preceding form into Eq. (4.8) and separating the terms in the two spectral regions, we obtain the following two equations:

$$\begin{aligned}\frac{\partial A_1}{\partial z} - \sum_{m\geq 2}\frac{i^{m+1}}{m!}\beta_{m1}\frac{\partial^m A_1}{\partial \tau^m} &= i\gamma A_1(1-f_R)(|A_1|^2 + 2|A_2|^2) \\ &\quad + i\gamma f_R\int_{-\infty}^{\infty} h_R(\tau')(|A_1|^2 + |A_2|^2)(z,\tau-\tau')d\tau', \end{aligned}\tag{4.12}$$

$$\begin{aligned}\frac{\partial A_2}{\partial z} - \sum_{m\geq 2}\frac{i^{m+1}}{m!}\beta_{m2}\frac{\partial^m A_2}{\partial \tau^m} &= i\gamma A_2(1-f_R)(|A_2|^2 + 2|A_1|^2) \\ &\quad + i\gamma f_R\int_{-\infty}^{\infty} h_R(\tau')(|A_2|^2 + |A_1|^2)(z,\tau-\tau')d\tau'. \end{aligned}\tag{4.13}$$

Here, β_{m1} and β_{m2} are the dispersion parameters evaluated at ω_1 and ω_2 respectively. We will use these equations to discuss temporal reflection from ultrashort pump pulses. The terms oscillating at frequencies other than those of the pump and probe were neglected in writing them. This is justified because they are the results of four-wave mixing between the pump and probe, which requires a phase-matching condition that is usually not satisfied in practice. We estimate the "coherence length" of such a process in our experimental conditions (details about experiments are in Chapter 6 and 7). The coherence length of this four-wave mixing process is estimated by $|\Delta\beta|^{-1}$ inversely proportional to the mismatch in the wave vector. In our experiment, this length turns out to be about 0.2 mm, which is much smaller than the interaction length between the pump and probe pulses. Therefore, we can safely neglect this four-wave mixing term in our model.

After separating the envelopes into the pump envelope and probe envelope, the frequency bandwidth of each envelope is actually small enough that β_{m1} and β_{m2} can be neglected for $m > 2$. Furthermore, we consider that the probe pulse is much weaker than the pump pulse so that the terms of $|A_2|^2$ can be neglected in Eq. (4.12) and Eq. (4.13). Then, the pump propagation equation is identical to the form given in Eq. (4.4), and the probe pulse's propagation equation can be simplified to be:

$$\frac{\partial A_2}{\partial z} + \frac{i\beta_{22}}{2}\frac{\partial^2 A_2}{\partial \tau^2} = ib(z,\tau)A_2, \tag{4.14}$$

where the pump-induced change in the refractive index is given as

$$\begin{aligned} b(z,\tau) &= 2\gamma(1-f_R)|A_1(z,\tau)|^2 \\ &\quad + \gamma f_R \int_{-\infty}^{\infty} h_R(\tau')|A_1(z,\tau-\tau')|^2 d\tau' \\ &\approx \gamma(2-f_R)|A_1(z,\tau)|^2 \end{aligned} \tag{4.15}$$

The term on the second line results from the Raman effect. We can also interpret Eq. (4.14) by noting that the pump pulse effectively creates a phase modulation for the probe pulse. This phase modulation is usually called cross-phase modulation. Without the presence of the Raman effect, the strength of this modulation is two times the strength of self-phase modulation Eq. (2.23). However, if the two pulses' frequency difference is much larger than the Raman frequency, as in this case, this ratio would be decreased to $2-f_R$.

Eq. (4.14) resembles Schrodinger's equation in quantum mechanics with $b(z,t)$ representing a barrier. Thus, our temporal-reflection problem is analogous to the scattering of a particle from a barrier in quantum mechanics. When the index change is large enough, we expect the probe pulse to be completely reflected by the pump pulse. However, as the pump pulse exhibits a Raman-induced delay, the exact quantum analog of the temporal reflection would be the reflection from a non-stationary energy barrier.

To study the temporal reflection of a probe pulse on the decelerating soliton shown in Fig. 4.2, we solve Eqs. (4.12) and (4.13) numerically. The parameters for the pump pulse are the same as in Fig. 4.2. For the probe pulse equation, we used $\beta_{22} = 12.3$ ps^2/m. The input pump pulse is at 1500 nm. The probe pulse's spectrum is centered at 1155 nm, 10 nm longer than the group-velocity matching wavelength of 1145 nm. Its shape corresponds to a Gaussian pulse:

$$A_2(0,\tau) = \exp\Big[-\frac{(\tau-T_d)^2}{2T_2^2} - i\delta_i\tau\Big], \tag{4.16}$$

where $T_2 = 1$ ps (corresponds to a FWHM of 1.66 ps) and δ_i is the frequency difference between 1155 nm and 1145 nm. All simulation results in the following of this chapter use this value of δ_i unless stated otherwise. $T_d = 2.5$ ps is the delay of the incident probe pulse with respect to the pump pulse.

The pump pulse propagation result is the same as in Fig. 4.2. Fig. 4.4 shows the evolution of the probe pulse reflecting from the boundary created by the soliton undergoing deceleration. The black dashed line shows the trajectory of the soliton. In part (a), the probe pulse is initially trailing the pump pulse by 2.5 ps, but it's traveling faster and catches up with the pump pulse at a distance of about 10 m. After that distance, most of its energy gets reflected by the pump pulse, while a small fraction of the pulse's energy is transmitted through the pump pulse and appears on its other side. The frequency of the reflected probe pulse has shifted from the incident frequency by about 6 THz, as seen in part (b). We also notice that in the time domain, the reflected pulse first gets narrower before it broadens again, and in the spectral domain, the reflected pulse spectrum becomes wider than the incident pulse.

It is not easy to to calculate analytically the reflectivity of a probe pulse from a red-shifting pump soliton. However, if we make a suitable approximation, we can make some progress. The approximation consists of neglecting the spectral shift of the pump during the reflection process.

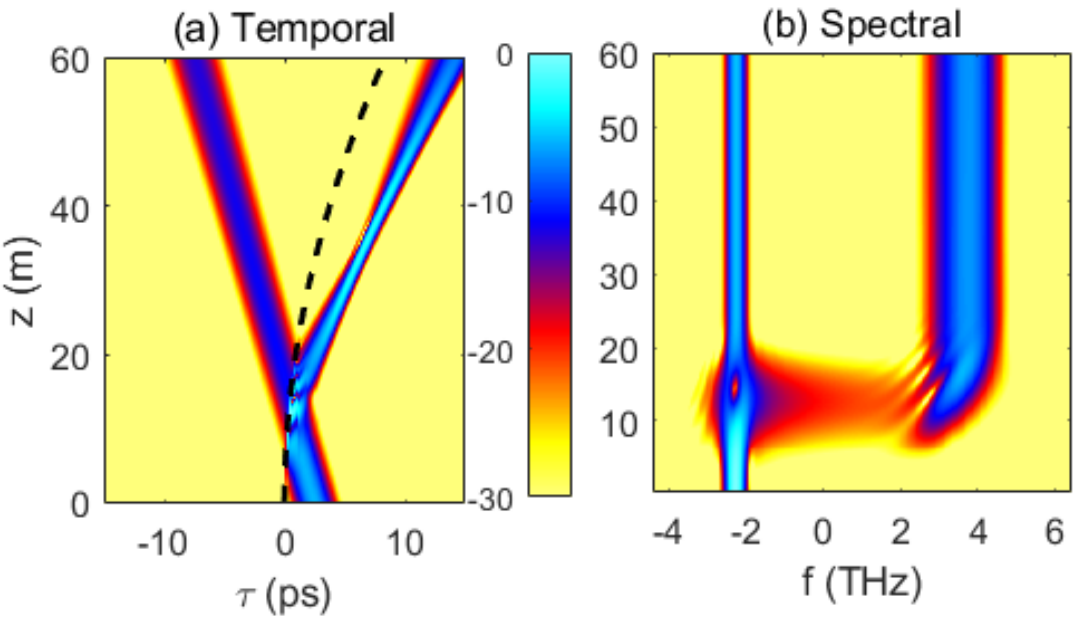

Figure 4.4: Evolution of the probe pulse reflecting from a soliton undergoing Raman red shift. The black dashed line shows the trajectory of the soliton.

In that situation, temporal reflection becomes the quantum analog of a particle scattered by a uniformly moving quantum barrier with a hyperbolic-squared shape. This problem is exactly solvable [78].

We first calculate the frequency of the reflected wave using momentum conservation or the phase-continuity relation [4]. We assume that over the duration that the probe is being reflected, the trajectory of the pump soliton can be treated as being linear. Mathematically, we approximate the pump's trajectory near $z = z_0$ as

$$\tau_b = az^2 \approx a[z_0^2 + 2z_0(z - z_0)], \tag{4.17}$$

where a is a constant given in Eq. (4.7) and z_0 is the location where the center of the incident probe pulse hits the pump pulse. It is calculated from the quadratic equation:

$$az_0^2 = T_d + \beta_{22}\delta_i z_0 \tag{4.18}$$

Under the linear trajectory approximation, we consider the central frequency components of the incident pulse and the reflected pulse. These two plane wave components can be written as

$$A_i \propto e^{i(\Delta\beta_i z - \delta_i \tau)}, \qquad A_r \propto e^{i(\Delta\beta_r z - \delta_r \tau)}. \tag{4.19}$$

Along the boundary, the phase difference between the two waves should remain constant, implying the following equation:

$$\frac{d}{dz}(\Delta\beta_i z - \delta_i \tau_b) = \frac{d}{dz}(\Delta\beta_r z - \delta_r \tau_b) \tag{4.20}$$

with $d\tau_b/dz \approx 2az_0$ obtained from Eq. (4.17). Combined with the dispersion relation $\Delta\beta_j = \beta_{22}\delta_j^2/2$ for $j = i, r$, we obtain the reflected frequency δ_r:

$$\begin{aligned}\delta_r &= \frac{4az_0}{\beta_{22}} - \delta_i \\ &= 2\Omega_{p0}\frac{\beta_{21}}{\beta_{22}} - \delta_i,\end{aligned} \tag{4.21}$$

where Ω_{p0} is the Raman-induced frequency shift (RIFS) of the pump at z_0. Physically, Eq. (4.21) shows that the reflected pulse's frequency depends on the RIFS at the location z_0. In the preceding discussion, we considered the central frequency component of the incident probe pulse. The reflected frequency δ_r calculated from Eq. (4.21) is the central frequency of the reflected pulse.

Under the linear-trajectory approximation, we can use the result from Ref. [78] and write the reflectivity in the form:

$$R = \left[1 + \frac{\sinh^2(\pi D/2)}{\cosh^2(\pi\sqrt{B-1}/2)}\right]^{-1}, \tag{4.22}$$

where $B = 8(2 - f_R)|\beta_{21}/\beta_{22}|$ and $D = (\delta_i - \delta_r)T_1$. Besides the parameter B, the reflectivity depends on D, indicating that the pump's width T_1 plays a role together with the frequency shift of the reflected pulse. The dependence of R on D is shown in Fig. 4.5 for three values of B, where it is shown that high reflectivity occurs for values of D roughly in the range $-5 < D < 5$. It seems from Fig. 4.5 that the use of narrower pump pulses (small T_1) is preferable to enhance the reflectivity. However, a shorter pump pulse also experiences a larger RIFS, not a desirable feature in the present context.

As an example, consider a probe pulse with a Gaussian shape as in Eq. (4.16). If T_d is positive, the pump pulse will slow down because of the RIFS, and the pump and probe pulses will eventually

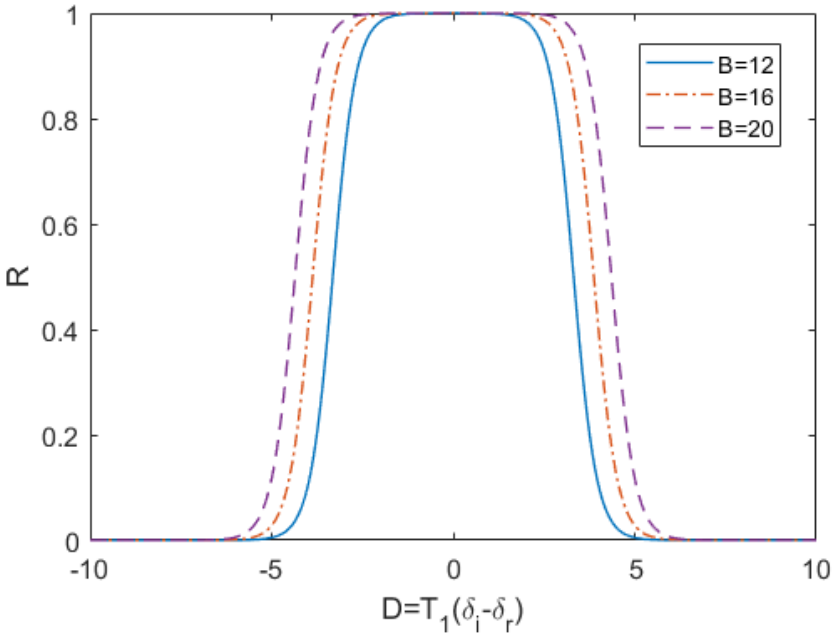

Figure 4.5: Reflectivity as a function of $D = (\delta_i - \delta_r)T_1$ for three values of B based on (4.22).

collide, regardless of the frequency shift δ_i. By explicitly calculating the location z_0 from Eq. (4.18), we find the frequency difference $\delta_r - \delta_i$ explicitly:

$$\delta_r - \delta_i = 2\sqrt{\delta_i^2 + \frac{4aT_d}{\beta_{22}}}. \tag{4.23}$$

We can use this result in Eq. (4.22) to calculate the probe's reflectivity. Although this method is not rigorous, it provides a good estimate within a few percent. Its accuracy degrades for short probe pulses with a large spectral bandwidth because the result in Eq. (4.22) only takes into account the central frequency of the probe pulse. The linear-trajectory approximation becomes less accurate for probe pulses wider than 10 ps. In that case, the leading part of the probe pulse experiences high reflectivity with a small frequency shift, while the opposite occurs for the trailing part. The result is that the central frequency of the reflected pulse is smaller than that calculated from Eq. (4.21).

From Eq. (4.23), we can see that to maximize R, we should choose $\delta_i = 0$, i.e., the probe pulse should be group-velocity matched with the pump pulse at the input end. Additionally, we want the delay T_d to be as small as possible. Its lowest value is limited by the probe pulse's duration because the pump and probe should not overlap at the input end. The minimum value of $\delta_r - \delta_i$ is proportional to $\sqrt{a}$ or scales as $1/T_1^2$. As a result, D scale as $1/T_1$, i.e., the larger T_1 is, the higher the reflectivity becomes. However, a larger T_1 implies a smaller frequency shift. Thus, a trade-off exists between the frequency shift and the conversion efficiency. For negative values of T_d, a collision between the pump and probe pulses does not always occur. Even when the collision occurs, the reflected pulse broadens broaden rapidly, an undesirable feature in practice.

4.4 Temporal Focusing

We have observed numerically a new feature for probe pulses reflected by a short soliton, whose spectrum is affected by the RIFS. When a relatively long probe pulse, initially trailing the pump, hits the pump pulse, the reflected pulse undergoes a temporal focusing phase and becomes shorter than the incident probe pulse, before broadening again, even in a medium exhibiting normal dispersion at the probe's wavelength. This behavior is shown in Fig. 4.6, where we display the temporal focusing for a $T_2 = 2.5$ ps pulse with delay $T_d = 6$ ps. The pump pulse is the same as before. In part (a), the reflected pulse gets narrower before broadening again. This is temporal focusing. We show the reflected pulse shape at the position where it has the smallest width, and compare it with the input pulse in (b). Clearly, the reflected pulse has a much shorter width than the input pulse. The FWHM of the focused pulses is 0.4 ps, and the focusing ratio is 10.4. Temporal focusing is stronger for longer input pulses. However, there are two drawbacks. The first one is that a longer input pulse has a smaller reflectivity. The other one is that when the probe pulse becomes too long, the focused pulse is distorted.

We can use the concept of space-time analogy introduced in Chapter 3 to understand the temporal focusing seen in Fig. 4.6. The new feature in this figure is that reflection occurs at the curved trajectory followed by the pump soliton because of the RIFS. In the spatial domain, the reflection of an optical beam at a parabolic-shape mirror corresponds to this situation. To match with our time-domain case, the bending of the mirror should occur in only one spatial dimension (see Fig. 4.7).

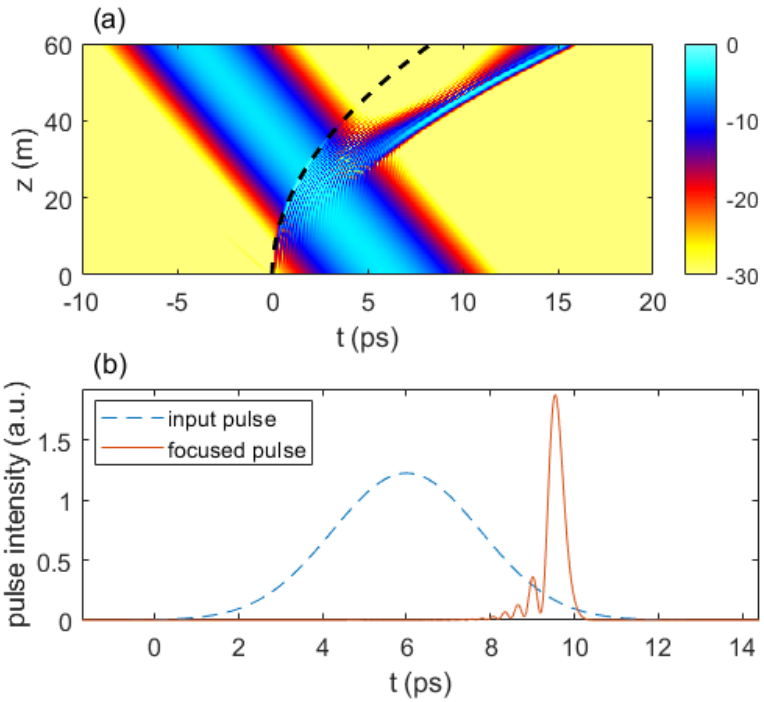

Figure 4.6: Temporal focusing of a $T_2 = 2.5$ ps pulse. The pulse's temporal evolution is shown in (a). The shapes of the focused pulse (at $z = 45$ m, where the reflected pulse has the smallest width) and input pulse are given in (b).

When a Gaussian beam is obliquely incident on such a partially reflecting parabolic mirror, the transmitted beam shape is not affected by the mirror, but the reflected beam is. As seen in Fig. 4.7, the reflected beam undergoes a focusing phase before it broadens. These features help us understand that reflection from a short soliton with a Raman-induced bent trajectory is the temporal analog of focusing by a concave mirror. From scalar diffraction theory, we know that a larger beam, when focused, can be brought down to a smaller size. This explains why temporal focusing is stronger for a longer input pulse. The distortion seen in Fig. 4.6 is the analog of the aberration that occurs when a large beam is obliquely incident on a parabolic mirror.

In Fig. 4.6, we considered the case where the probe pulse trails the pump pulse initially. If the incident probe leads the pump pulse and travels slower than the pump pulse, the pump's trajectory acts as a convex mirror, instead of a concave mirror. In the spatial case, the reflected beam will diverge after hitting a convex mirror. Thus, we expect the reflected pulse to become broader. An example is shown in Fig. 4.8. The reflected pulse has a much wider spectrum and is broadening very fast. This is consistent with our physical intuition.

4.5 Analytical Theory

In this section, we develop an analytical model for the reflected pulse spectrum and use it to discuss the phenomenon of temporal focusing. We focus on the case where the probe pulse trails the pump

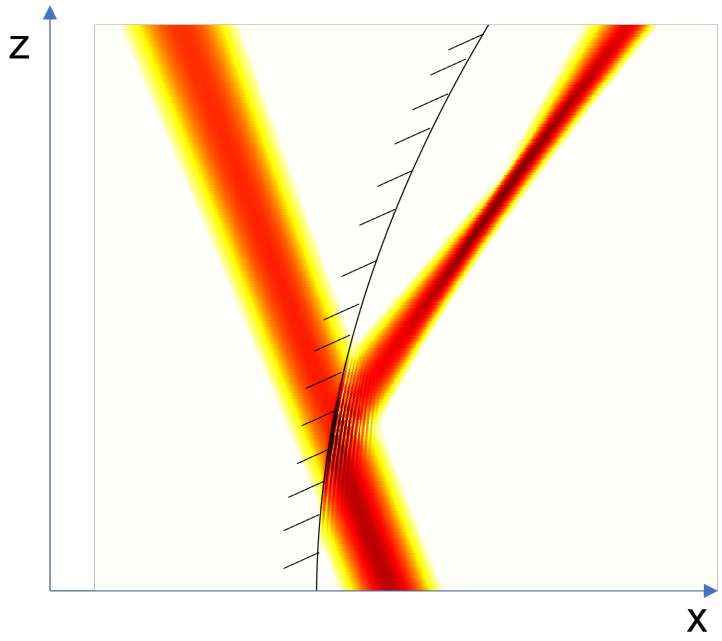

Figure 4.7: Spatial analog: reflection of a Gaussian beam from a partially reflecting parabolic-shape mirror.

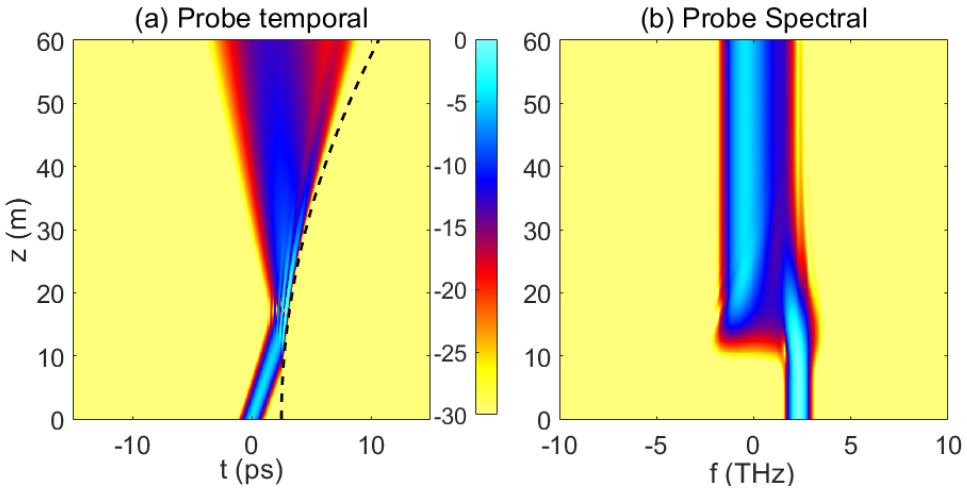

Figure 4.8: Temporal defocusing induced by a pump soliton: (a) temporal evolution, (b) spectral evolution. The 1135-nm probe is a Gaussian pulse with $T_2 = 0.5$ ps and leads the pump pulse by 2.5 ps initially.

pulse initially so that the pump's trajectory acts as a concave mirror.

The probe pulse propagates freely in a dispersive medium before and after the reflection. If we include only the second-order dispersion, their slowly varying envelops evolve as [28]

$$A_i(z,\tau) = \frac{1}{2\pi}\int_{-\infty}^{\infty} \tilde{A}_i(\omega)\exp\left(\frac{i}{2}\beta_{22}\omega^2 z - i\omega\tau\right)d\omega \tag{4.24}$$

$$A_r(z,\tau) = \frac{1}{2\pi}\int_{-\infty}^{\infty} \tilde{A}_r(\omega)\exp\Big(\frac{i}{2}\beta_{22}\omega^2 z - i\omega\tau\Big)d\omega, \tag{4.25}$$

where the second equation applies after the collision of two pulses. The incident field for the Gaussian probe is used from Eq. (4.16). Its use allows us to calculate the initial spectrum $\tilde{A}_i(\omega)$ through a Fourier transform.

At the boundary, the reflected and the incident fields satisfy the relation:

$$A_r(z,\tau_b) = \sqrt{R}A_i(z,\tau_b), \qquad \tau_b = az^2, \tag{4.26}$$

where the reflectivity R is given in Eq. (4.22). Here we have assumed that the R does not change during the whole reflection process, and we can use its value at the center of the probe pulse. Writing $A_r(z,t_b)$ as in Eq. (4.25), we obtain

$$\frac{1}{2\pi}\int \tilde{A}_r(\omega)\exp\Big(\frac{i}{2}\beta_{22}\omega^2 z - ia\omega z^2\Big)d\omega = \sqrt{R}A_i(z,az^2). \tag{4.27}$$

We want to deduce the spectrum of the reflected pulse from the preceding equation. This is not easy but can be done if we employ physical intuition. First, the right side is only non-zero near z_0. Second, the reflected spectrum $\tilde{A}_r(\omega)$ is centered at δ_r given by Eq. (4.21). Based on these observations, we can simplify the left side as

$$\begin{aligned}
&\int \tilde{A}_r(\omega)\exp i(\beta_{22}\omega^2 z/2 - a\omega z^2)d\omega \\
&= \int \tilde{A}_r(\omega)\exp i(\beta_{22}\omega^2 z/2 - a\omega(2z_0 z - z_0^2) - a\omega(z-z_0)^2)d\omega \\
&\approx e^{-ia\delta_r(z-z_0)^2}\int \tilde{A}_r(\omega)e^{ia\omega z_0^2}\exp\left[i(\beta_{22}\omega^2/2 - 2a\omega z_0)z\right]d\omega,
\end{aligned} \tag{4.28}$$

where we replaced ω in the term $a\omega(z-z_0)^2$ with δ_r. As the integral is now related to an inverse Fourier transform, the reflected pulse spectrum is found to be

$$\begin{aligned}
\tilde{A}_r(\omega) = F(\beta_{22}\omega^2/2 - 2az_0\omega)(\beta_{22}\omega - 2az_0) \\
e^{-iaz_0^2\omega}H(\omega - 2az_0/\beta_{22}),
\end{aligned} \tag{4.29}$$

Where $H(x)$ is the step function and $F(k)$ is calculated using

$$F(k) = \sqrt{R}\int A_i(z,az^2)e^{ia\delta_r(z-z_0)^2}e^{-ikz}dz. \tag{4.30}$$

Eq. (4.29) provides an approximate analytic expression for the spectrum of the reflected pulse and is our main result in this section. The step function restricts the frequencies to the range $\omega > 2az_0/\beta_{22}$ to ensure that the reflected pulse stays on the same side of the pump pulse as the incident pulse. To check the accuracy of Eq. (4.29), we compare in Fig. 4.9 its prediction to the numerically obtained spectrum in Fig. 4.4. It is evident that the analytical expression agrees quite well with the numerical results.

For an input Gaussian pulse, $A_i(z,az^2)$ can be calculated analytically. By keeping only terms up to the second order in $z-z_0$, the reflected pulse spectrum can be obtained in a closed form from

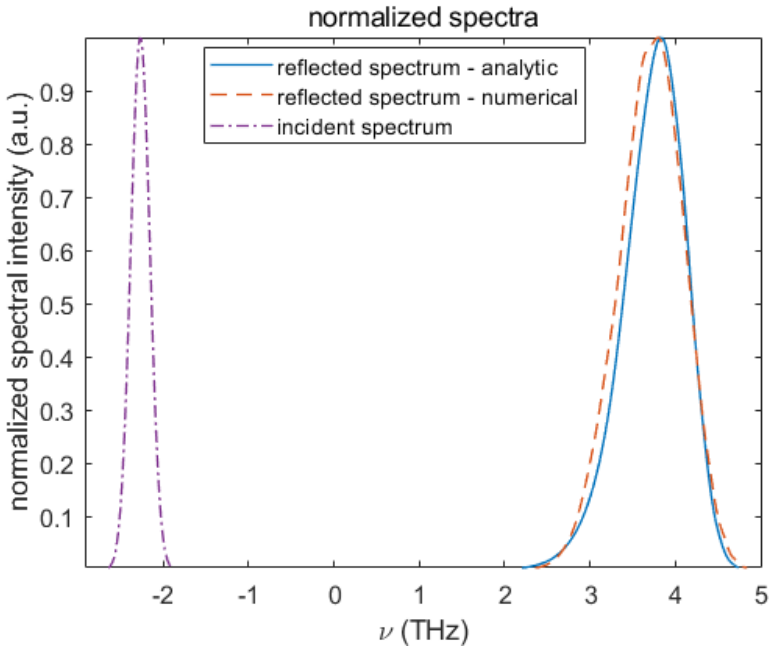

Figure 4.9: Comparison of the analytically predicted and numerically simulated spectra for the pulse reflected pulse using the parameters used for Fig. 4.4. The analytical curve is based on Eq. (4.29). The incident pulse spectrum is also plotted as a reference.

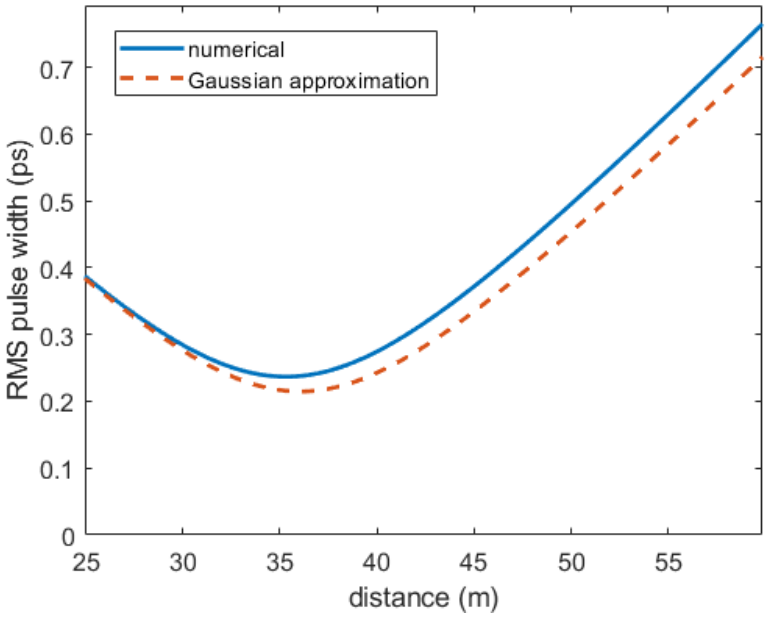

Figure 4.10: The reflected pulse's RMS pulse width as it propagates. The parameters are the same as in Fig. 4.4. The numerical RMS pulse width obtained directly is compared with the RMS pulse width predicted by the Gaussian approximation Eq. (4.32).

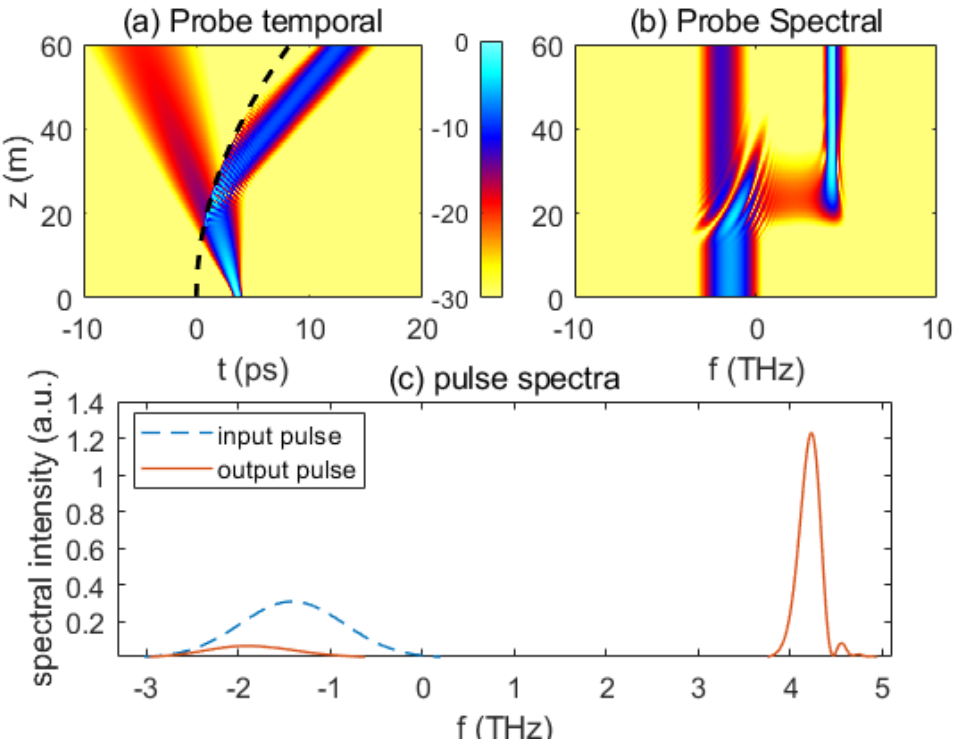

Figure 4.11: Simulation result of a short probe pulse collimated by the Raman soliton.

Eq. (4.29). To simplify the notation, we define a complex q parameter for a Gaussian pulse similar to that for a Gaussian beam and write its spectrum as

$$\tilde{A}_j(\omega) \propto \exp[-q_j(\omega-\omega_0)^2/2], \quad (j=i,\ r). \tag{4.31}$$

The reflected pulse is found to be approximately Gaussian with its central frequency at δ_r. The q parameter of the reflected pulse right after the reflection is given by (for detailed derivation, see Appendix):

$$\frac{1}{q_r(z_0)} = \frac{1}{q_i(z_0)} - \frac{8ia}{\beta_{22}^2(\delta_r-\delta_i)}, \tag{4.32}$$

where $q_i(z_0) = T_2^2 - i\beta_{22}z_0$ is the q parameter of the probe right before the reflection. This equation is similar to the transformation law for the q parameter of Gaussian beams. It shows that the space-time duality between the beams and pulses holds even for the q parameter. Using Eq. (4.32), we can find the spectral and temporal shapes of the reflected pulse. To check the accuracy of the Gaussian approximation, we compare in Fig. 4.10 the analytic prediction of the root-mean-square (RMS) width of the reflected pulse with the numerical values obtained from the simulation shown in Fig. 4.4. One can conclude that the Gaussian approximation works reasonably well.

Eq. (4.32) can be used to understand the temporal focusing phenomenon discussed earlier. For a longer incident pulse, $q_i(z_0) \approx T_2^2$, and the second term of Eq. (4.32) gives rise to a positive imaginary part of $q_r(z_0)$. This corresponds to a negative chirp, and as it propagates, the chirp gets compensated by the dispersion and the pulse becomes shorter than the incident pulse.

One interesting phenomenon occurs when a shorter input probe pulse is considered. In this case, the imaginary part in $q_i(z_0)$ cannot be neglected, resulting in a positive imaginary part in

$1/q_i(z_0)$. This imaginary part can be cancelled by the second term in Eq. (4.32). In Fig. 4.11, we show such a result. The input pulse is a short pulse with $T_2 = 200$ fs. The frequency shift from the reference frequency $\delta_i/(2\pi) = -1.42$ THz and the delay is 3.69 ps. In Fig. 4.11(a), we see that, before the reflection, the pulse is broadening very fast because it's short. After hitting the boundary and reflecting, the reflected pulse maintains its width without broadening. This is the temporal analog of collimation. Physically, the chirp generated during the propagation gets canceled by the reflection on a curved boundary. In the spectral domain, part (c) shows that the reflected pulse has a much smaller spectral width than the incident pulse. This suggests that it may be possible to use this phenomenon to realize spectral compression.

4.6 Conclusion

In this chapter, we performed a more realistic study of temporal reflection. We discussed how to create the boundary of index change via a pump-probe scheme, and how to choose the pump and probe wavelengths based on the dispersion properties of the medium.

We utilized the pulse propagation equation to model the pump-probe interaction in the medium, with an optical fiber as an example. We considered using an optical soliton as a pump pulse to create the index boundary, and showed that the Raman scattering induces a continuous red shift and deceleration of the soliton, resulting in a boundary with deceleration.

We further numerically studied the temporal reflection of the probe pulse on this type of decelerating boundary. We observed that the reflected pulse becomes narrower under conditions that lead to a novel type of temporal focusing. This phenomenon is explained through space-time duality based on the similarity between the pulse propagation in a dispersive medium and beam propagation in the paraxial approximation. We showed that the temporal situation in our case is analogous to an optical beam incident obliquely on a parabolic mirror. Using this physical picture, we showed that temporal reflection can lead to focusing, defocusing, or collimation of optical pulses, just like a curved mirror can do so for optical beams. We were able to obtain an approximate analytic expression for the reflected pulse's spectrum and use it to derive the temporal version of the transformation law for the q parameter associated with Gaussian beams.

It is worth noting that similar effects should also take place if the pump pulse accelerates or decelerates for some other reasons, for example, if it is an Airy pulse [79], or if the optical fiber changes its property along the propagation direction, such as using a tapered fiber.

We would also like to point out that the interaction of Raman soliton with a probe pulse was also discussed in [80, 81]. They focused on a more mathematically involved treatment. The discussion in this chapter provides a more intuitive picture to understand the physics.

Chapter 5

Temporal Waveguides

In the previous chapters, we introduced and analyzed temporal reflection that takes place when a moving boundary of refractive index is created inside a dispersive medium. As shown in Chapter 3, under appropriate condition, total reflection can take place. Based on this idea, Plansinis et al. [23, 24] showed that two moving boundaries that are separated in time can form a temporal waveguide that confines pulses to the time window created by the two boundaries. Similar to a spatial waveguide, such a temporal waveguide has a set of modes with different shapes that propagate inside the temporal waveguide without any distortion.

For a temporal waveguide, if we consider using two short solitons to create the boundaries, similar to what we discussed in Chapter 4, we also need to take into account the deceleration of these solitons as the result of Raman-induced red shift.

When two Raman solitons are created by a pair of short identical pump pulses, separated in time by a fixed delay, they form a temporal waveguide that is different from the waveguides studied earlier [24]. Because of intrapulse Raman scattering, both Ramam solitons slow down identically, and the temporal window associated with the waveguide shifts in time continuously. In this chapter, we study the evolution of a trapped probe pulse in such a decelerating temporal waveguide. We show that this type of temporal waveguide is analogous to a spatial waveguide whose core is curved or bent. Similar to the spatial case, the bending leads to coupling among different modes of the waveguide. We show that a trapped probe pulse undergoes periodic changes in its shape resulting from mode coupling, while its spectrum blue-shifts continuously to ensure that its speed matches the speed of pump pulses. We develop an analytic approach based on coupled-mode theory and show that its predictions agree well with the numerical results.

It is also worth mentioning some of the relevant research. In the context of supercontinuum generation in optical fibers, the trapping of dispersive wave by a soliton can occur under certain conditions [82, 83, 84, 85, 86, 87, 88]. Our study here has similar physics, but our analysis provides additional insight.

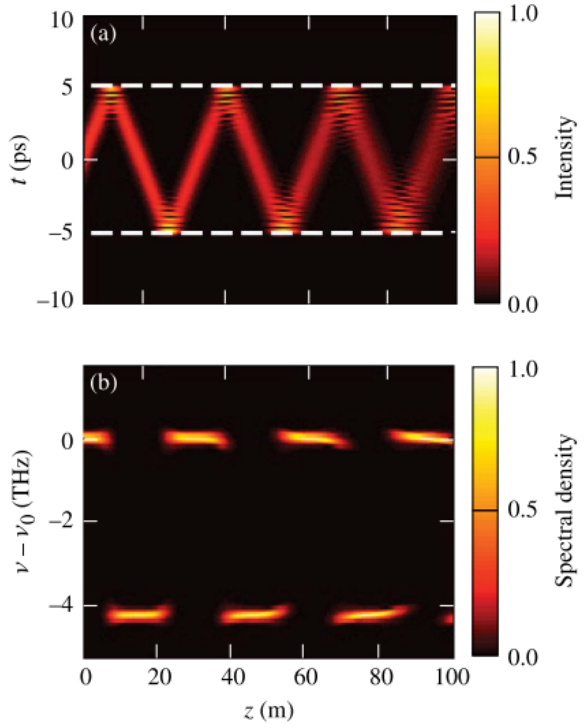

Figure 5.1: Cited from [23]. Simulation of Eq. (5.1). The input pulse is a Gaussian pulse.

5.1 Modeling of Temporal Waveguides

First, we briefly discuss the idea of a temporal waveguide proposed by Plansinis et al [23]. They used the pulse propagation equation given in Eq. (3.4):

$$\frac{\partial A}{\partial z} + \Delta\beta_1 \frac{\partial A}{\partial \tau} + \frac{i\beta_2}{2}\frac{\partial^2 A}{\partial \tau^2} = iB(\tau)A, \tag{5.1}$$

To form a temporal waveguide, they considered a rectangle function for $B(\tau)$:

$$B(\tau) = \begin{cases} \beta_B \text{ , if } |\tau| < T_B \\ 0 \text{ , otherwise.} \end{cases} \tag{5.2}$$

This profile of index change contains two boundaries, and total reflection can take place at the two boundaries back and forth, similar to the ray reflecting on the interface of core-cladding in an optical fiber.

In Ref. [23], the numerical simulations based on Eq. (5.1) were used. We show the figure here in Fig. 5.1 taken from Plansinis' work. We can see that the incident pulse undergoes cascaded temporal reflections with the two boundaries, trapping the pulse between the two boundaries. We can view this as the temporal analog of a spatial waveguide. Similar to a spatial waveguide, a temporal waveguide also has several supported modes. These modes are specific pulse shapes that do not distort during propagation in the temporal waveguide.

5.2 Raman-induced Bending of a Temporal Waveguide

If we consider the two boundaries of the waveguide created by two solitons, we need to study the propagation of the two solitons as well as the probe pulse trapped between the solitons. We will use the models we introduced in Chapter 4. The equations governing the pump (soliton) and probe pulses' propagation are given by Eqs. (4.12) and (4.13). We numerically solve these equations with the input:

$$A_1(0,\tau) = \sqrt{P_1}\left[\operatorname{sech}\left(\frac{\tau - \Delta T/2}{T_1}\right) + e^{i\frac{\pi}{2}}\operatorname{sech}\left(\frac{\tau + \Delta T/2}{T_1}\right)\right], \tag{5.3}$$

$$A_2(0,\tau) = \sqrt{P_2}\exp\left(-\frac{\tau^2}{2T_2^2}\right), \tag{5.4}$$

where ΔT is the separation between the two pump pulses of width T_1. Their peak power is chosen such that $P_1 = |\beta_{21}|/\gamma T_1^2$ corresponds to a fundamental soliton. The 90° phase shift between the two pump pulses is introduced to prevent any nonlinear interaction between them [28]. The probe pulse has a Gaussian shape and its width T_2 is chosen to be considerably larger than that of pump pulses. In contrast, the peak power P_2 of the probe is much smaller compared to that of the pump pulses to prevent its influence on the pump pulse.

As a specific example, we choose $T_1 = 200$ fs, $T_2 = 1$ ps, and $\Delta T = 5$ ps. The width of the probe pulse approximately matches the fundamental mode of the temporal waveguide formed by two pump pulses. The values of dispersion parameters, $\beta_{21} = -\beta_{22} = -13.4$ ps^2/km and $\beta_{31} = \beta_{32} = 0.07$ ps^3/km, correspond to a silica fiber pumped at 1500 nm. All dispersion terms higher than third order were neglected in our simulations. The nonlinear coefficient γ is 2 W$^{-1}\cdot$km^{-1}. Figure 5.2 shows the temporal and spectral evolution of the pump (top) and probe (bottom) pulses for a 1-km-long fiber. As expected, the spectrum of pump pulses continuously red-shifts because of intrapulse Raman scattering. In the time domain, the trajectory of pump pulses is bent in a parabolic fashion because their deceleration caused by the spectral red shift produces a time delay varying as z^2. These are the same for the single soliton case discussed in the previous chapter.

The evolution of the probe pulse in Figure 5.2(c) shows clearly that it is trapped within the temporal waveguide formed by two solitons. In the absence of pump pulses, the probe's trajectory would be vertical, its spectrum would remain unchanged, and its width would increase because of dispersion. When the two pump pulses form a waveguide, the probe pulse is trapped between them and is forced to decelerate with them. In the spectral domain, the probe's spectrum shifts toward higher frequencies (a blue shift), and this shift is required for its speed to decrease. An interesting feature seen in Fig. 1(d) is that, although the pump's spectrum red-shifts linearly with distance, the probe's spectrum does not do so. It exhibits a periodic evolution pattern in addition to the blue shift. In the time domain, the probe pulse also changes its shape in a periodic fashion. To understand the origin of these features, we develop a semi-analytic approach in the next section. It reveals that the decelerating temporal waveguide is the temporal analog of a bent (or curved) spatial waveguide. The periodic spatial and temporal features result in both cases from the coupling between the waveguide's modes induced by such bending.

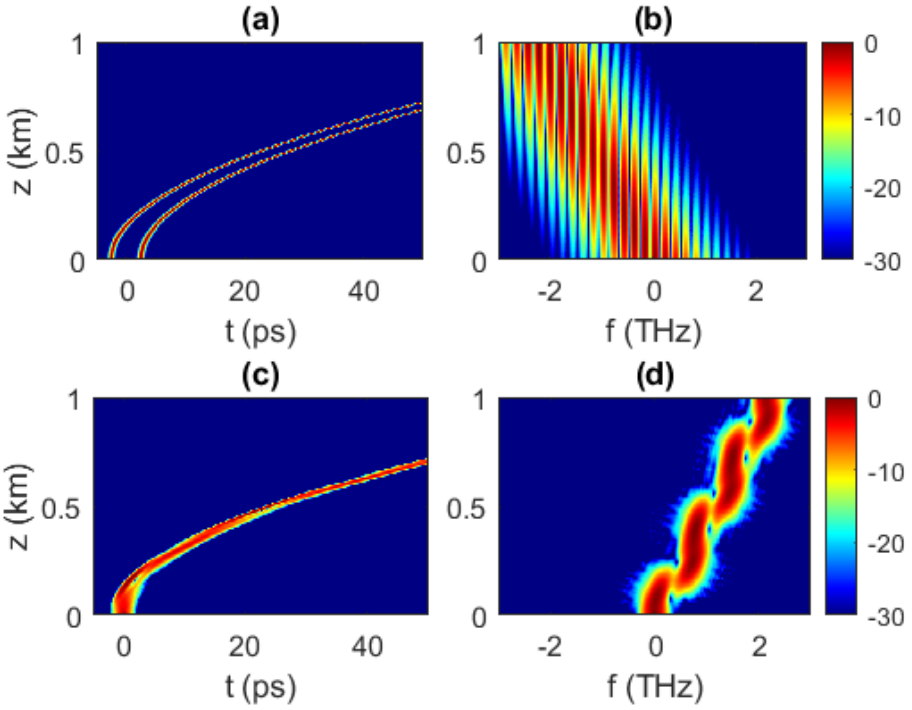

Figure 5.2: Temporal (a, c) and spectral (b, d) evolutions of pump (top) and probe (bottom) pulses over a 1-km-long fiber. The probe pulse is trapped within the temporal waveguide formed by two Raman solitons. The intensity is plotted on a logarithmic (dB) scale.

5.3 A Non-inertial Reference Frame

If the probe pulse is weak enough, and the two solitons are separated far enough that they do not interact, then each soliton's evolution is governed by Eq. (4.6). The probe pulse propagation is still given by Eq. (4.14), except that $b(z,\tau)$ contains a contribution from two solitons.

Since the soliton experiences a quadratic delay as it propagates down as a result of Raman red shift, we introduce a non-inertial frame where the soliton now appears stationary:

$$\tilde{\tau} = \tau - az^2. \tag{5.5}$$

In this frame, the temporal shape of each pump pulse power does not change with z, i.e., $|A_1(z,\tilde{\tau})|^2 = |A_1(0,\tilde{\tau})|^2$. Eq. (4.14) then is transformed into:

$$\frac{\partial A_2}{\partial z} - 2az\frac{\partial A_2}{\partial \tilde{\tau}} + \frac{i}{2}\beta_{22}\frac{\partial^2 A_2}{\partial \tilde{\tau}^2} = ib(\tilde{\tau})A_2, \tag{5.6}$$

where we kept only the dominant $m = 2$ dispersion term and defined $b(\tilde{\tau})$ as

$$\begin{aligned} b(\tilde{\tau}) &= 2\gamma(1-f_R)|A_1(\tilde{\tau})|^2 + \gamma f_R \int_{-\infty}^{\infty} h_R(\tilde{\tau}')|A_1(\tilde{\tau}-\tilde{\tau}')|^2 d\tilde{\tau}' \\ &\approx \gamma(2-f_R)|A_1(\tilde{\tau})|^2. \end{aligned} \tag{5.7}$$

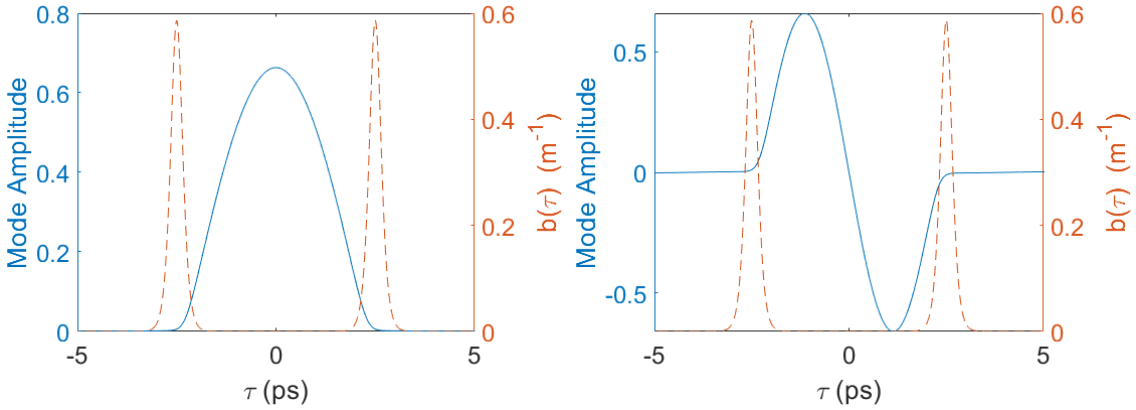

Figure 5.3: First two modes of the temporal waveguide formed by two solitons with $T_1 = 0.2\,\text{ps}$ and $\Delta T = 5\,\text{ps}$.

The approximate form of $b(\tilde{\tau})$ holds for probe pulses considerably wider than pump pulses.

We use Eq. (5.6) in the next section to find the waveguide modes and to study the Raman-induced coupling among them. If the second term containing the parameter a is absent in this equation, its form becomes identical to the one-dimensional Schrödinger equation, with z playing the role of time and $b(\tilde{\tau})$ acting as the potential created by the pump pulses. The term containing a results from the use of a non-inertial frame and its dependence on z makes the Hamiltonian "time-dependent." It perturbs a temporal waveguide such that its modes keep changing with z.

5.4 Coupled-Mode Equations

We write Eq. (5.6) in the form of a Schrödinger equation as

$$-i\frac{\partial A_2}{\partial z} = \hat{H}(z)A_2(z,\tilde{\tau}), \tag{5.8}$$

where the Hamiltonian is given by

$$\hat{H}(z) = -\frac{\beta_{22}}{2}\frac{\partial^2}{\partial\tilde{\tau}^2} - 2iaz\frac{\partial}{\partial\tilde{\tau}} + b(\tilde{\tau}). \tag{5.9}$$

Recalling that z plays the role of time and $\tilde{\tau}$ that of a spatial coordinate, Eq. (5.8) shows that we are dealing with a time-dependent Hamiltonian. We can find the eigenmodes of this Hamiltonian for any value of z, but they will evolve with z. We adopt the approach used for a harmonic oscillator whose frequency varies with time [35].

Let $\psi_p(z,\tilde{\tau})$ be the pth eigenmode of the Hamiltonian with the eigenvalue $\Delta\beta_p(z)$, i.e.,

$$\hat{H}(z)\psi_p(z,\tilde{\tau}) = \Delta\beta_p(z)\psi_p(z,\tilde{\tau}). \tag{5.10}$$

The eigenmodes at $z = 0$ can be found numerically using the same parameters as those in Fig. 5.2. The first and second-order modes are shown in Fig. 5.3. The two modes resemble the eigenmodes of a quantum well because each soliton acts as a high-index barrier.

In Eq. (5.9), the second term containing az has its origin in the group-velocity mismatch between the pump and probe pulses. This mismatch can be compensated if the probe pulse shifts its frequency to match the group velocity of the pump. Based on this concept, the eigenmodes and eigenvalues of Eq. (5.10) at any distance z are found to be

$$\psi_p(z,\tilde{\tau}) = \psi_p(0,\tilde{\tau})\exp(-i2az\tilde{\tau}/\beta_{22}) \tag{5.11}$$

$$\Delta\beta_p(z) = \Delta\beta_p(0) - 2a^2z^2/\beta_{22}. \tag{5.12}$$

It is easy to conclude that the temporal shape of the eigenmodes does not change on propagation, but they undergo a frequency shift that increases linearly with the propagation distance. This shift has its origin in the linear red shift of pump pulses resulting from intrapulse Raman scattering. However, its sign is opposite to that of pump pulses, indicating that the mode frequencies shift toward the blue side.

Let us consider the situation in which a specific eigenmode, say $\psi_p(0,\tilde{\tau})$, is excited at the input end of the temporal waveguide. If $\hat{H}(z)$ changes slowly enough that the adiabatic approximation holds, this mode will evolve to become $\psi_p(z,\tilde{\tau})$, without coupling to other modes [35]. From Eq. (5.12), the mode shape will not change even though its frequency will shift toward the blue side.

In general, a probe pulse will excite multiple modes of the temporal waveguide, and its shape will change because of the coupling among different modes taking place during its propagation. To study this mode coupling, we decompose the probe pulse into the eigenmodes of $\hat{H}(z)$ as

$$A_2(z,\tilde{\tau}) = \sum_p C_p(z)\psi_p(z,\tilde{\tau}). \tag{5.13}$$

Using this expansion in Eq. (5.8), we obtain

$$\sum_p \frac{dC_p}{dz}\psi_p + \sum_p C_p\frac{\partial\psi_p}{\partial z} = i\sum_p C_p\Delta\beta_p\psi_p \tag{5.14}$$

After decomposing $\partial\psi_p/\partial z$ in terms of the eigenmodes, we obtain the following evolution equation for the modal amplitudes [35]:

$$\frac{dC_p}{dz} + \sum_n d_{pn}C_n = iC_p\Delta\beta_p, \tag{5.15}$$

where $d_{pn} = <\psi_p|\frac{\partial\psi_n}{\partial z}>$ is given by

$$d_{pn} = -\frac{2ia}{\beta_{22}}\int_{-\infty}^{\infty}\tilde{\tau}\psi_p^*(0,\tilde{\tau})\psi_n(0,\tilde{\tau})d\tilde{\tau} = -\frac{2ia}{\beta_{22}}T_{pn}. \tag{5.16}$$

Noting that $\psi_p(0,\tilde{\tau})$ is real, T_{pn} is defined as

$$T_{pn} = T_{np} = \int_{-\infty}^{\infty}\tilde{\tau}\psi_p(0,\tilde{\tau})\psi_n(0,\tilde{\tau})d\tilde{\tau}. \tag{5.17}$$

The last term in Eq. (5.15) can be eliminated with the transformation:

$$C_p(z) = E_p(z)\exp\left(i\int_0^z\Delta\beta_p(z')dz'\right). \tag{5.18}$$

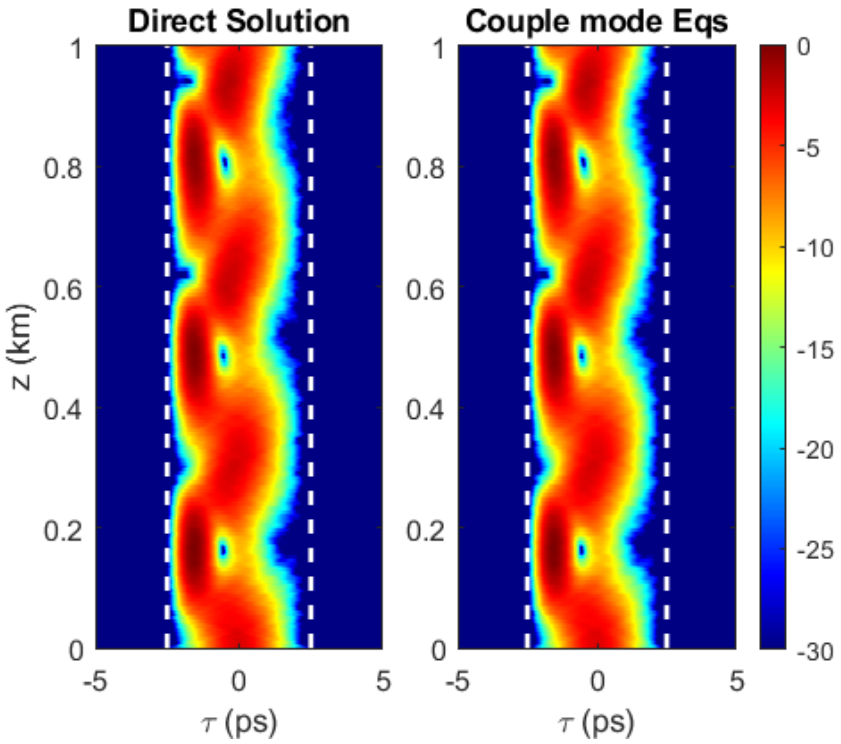

Figure 5.4: Temporal evolution of probe pulse in the non-inertial frame with the same parameter values used in Fig. 5.2. Left: solution of Eq. (5.6). Right: solution based on the coupled-mode equations in Eq. (5.19).

In terms of E_p, the set of coupled-mode equations takes the form:

$$\frac{dE_p}{dz} = \frac{2ia}{\beta_{22}} \sum_n T_{pn} e^{ib_{np}z} E_n, \tag{5.19}$$

where b_{np} is defined as

$$b_{np} = \Delta\beta_n(z) - \Delta\beta_p(z) = \Delta\beta_n(0) - \Delta\beta_p(0). \tag{5.20}$$

This set of relatively simple equations governs the Raman-induced coupling of the modes of a temporal waveguide. Notice that only the difference of initial eigenvalues at $z = 0$ appears in Eq. (5.20) because all eigenvalues change with z by the same amount in Eq. (5.12). Note that in this case, there is no geometrical phase because $T_{nn} = 0$ from the parity symmetry of the eigenmode.

Using the same parameter values used for Fig. 5.2, we simulated the probe pulse propagation in the non-inertial frame in two different ways. The results are shown in Fig. 5.4, where we plot the temporal evolution of the probe pulse in a 1-km-long fiber. On the left side, we solved directly the wave equation given in Eq. (5.6). Results shown on the right side were obtained by solving the coupled mode equations in Eq. (5.19). In both cases, white dashed lines show the trajectories of the pump solitons that become vertical (no temporal shift) in the non-inertial frame used here. The probe pulse, trapped between the two pump solitons, undergoes periodic changes in its shape, which become more apparent in the non-inertial frame, compared to the results shown in Fig. 5.2.

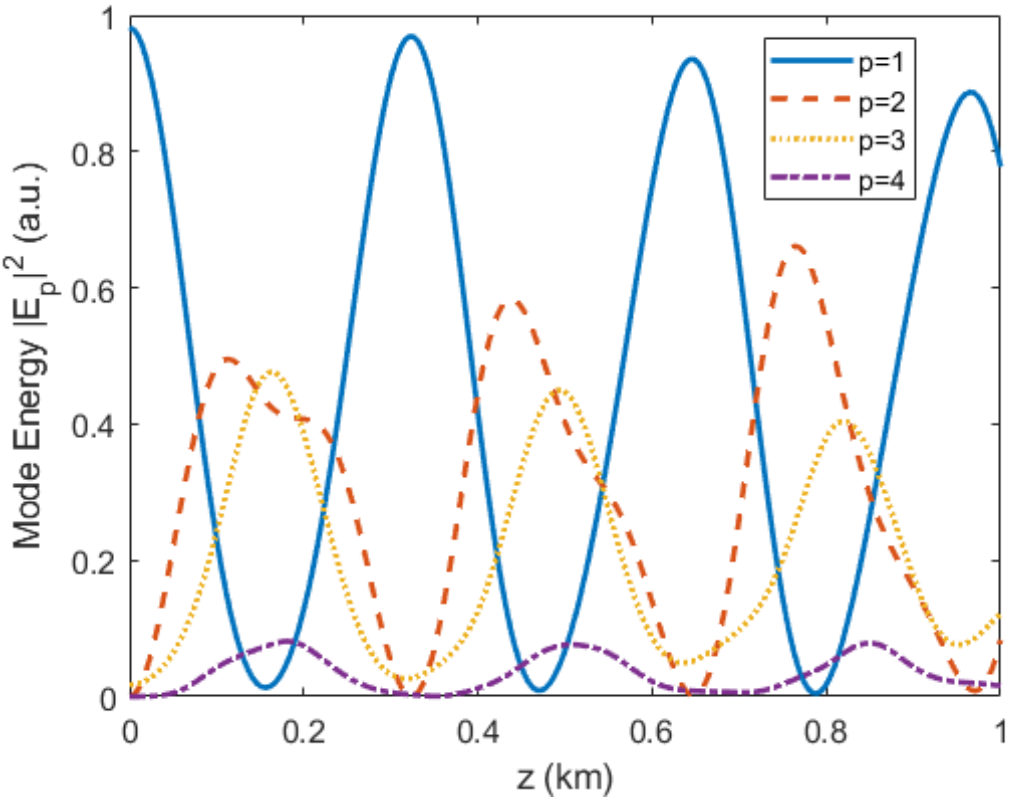

Figure 5.5: Changes occurring with distance in the distribution of pulse's energy among different modes. Parameter values are the same as in Fig. 5.2.

The excellent agreement between the two approaches verifies the accuracy of our coupled-mode equations and justifies the approximations made in their derivation.

It should be apparent from Eq. (5.19) that $|E_p(z)|^2$ is a good measure of the fraction of energy of the probe pulse in a specific mode of the temporal waveguide at a distance z. Changes in the distribution of energy in different modes of the waveguide are shown in Fig. 5.5. As seen there, even though the first mode carries most energy initially at $z = 0$, coupling of this mode to higher-order modes leads to transfer of energy to other modes in a periodic fashion. This energy transfer manifests as periodic changes in the probe pulse's shape in Fig. 5.4. However, the total energy of all the modes is conserved during the propagation. This is because the probe pulse remains trapped during propagation and there is no energy exchange between the pump and probe.

5.5 Model Based on Two Modes

Mode coupling is an undesirable feature for practical applications. For example, the blue shift of the probe's spectrum can be useful for frequency conversion applications. However, because of mode coupling, probe pulse's spectrum does not shift to the blue side in a controlled fashion. In this section, we use the coupled-mode equations to find the conditions under which coupling of the

fundamental mode to its neighboring modes can be largely suppressed. In this situation, a temporal waveguide can be used to shift the probe' spectrum toward the blue side in an adiabatic fashion.

We have seen in Section 5.4 that the evolution of a probe pulse is governed by a z-dependent Hamiltonian. When the Hamiltonian changes slowly with z, the fundamental mode evolves adiabatically, without coupling to neighboring modes of the waveguide. Close to this adiabatic limit, mode coupling is relatively weak, and the fundamental mode should couple only to the second mode. This suggests that we can get considerable physical insight by considering only the first two modes in Eq. (5.19) and solving the following set of two coupled equations:

$$\frac{dE_1}{dz} = \frac{2ia}{\beta_{22}} T_{12} e^{ib_{21}z} E_2, \quad \frac{dE_2}{dz} = \frac{2ia}{\beta_{22}} T_{12} e^{-ib_{21}z} E_1. \tag{5.21}$$

The preceding equations are identical to those obtained for a directional coupler and can be solved easily because of their linear nature. Assuming that only the fundamental mode is excited at the input end, the energy in the second-order mode is found to be

$$|E_2(z)|^2 = |E_1(0)|^2 \Big(\frac{4aT_{12}}{\beta_{22}K}\Big)^2 \sin^2 \frac{Kz}{2} \tag{5.22}$$

where

$$K = \sqrt{b_{21}^2 + (4aT_{12}/\beta_{22})^2}. \tag{5.23}$$

Similar to a directional coupler, the mode's energy oscillates with z with the period $L_p = 2\pi/K$ and becomes maximum in the middle of each period. Using Eq. (5.22), the maximum energy fractional energy in the second order mode is

$$\frac{|E_2(z)|^2_{max}}{|E_1(0)|^2} = \frac{F}{1+F}, \tag{5.24}$$

where the parameter F is introduced as

$$F = (4aT_{12}/\beta_{22}b_{21})^2. \tag{5.25}$$

When a temporal waveguide is designed to ensure $F \ll 1$, almost all energy of the probe pulse remains in the fundamental mode, and the mode evolves in an adiabatic fashion. When F becomes close to 1, the fundamental mode does not evolve adiabatically. The two-mode model ceases to apply for $F > 1$ because coupling to higher-order modes cannot be ignored. For the results shown in Figs. 5.4 and 5.5, the estimated value of F is 6.5. It is evident that more than two modes should be included for such large values of F. The main conclusion is that the mode coupling can be made negligible by ensuring that $F \ll 1$.

The expression for F in Eq. (5.25) depends on T_{12}, whose value can be calculated from Eq. (5.17) but requires the mode profiles that must be obtained numerically. To estimate the values of F as simply as possible, we assume that pump pulses are so short compared to the probe pulse that we can treat the waveguide as a quantum well of width ΔT, surrounded by walls of infinite potentials. The eigenfunctions and eigenvalues of such a quantum well are known in an analytic form, and they can be used to find the parameters T_{12} and b_{21} in Eq. (5.25). The use of these parameters leads to the following expression for F:

$$F \approx 1.68 \times 10^{-4} T_R^2 \Delta T^6 / T_1^8. \tag{5.26}$$

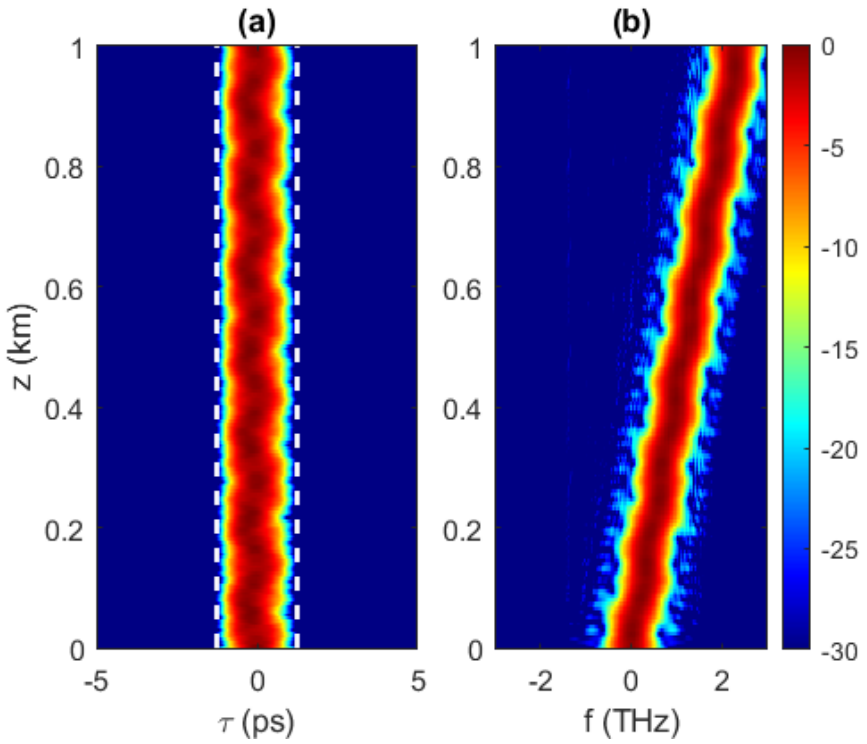

Figure 5.6: (a) Temporal and (b) spectral evolution of a probe pulse ($T_2 = 0.5$ ps) inside a temporal waveguide with $\Delta T = 2.5$ ps.

We stress that Eq. (5.26) provides only a rough estimate of F and should be used only for a qualitative understanding. To estimate the numerical value of F for optical fibers, we use the $T_R = 3$ fs. F depends both on the widths and spacing of two pump pulses used as temporal boundaries. High powers of both of these parameters in Eq. (5.26) indicates that mode coupling is very sensitive to the values of both of them. To make F small, we need to either increase T_1 or decrease ΔT. Increasing T_1 decreases the Raman-induced red shift and reduces bending of the waveguide. In practice, the delay ΔT between the two pump pulses is easily controlled. Its lower values reduce the waveguide's width and increase the difference in eigenvalues of different waveguide modes.

As seen in Eq. (5.26), F varies as $(\Delta T)^6$. Thus, decreasing ΔT by 50% should suppress mode coupling significantly for the situation shown in Fig. 5.5. We keep all other parameters the same but choose $\Delta T = 2.5$ ps and $T_2 = 0.5$ ps. The results are shown in Fig. 5.6. The temporal evolution of the probe pulse should be compared to that in Fig. 5.4. Clearly, distortion of the probe pulse is reduced considerably. Note also that the probe's spectrum shifts toward the blue much more smoothly. The value of the parameter F is 0.0648 for the parameters used here. As $F \ll 1$, the modal coupling should be relatively weak. This is indeed the case in Fig. 5.7, where the fractional energy of each mode is shown as a function of z using the coupled-mode equations. The fundamental mode dominates, and only a small fraction of its energy is transferred to the second mode in a periodic fashion. The results of the two-mode theory Eq. (5.22) agree well with the solution of the full coupled mode equations Eq. (5.19) for such small values of F.

For completeness, we also consider the strong-coupling case by increasing the separation between the two pump pulses to 10 ps. The resulting temporal waveguide supports a large number of

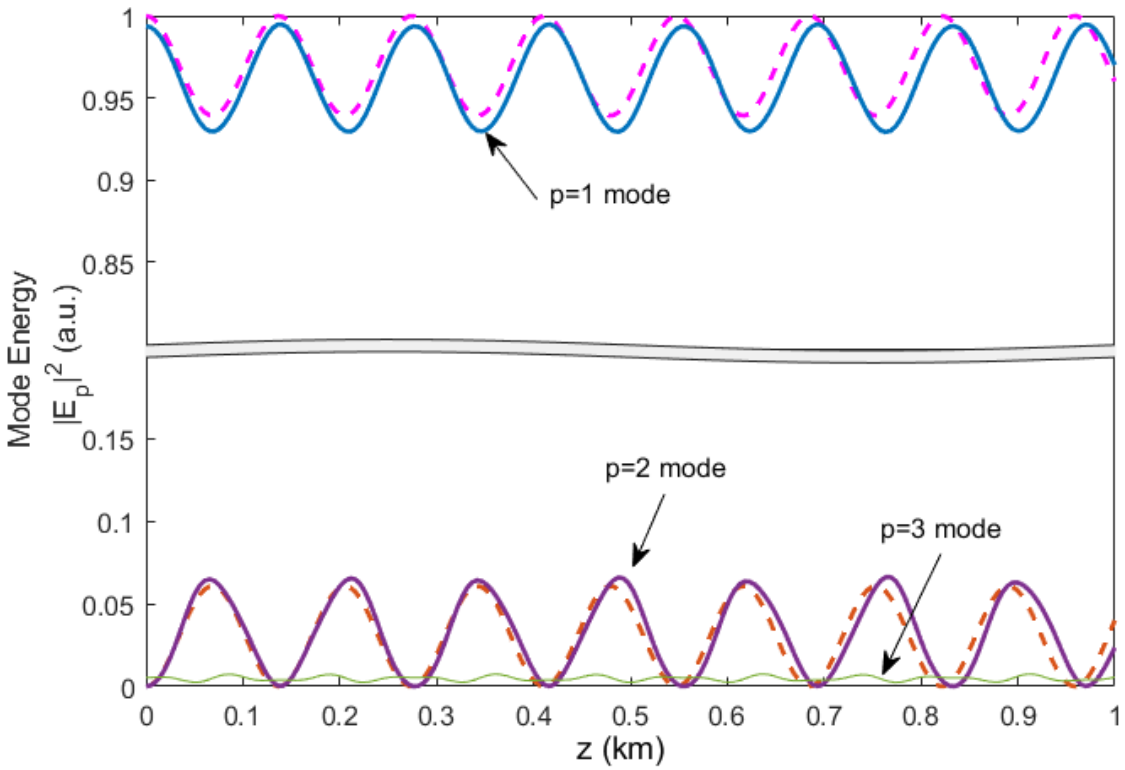

Figure 5.7: Mode energies evolution in a 2.5ps temporal waveguide in Fig. 5.6. Dashed lines show the result from the two-mode theory.

modes. The parameter F is 546 for this waveguide, indicating that mode coupling would lead to pulse distortion that is much more severe than that seen Fig. 5.4. The results are shown in Fig. 5.8 for a probe pulse with $T_2 = 2$ ps. Coupling among a large number of modes distorts the shape of probe pulses severely, and the pulse's spectrum does not blue shift in a regular fashion.

5.6 Conclusion

In this chapter, we have studied the propagation of optical pulses inside a temporal waveguide, formed by two short pump pulses solitons acting as high-index barriers. The wavelength of pump pulses is chosen such that they form solitons inside a dispersive nonlinear medium such as an optical fiber. The solitons are short enough that they decelerate as their spectra shift continuously toward the red side because of intrapulse Raman scattering. We show that the temporal waveguide formed by such solitons is not stationary, and the situation is analogous to a three-layer waveguide whose core is curved in space.

We use the coupled pump-probe equations to show that a probe pulse shifts its spectrum toward the blue side to match its speed with that of pump pulses so that it remains trapped inside such a temporal waveguide. However, the shape of the probe pulse evolves in a periodic fashion inside the waveguide. To understand this behavior, we make use of a non-inertial reference frame for

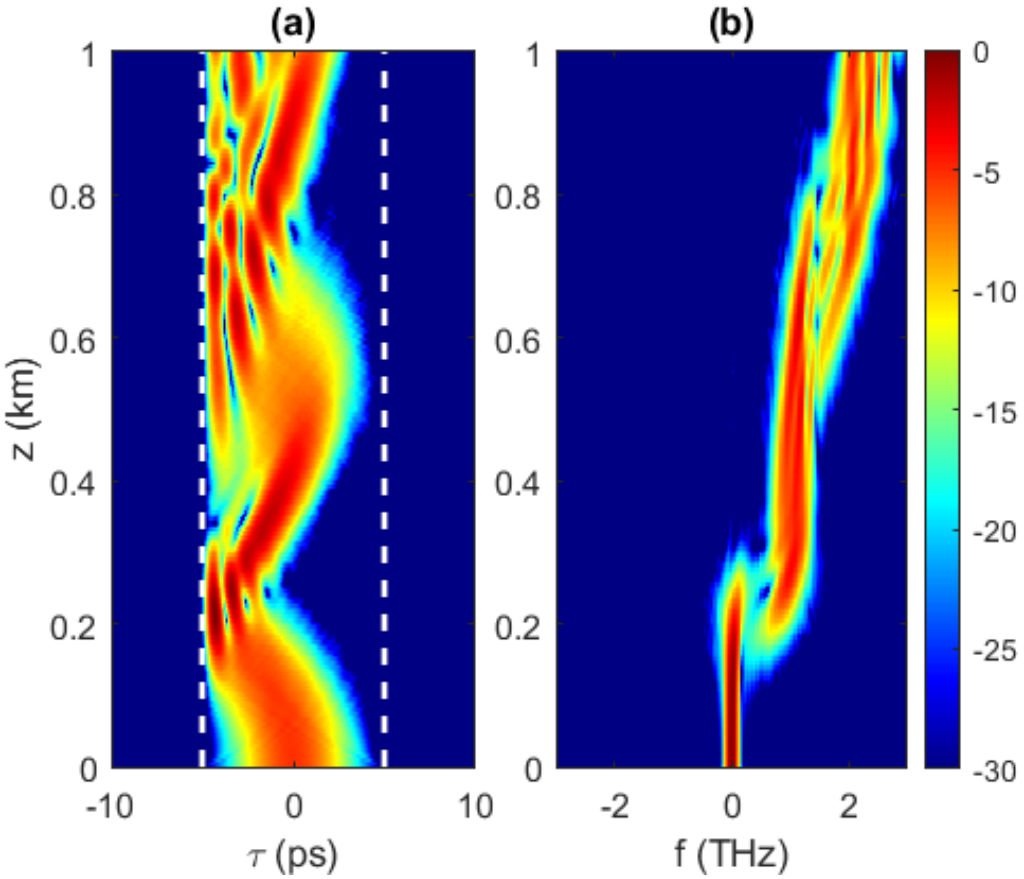

Figure 5.8: (a) Temporal and (b) spectral evolution of a probe pulse ($T_2 = 2$ ps) inside a temporal waveguide with $\Delta T = 10$ ps.

the probe pulse and find the eigenmodes and eigenvalues of the curved waveguide in this frame. We use these modes to develop a set of coupled-mode equations, showing that shape changes occur because of mode coupling induced by the Raman-induced deceleration of pump solitons used to make the waveguide. A simplified two-mode model is used to introduce a single parameter governing modal coupling and to find the condition under which coupling becomes weak enough that the probe pulse blue-shifts its spectrum without changes in its pulse shape.

From a practical standpoint, our study shows that the effects of stimulated Raman scattering must be considered when two femtosecond pump pulses with a fixed separation are employed to form a temporal waveguide that traps a probe pulse between the two pump pulses. The spectral blue shift of the probe pulse in such a waveguide can be useful for applications that require a tunable source of short pulses. It is difficult to change the wavelength of low-energy pulses. The technique used in this work transfers the Raman-induced red shift of pump pulses to probe pulses through cross-phase modulation as a blue shift, whose magnitude can be controlled by adjusting the width and spacing of pump pulses used to form the waveguide.

Chapter 6

Experiments on Temporal Waveguides

Starting from this chapter, we discuss the experimental work on temporal reflection. In this chapter, we study the temporal waveguide that is closely related to the discussion in Chapter 5.

In Chapter 5, we considered a temporal waveguide formed by two Raman solitons. In some situations, such as the result shown in Fig. 5.8, essentially only a single soliton is interacting with the probe pulse that is trapped by it. This observation suggests that a single Raman soliton is enough to create a temporal waveguide for the probe pulse.

In this chapter, we demonstrate the formation of such a temporal waveguide in a photonic crystal fiber (PCF) used as a nonlinear dispersive medium. By launching the pump and probe pulses at wavelengths on opposite sides of the PCF's zero-dispersion wavelength, we show that the probe pulse is forced to move at the speed of the pump pulse, whose speed keeps decreasing because of a continuous red-shift of its spectrum produced by the process of intrapulse Raman scattering [28]. A consequence of this speed matching is that the probe pulse undergoes a spectral blue shift all along the fiber, becoming as large as 70 nm at the end of the PCF in our experiment. As the amount of blue shift depends on the fiber's length and on the pump pulse's energy, this technique can be useful for tunable wavelength conversion of weak probe pulses, with potential applications in optical signal processing and quantum optics [89, 90].

6.1 Numerical Simulations

Here, we present some numerical simulations. As before, we used the following generalized nonlinear Schrödinger's equation for numerical simulations:

$$\frac{\partial A}{\partial z} + \sum_{k\geq 2} \frac{i^{k-1}}{k!}\beta_k \frac{\partial^k A}{\partial \tau^k} = i\gamma\Big(1 + \frac{i}{\omega_0}\frac{\partial}{\partial \tau}\Big) \times \Big(A(z,\tau)\int_0^\infty R(\tau')|A(z,\tau-\tau')|^2 d\tau'\Big). \tag{6.1}$$

This equation has the same form as in Eq. (4.4), but terms have been added to include higher order dispersion and self steepening [28].

The fiber dispersion parameters are obtained by measuring the wavelength dependence of the group index of the PCF that we used for our experiment. This fiber is a piece of photonic crystal

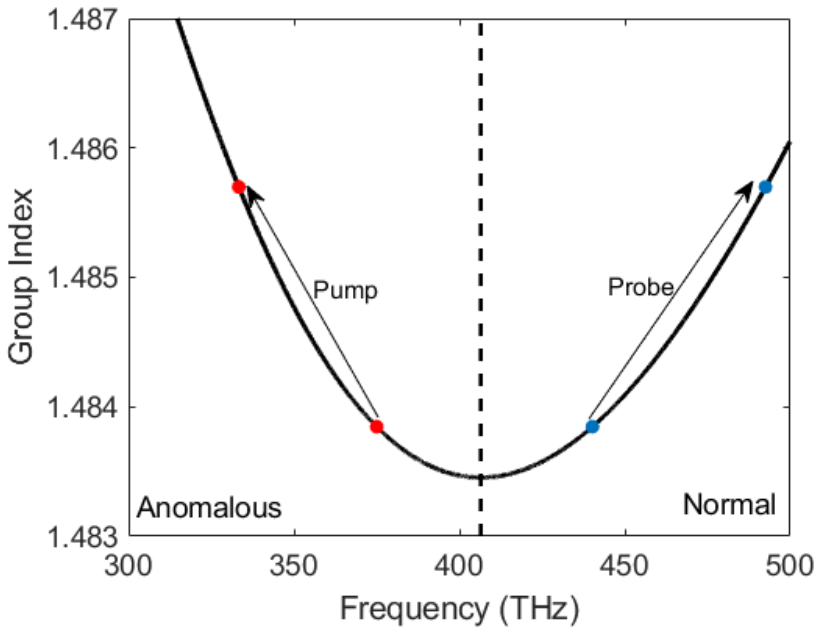

Figure 6.1: Measured group index of our PCF plotted as a function of frequency. The dashed vertical line marks its zero-dispersion frequency (wavelength 738 nm). Two dots at the bottom mark the initial central frequencies of the pump and probe pulses. Two arrows show changes in these frequencies during their propagation inside the PCF.

fiber (PCF) from purchased from IXblue (Part number IXF-SUP-2-135). We used the white light interferometry technique for this measurement [91, 92]. The details of the dispersion measurement are provided in Appendix B. Fig. 6.1 shows the dispersion profile by plotting measured values of its group index as a function of frequency. The dispersion parameters are obtained by performing a polynomial fit of $\beta_1 = n_g/c$, with n_g being the group index of the fiber mode and c being the speed of light in vacuum. The nonlinear coefficient $\gamma = 105$ W^{-1}km^{-1} is given by the fiber's manufacturer. The reference frequency ω_0 corresponds to the wavelength of 800nm used for our input pump pulse. This wavelength is in the anomalous dispersion region of the PCF, allowing the pump to form a soliton.

Similar to the discussion in Chapter 4, the probe pulse wavelength is chosen so that it lies in the normal dispersion region and has a group velocity close to that of the input pump pulse. We used 683ñm in our case (also see Fig. 6.1).

Fig. 6.2 shows the results of numerical simulations based on Eq. (6.1) with the parameters appropriate for our experiment. The pump pulse at 800 nm is launched into the 3.75-m-long PCF and its full width at half maximum (FWHM) is about 110 fs. It forms a higher-order soliton (estimated soliton order 4.6). The probe pulse at 683 nm has a Gaussian shape with a FWHM of 137 fs (bandwidth 5 nm) and its group velocity is nearly matched to that of the pump pulse. The energy of the probe pulse was about 10% of the pump pulse. The low probe pulse energy ensures that the probe has negligible impact on the pump. Dispersion parameters were obtained by fitting a polynomial to the measured dispersion data in Fig. 6.1.

As seen in Fig. 6.2, the higher-order soliton undergoes the process of soliton fission within

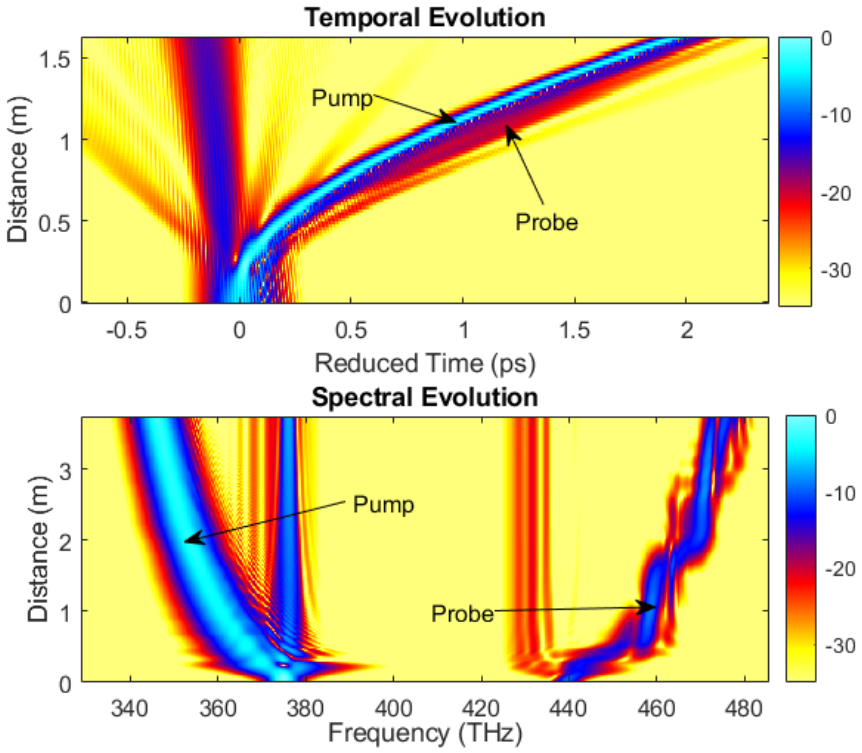

Figure 6.2: Numerical simulations for a Raman-induced temporal waveguide. The probe pulse follows the pump's trajectory because of its Raman-induced deceleration. Spectral evolution at the bottom shows the red and blue shifts of the pump and probe pulses.

the first 20 cm of the PCF [28]. A short fundamental soliton is formed after the fission, which experiences intrapulse Raman scattering and deceleration, leading to a bent trajectory in the time domain. The probe pulse follows this trajectory through temporal reflections while changing its frequency in a zigzag fashion. The net result is that a Raman-induced temporal waveguide is formed that guides the probe pulse along the pump's trajectory. As the pump's spectrum red-shifts, the spectrum of the probe pulse shifts toward the blue side because the two pulses experience opposite kinds of dispersion. The final frequencies of the pump and probe at the end of the PCF are shown by two arrows in Fig. 6.1.

One can view the Raman-induced waveguiding process as a cascade of temporal reflections along the fiber's length. As the pump pulse slows down near the front end of the fiber, the probe reflects off the pump for the first time and blue-shifts its frequency to move slower than the pump pulse. However, after this first reflection, the pump pulse keeps slowing down and a second reflection occurs that shifts the probe's frequency further to the blue side. This process keeps repeating along the fiber's length. The net result is that a cascade of temporal reflections keeps the pump and probe pulses moving together along the entire length of the fiber. This interpretation is justified by the zigzag pattern of the blue shifts of the probe seen in Fig. 6.2, which is very different from the smooth spectral red shift of the pump. The total blue shift at the output end is such that the group velocities of the probe and pump pulses are nearly the same. In addition to the blue shifted probe pulse, we still see some remaining unconverted probe. This is expected because a small portion of

probe can still tunnel through the pump pulse since it has a finite temporal width. This tunneling can be understood from the analogy between the 1-dimensional quantum scattering problem (See Sec. 3.2). The pump pulse forms a potential barrier that is experienced by the probe pulse. Since this barrier has a finite width, some tunneling should be expected.

6.2 Experimental Setup and Results

Fig. 6.3 shows the experimental setup schematically. A Ti:sapphire laser-pumped regenerative amplifier (Coherent, Astrella) emits a 1-kHz train of 100-fs pulses at 800 nm. Half of each pulse's energy pumps an optical parametric amplifier (OPA). The OPA generates white light from a small portion of the pump as seed and amplifies this seed through nonlinear wave mixing. Its output wavelengths are tunable over a wide range. A bandpass filter is used to reduce the spectral bandwidth to about 5 nm. We selected 683-nm probe pulses from the OPA and combined them using a beam splitter with the 800-nm pump pulses that were delayed suitably using a translation stage. The resulting beam is focused onto the 3.75 m-long PCF, and the spectrum of its output is measured with a spectrometer (Ocean Optics, USB2000+). A flip mirror sends the two beams to a BBO crystal for sum-frequency generation (SFG). The output is passed through a short-pass filter and sent into a spectrometer for UV detection. The SFG signal is used to synchronize the pump and probe pulses. The linear polarizer before the PCF ensures that the two pulses have the polarization direction that is aligned with one of the principal axes of the PCF. A half-wave plate is used in the pump beam's path to change the peak power of pump pulses.

Figure 6.4 shows the measured spectra from the PCF's output in three situations. When only the pump pulse with energy of about 18pJ is launched, the spectrum in part (a) contains two dominant peaks centered at 800 nm and 866 nm. The second peak corresponds to a fundamental soliton, formed after the fission of the pump pulse at a short distance into the PCF. Intrapulse Raman scattering has the most impact on this soliton, and its spectrum red-shifts all along the PCF. The remaining energy of the pump pulse appears as a peak around 800 nm. Experimentally, the main output soliton has an energy of about 12.3pJ while the simulation would predict an output Raman

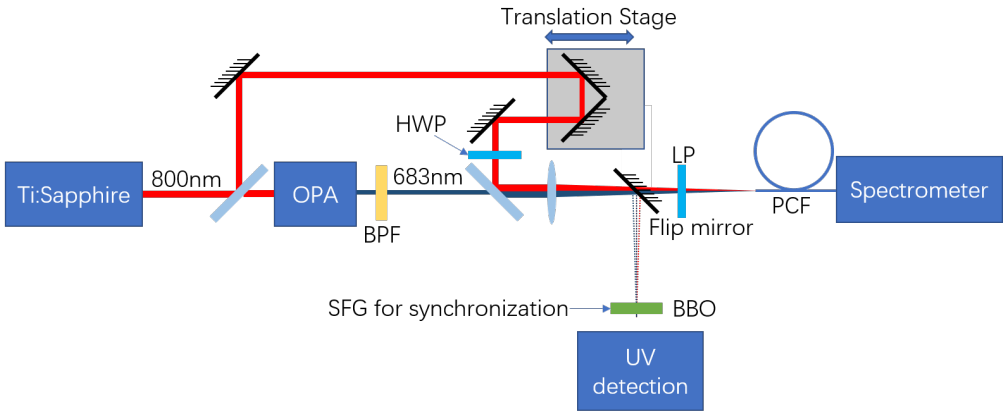

Figure 6.3: Experimental setup. OPA: Optical parametric amplifier. BPF: bandpass filter. HWP: half-wave plate. LP: linear polarizer. PCF: photonic crystal fiber. SFG: sum frequency generation.

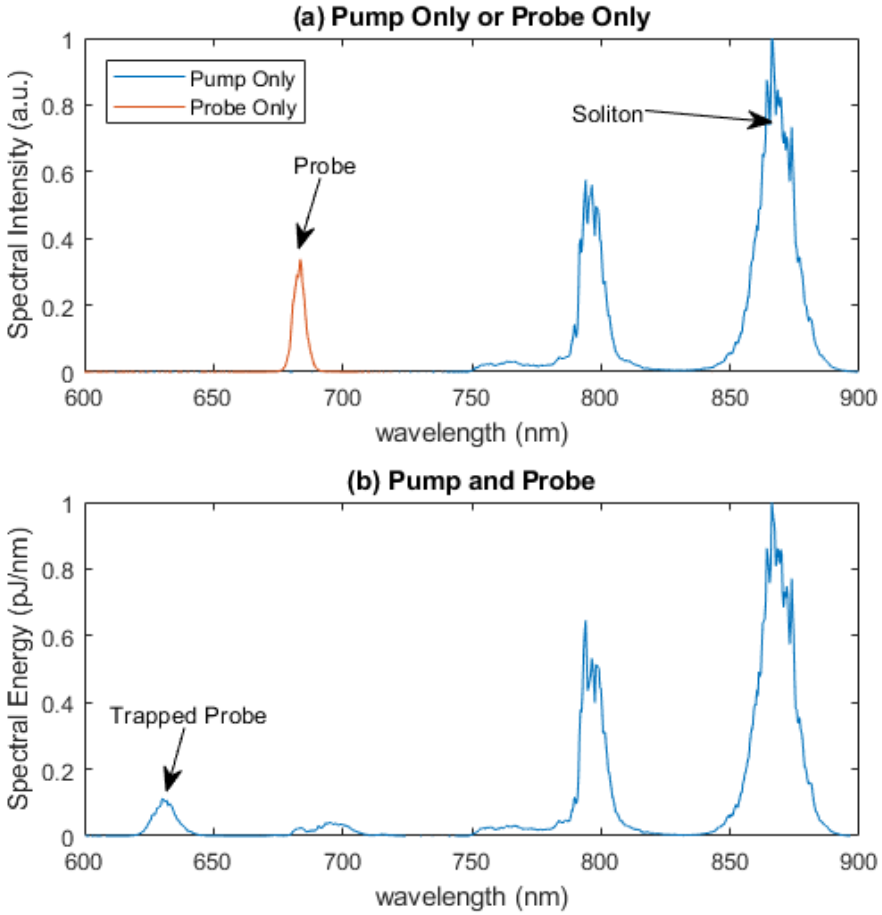

Figure 6.4: Measured output spectra under different conditions. (a) Only the pump or probe pulse is sent through the PCF. (b) Both pump and probe pulses are sent through the PCF. Data are averaged over 25000 pulses.

soliton (with the same amount of Raman shift) with energy of 15pJ. The agreement is reasonable and the discrepancy probably comes from the uncertainty in the simulation's parameter as well as some possible losses in the experiments. Experimentally, we did not accurately measure the pulse energy for every case. Instead, it is more reliable to keep track of the Raman red shift of the main soliton. The reason is that the soliton's Raman red shift (with a given length), which can be more easily measured accurately, is determined by the soliton's energy, and therefore determines the trajectory and evolution of the soliton. This determines the interaction of the probe pulse with this soliton.

When only probe pulses are launched at 683 nm, a single peak at this wavelength is observed. When both the pump and probe pulses are launched together into the PCF, as seen in Fig. 6.4(b), the output spectrum has a new blue-shifted peak at 631 nm. As expected, two peaks on the right side, formed through fission of the pump pulse, are not affected much by the probe pulse. In contrast, considerable energy of the probe pulse is blue-shifted to near 631 nm. It can be seen from Fig. 1, that the group velocity at this wavelength matches with that of the red-shifted soliton

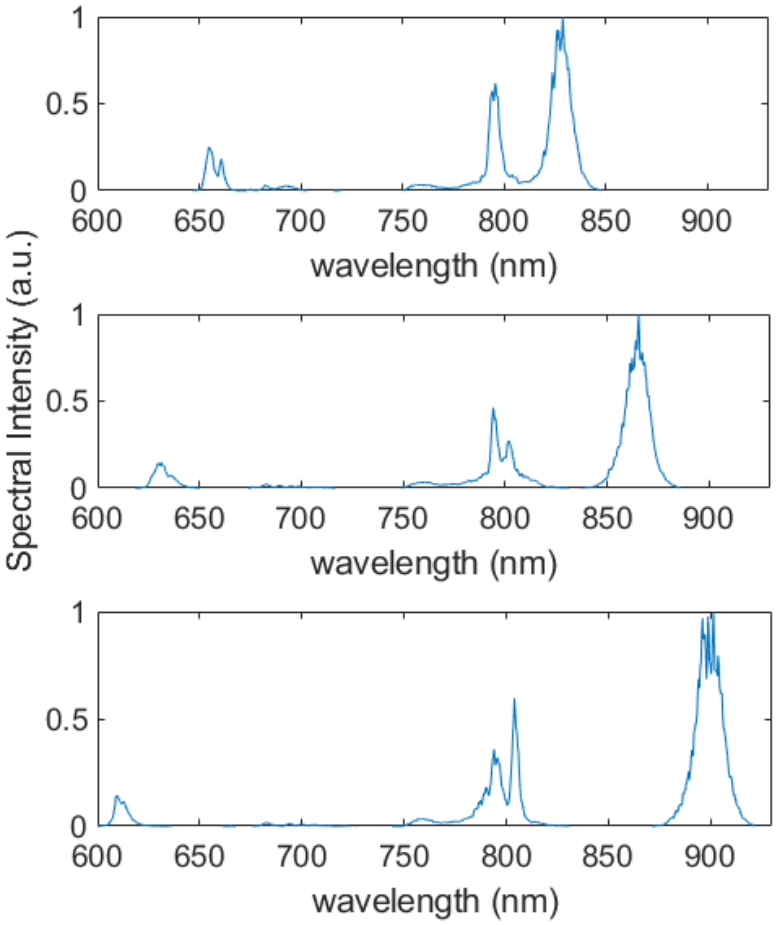

Figure 6.5: Measured output spectra for three values of average pump pulse energy. Data are averaged over 2500 pulses.

at 866 nm. This matching indicates that a Raman-induced temporal waveguide is indeed formed inside our PCF.

The final wavelength of the probe pulse at the PCF's output depends on the peak power of the soliton formed after the fission of pump pulses. We have verified this feature by varying the average pump power launched into the PCF. Figure 6.5 shows the measured spectra at three power levels. As we increase the pump power, the soliton's red shift becomes larger. As a result, the blue shift of probe pulses also becomes larger because of their Raman-induced temporal waveguiding.

The magnitude of the blue shift is set by the condition that the pump and probe pulses travel at the same speed inside the PCF. To verify this feature, we plot In Fig. 6.6 the measured blue-shifted wavelength as a function of the output wavelength of the soliton (circles). The soliton's wavelength is determined by fitting the spectrum to that of a "sech" pulse, while the probe's wavelength is based on the center-of-mass estimate. The solid line is obtained from the dispersion data shown in Fig. 1. It is evident that the probe's blue-shifted wavelength agrees quite well with the prediction based on group-velocity matching. The excellent agreement seen in Fig. 6.6 is an indirect proof that a Raman-induced temporal waveguide did indeed form in our experiments.

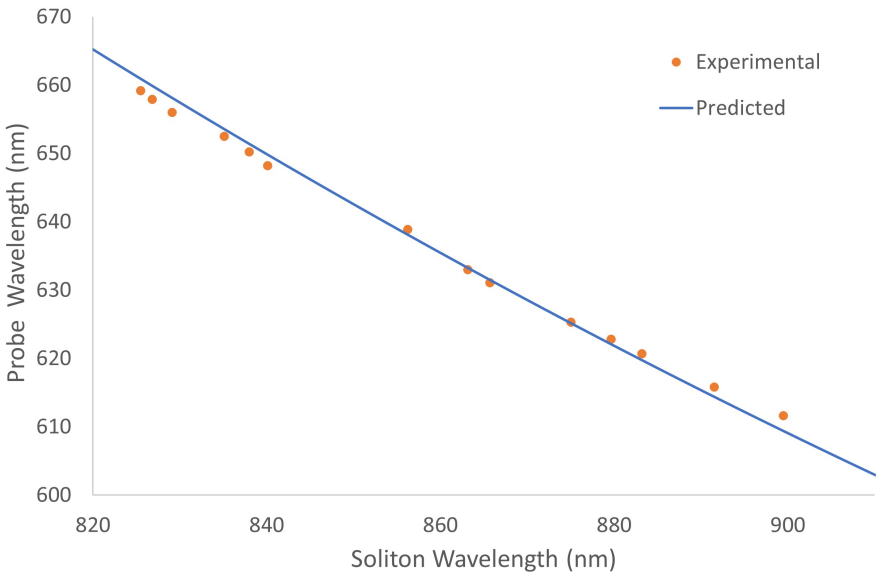

Figure 6.6: Probe's output wavelength plotted as a function of soliton's wavelength (circles). The solid line is the prediction based on the dispersion data in Fig. 1.

6.3 Conclusion

In this chapter, the formation of a Raman-induced temporal waveguide is demonstrated by launching short pump and probe pulses inside a photonic crystal fiber at wavelengths that lie on the opposite sides of the zero-dispersion wavelength of the fiber. Under such conditions, the pump pulse creates a fundamental soliton whose speed changes continuously owing to its deceleration through the Raman-induced red shift of its spectrum. We show that the spectrum of the probe pulse is blue-shifted in a zigzag fashion along the fiber to ensure that the two pulses keep moving at nearly the same speeds over the entire length of the fiber. The output wavelengths of the pump and probe pulses depend on the peak power of input pump pulses and their measured values agree with the predictions based on the measured dispersion data. Numerical modeling also shows good agreement with the experimental results.

We explain the Raman-induced waveguiding process as a cascade of temporal reflections along the fiber's length that keeps the pump and probe pulses moving together along the entire length of the fiber. This interpretation is justified by the zigzag pattern of the blue shifts of the probe seen in Figure 6.2. The blue shift of probe pulses may be useful for tuning the wavelength of low-energy optical pulses toward the blue side using a suitable pump laser. Although four-wave mixing can also be used for this purpose, its use requires phase matching. In contrast, our scheme makes use of intrapulse Raman scattering of pump pulses, which does not require phase matching. It is the formation of a temporal waveguide that transfers the pump's Raman-induced red-shift to the probe pulses as a blue shift. Our experiment shows that this shift can approach 100 nm in the visible region.

Chapter 7

Probing the Boundary's Trajectory

In the previous chapter, we studied the interaction of a probe pulse with a decelerating boundary, when the incident probe pulse lags the boundary initially. As a result, the probe pulse is reflected from the boundary in a cascaded fashion as the boundary slows down, leading to the trapping of the probe pulse.

In this chapter, we study the case where the incident probe pulse leads the boundary, but travels slower than the initial speed of the boundary. Fig. 7.1 illustrates the interaction using three pulses with different initial delays. In this case, only a single temporal reflection can take place. Because the boundary's speed is changing as it propagates, the boundary's velocity at the interaction point depends on the incident pulse's timing. From the phase continuity discussed in Chapter 2 (Eq. (2.9)), the reflected pulse frequency depends on the boundary's velocity. Thus, central frequency of the reflected light depends on the relative delay between the incident pulse and the boundary. By varying this relative delay, and measuring the reflected pulse's spectrum as a function of the delay, we obtain information about the trajectory of the boundary and use it to deduce the trajectory of the decelerating pump pulse. Effectively, we can use the temporal reflection to probe the trajectory of a boundary that changes its speed inside the PCF.

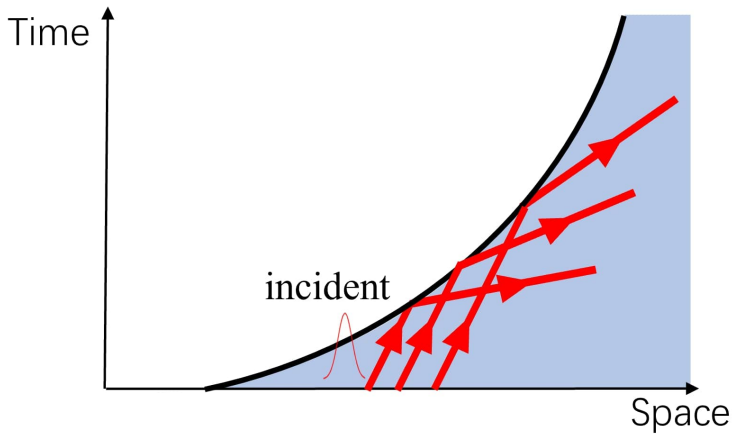

Figure 7.1: Schematic showing the temporal reflection of three probe pulses (red lines with arrows) from a decelerating boundary. Central frequency of the reflected pulse depends on the initial delay (or advance) of the probe pulse.

We used the Raman soliton (pump) in a photonic crystal fiber to form the boundary (boundary is the same as in the previous chapter), and sent a weaker probe pulse to reflect from it with different pump-probe delays and measured the reflected pulse spectrum with different delays. We will show later, both numerically and experimentally, that the reflected pulse's spectrum changes significantly as the initial delay between the pump and probe pulses is varied. And we show that it is possible to deduce this trajectory from the delay-dependent spectral data. It should be stressed that the trajectory of a Raman soliton is hard to measure without destroying the fiber. Our approach provides a non-destructive method for deducing the soliton's trajectory. We believe that it can be used as a diagnostic tool for many other optical processes.

7.1 Numerical Simulations

For numerical simulations, we first write the total electric field by introducing the pump and probe pulse envelopes:

$$E(z,t) = \mathrm{Re}\Big(A_s(z,t)e^{i[\beta(\omega_s)z-\omega_s t]} + A_p(z,t)e^{i[\beta(\omega_p)z-\omega_p t]}\Big), \tag{7.1}$$

where t is the time in the laboratory frame, A_s and A_p are the envelopes of the soliton (pump) and probe pulse respectively, and $\beta(\omega)$ is the frequency-dependent propagation constant. ω_s and ω_p are reference frequencies that should be close to the central frequencies of the pump and probe. We can derive a set of two coupled propagation equations for A_s and A_p in a similar way as we did in chapter 4. Basically we first combine the two envelopes into a single envelope function, which satisfies the propagation equation Eq. (2.28) with the nonlinear terms given by Eq. (2.25). Then we assume that the two pulses are spectrally separated far from each other and separate the two envelopes based on this assumption. Assuming that the probe energy is small enough that its nonlinear effects can be neglected, we arrive at the following coupled NLS equations [28]:

$$\frac{\partial A_s}{\partial z} + \sum_{k\geq 2} \frac{i^{k-1}}{k!}\beta_k^{(s)} \frac{\partial^k A_s}{\partial \tau^k} = i\gamma\Big(1+\frac{i}{\omega_0}\frac{\partial}{\partial \tau}\Big)\Big((1-f_R)|A_s|^2A_s + f_R N_R A_s\Big), \tag{7.2}$$

$$\frac{\partial A_p}{\partial z} + \Delta\beta_1 \frac{\partial A_p}{\partial \tau} + \sum_{k\geq 2} \frac{i^{k-1}}{k!}\beta_k^{(p)} \frac{\partial^k A_p}{\partial \tau^k} = 2i\gamma|A_s|^2A_p, \tag{7.3}$$

where $\tau = t - z/v_g(\omega_s)$ is the reduced time in a frame moving with the speed $v_g(\omega_s)$ and $\beta_k^{(j)} = (d^k\beta/d\omega^k)|_{\omega_j}$ with $j = s, p$ are the dispersion parameters of the PCF at the soliton and probe's reference frequencies respectively. The parameter, $\Delta\beta_1 = 1/v_g(\omega_p) - 1/v_g(\omega_s)$, is a measure of the speed difference between the probe and the soliton. As losses are < 0.36 dB for our 3.8-m-long fiber (as per fiber's manufacturer), we have neglected the loss term in Eqs. (7.2) and (7.3). The Raman term is contained in $N_R = \int_0^\infty h_R(\tau')|A_s(z,\tau-\tau')|^2 d\tau'$. The equations are essentially the same as in Chapter 4, except that we included higher order dispersions for both pump and probe pulses, and the self-steepening term for the pump pulse. We simplified the interaction between the pump and probe pulses by only considering the pump pulse's induced cross-phase modulation to

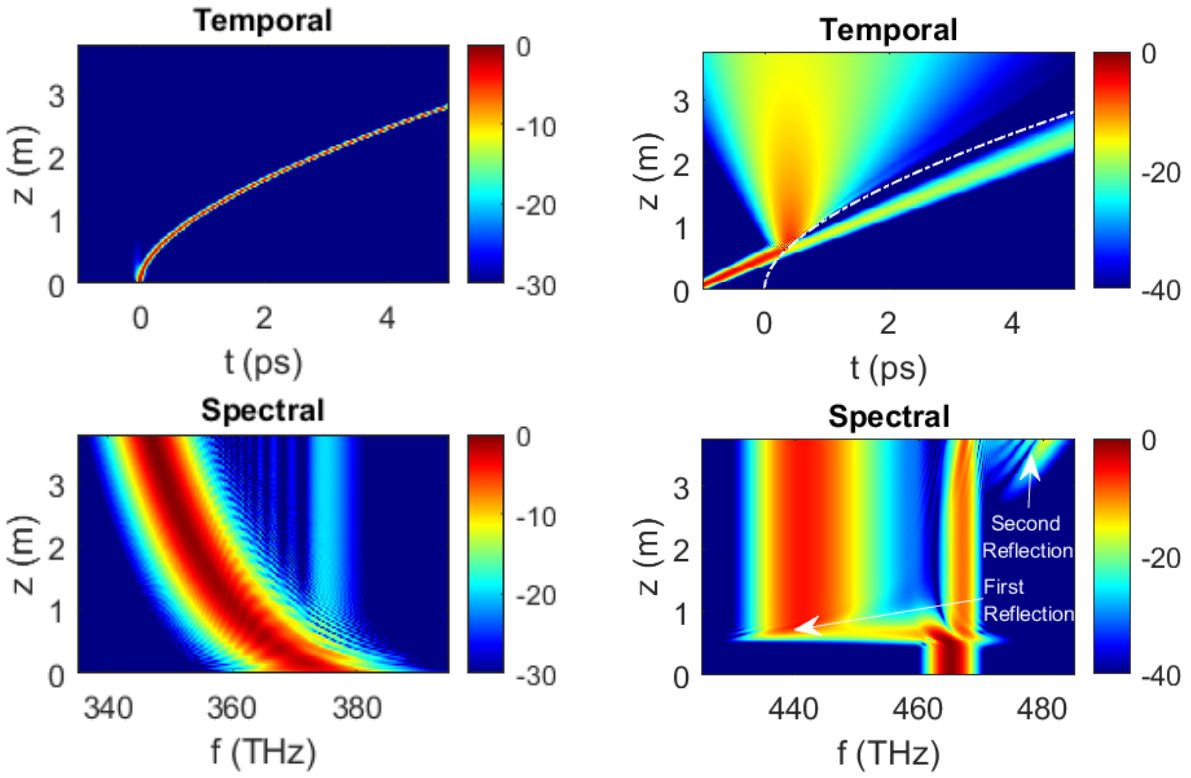

(a) Soliton

(b) Probe pulse

Figure 7.2: Temporal and spectral evolution patterns over the PCF length are shown for the (a) soliton (pump) and (b) probe pulse on a logarithmic color scale. The white dashed line in (b) shows the trajectory of the soliton.

the probe pulse. The dispersion parameters are still extracted from the dispersion curve of the PCF that we purchased (See Fig. 6.1).

We solved Eqs. (7.2) and (7.3) with the Runge–Kutta method using $A_s(0,\tau) = \sqrt{P_1}\,\mathrm{sech}(\tau/T_1)$ for the pump pulse with $T_1 = 15.7$ fs and $P_1 = |\beta_2^{(s)}|/(\gamma T_1^2)$ for the peak power of a fundamental soliton. The probe pulse was a much wider Gaussian pulse centered at 645 nm with a spectral width of 4 nm. The soliton had an initial delay of 1.15 ps relative to the probe pulse. The nonlinear coefficient for our PCF is estimated to be 105 $\mathrm{W}^{-1}\mathrm{km}^{-1}$. In our experiments, we inject pump pulses with energy higher than that needed to form a fundamental soliton. After the fission process, a shorter Raman soliton is formed, whose spectrum shifts toward the red side with propagation inside the fiber. For our numerical simulations, we use a short fundamental soliton to study the probe's reflection from this Raman soliton. This is justified because in our experiment described in the following section, we focus on the interaction of the probe pulse with the Raman soliton after it is clearly formed.

Figure 7.2 shows our numerical results for the preceding parameter values. Temporal and spectral evolution patterns over the PCF length are shown for the (a) soliton (pump) and (b) probe pulse using a logarithmic color scale. As before, we get a soliton with a decelerating trajectory from the Raman red shift. We will denote this phenomenon as Raman-induced frequency shift

(RIFS).

The probe pulse is initially traveling slower than the soliton. When the soliton collides with it, most of its energy gets reflected by the soliton. This is clearly seen from the probe's temporal evolution in Fig. 7.2a. The reflected pulse travels faster than the soliton in the normal-dispersion region of the PCF because of a red shift in its spectrum. We can clearly identify this red-shifted peak in the spectral evolution of the probe (white arrow marked "first reflection"). However, a fraction of the probe's energy is transmitted through the soliton, and this part keeps traveling slower than the soliton. As the soliton keeps decelerating inside the PCF, the transmitted part of the probe collides again with it, and a second reflected pulse is produced. This collision generates blue-shifted radiation near the end of the fiber (marked by the arrow "second reflection" in the probe spectrum).

As discussed earlier, a change in the initial delay of the soliton from the probe pulse should change the spectrum of reflected pulse significantly. This is confirmed by performing simulations with different delays. The output spectra of the probe pulse with different delays are shown in Fig. 7.3. As the delay becomes larger, the probe's blue shift becomes smaller and eventually disappears. This can be understood from Fig. 7.1. As delay increases, the speed difference between the probe and soliton decreases after they collide. When the delay is large enough, the soliton does not catch up with the probe, and temporal reflection ceases to occur. The dashed black line in Fig. 7.3 is calculated by considering the intersection of the probe's center with the soliton's decelerating trajectory. Frequency of the reflected pulse is calculated from Eq. (2.9) using v_b as the instantaneous speed of the soliton at that location (see supplemental for details). We find an excellent agreement between the simulated output spectrum and the analytical prediction of the central wavelength.

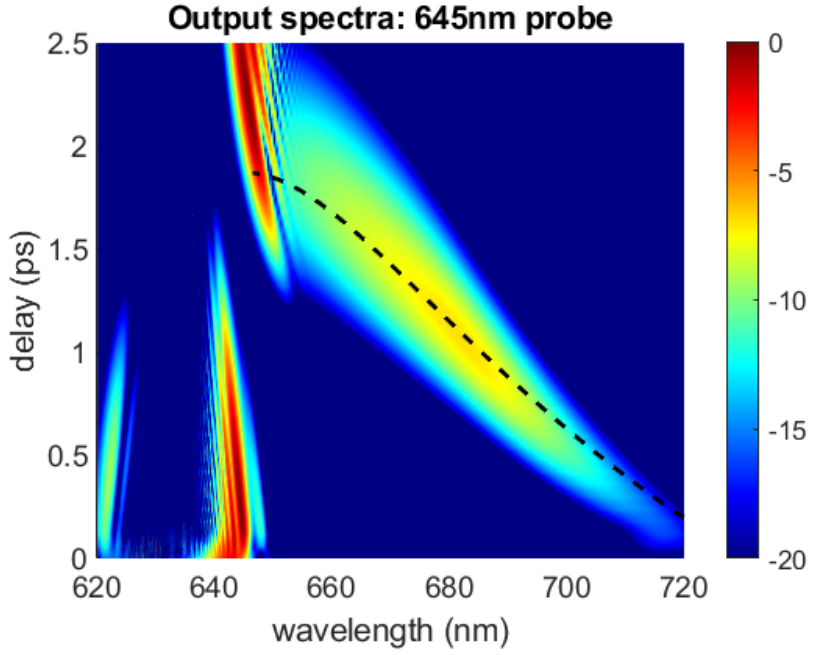

Figure 7.3: Color-coded output spectrum of a 645-nm probe pulse for different initial delays between the pump and probe pulses.

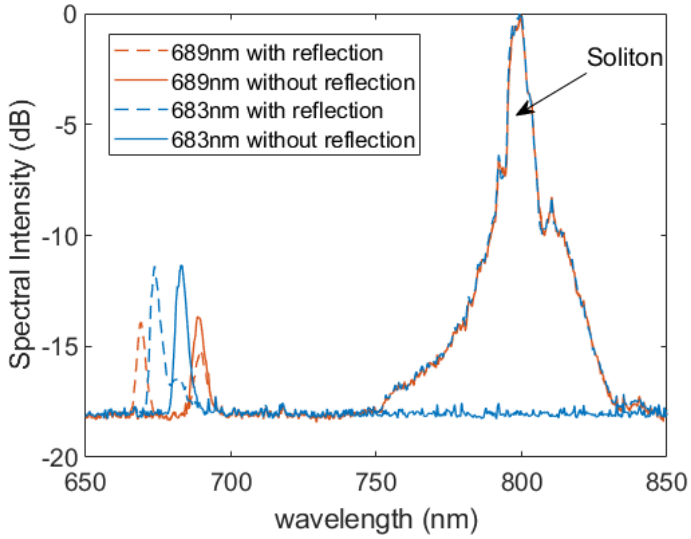

Figure 7.4: Measured output spectra with three distinct peaks when the soliton undergoes negligible RIFS. Probe pulses at wavelengths 683 and 689 nm were reflected off the soliton formed by the 800-nm pump pulse. A blue-shifted reflected pulse (dashed line) is produced in both cases.

Since the reflected pulse's spectrum depends on the speed of the soliton at the time of collision, we can deduce this speed by measuring the spectrum, which allows us to calculate the soliton's frequency. As we change the initial delay between the soliton and the probe, the probe pulse hits different parts of the trajectory of the soliton. Thus, the delay-dependent spectra shown in Fig. 7.3 contain information about the soliton's trajectory, making it possible to deduce the soliton's trajectory from the spectral data.

The soliton's spectrum shifts from 800 nm to 864 nm over the PCF length in Fig. 7.2a. In this case, it is not possible to probe the whole trajectory using probe pulses at a single wavelength. The reason is that the efficiency of temporal reflection depends critically on the speed difference between the probe and the soliton. As a result, probe pulses at one wavelength can only probe the portion of the soliton's trajectory where the speed difference is sufficiently small. To probe the whole trajectory, we send probe pulses at several different wavelengths. Combining the spectral data measured for different probe wavelengths, it became possible to probe the whole trajectory of the soliton.

7.2 Experimental Probing of the Raman Soliton's Trajectory

The experimental setup is the same as described in chapter 6, Fig. 6.3. The only difference here is that we now changed the band pass filter in the probe pulse beam path, and the filter is tilted to tune the central wavelength of the probe pulse.

As described in Chapter 6, the pump pulse generates a fundamental soliton, which is responsible for the main interaction between the pump and probe. The soliton's Raman red shift (at the output) depends on the input pulse energy. We first consider the simpler case of temporal reflection

without the Raman effect. This is achieved by carefully adjusting the energy of the pump pulse sent into the fiber. By monitoring the output spectrum, it was possible to control energy such that a soliton is formed with negligible RIFS (at an energy of about 4 pJ). Probe pulses at two different wavelengths (683 and 689 nm) are sent into the fiber, and the relative delay between the soliton and probe is tuned such that the whole probe pulse can reflect off the soliton, resulting in maximum reflectivity. We kept the energy of probe pulses relatively small to ensure that they do not impact pump pulses during propagation. For the results shown in Fig. 7.4, their energy was smaller than 0.1 pJ for both cases. Probe pulses at these two wavelengths travel faster than the soliton. The input and output spectra of probe pulses are shown for comparison. After reflection, a blue shifted peak appears in the spectrum, which belongs to the reflected pulse traveling slower than the soliton. Comparing the probe pulses at the two wavelengths, the 689-nm probe has a larger initial speed difference, which makes the frequency shift of the reflected pulse larger with a smaller reflectivity. Using the incident and reflected probe spectra, we can calculate the soliton's wavelength at the time of collision from the phase-continuity relation in Eq. (2.9). The wavelength calculated this way is 802 nm, and this value is in agreement with the soliton's central wavelength seen in Fig. 7.4, which is 800nm.

For the results shown in Fig. 7.5, the Raman effects were included by increasing the energy of pump pulses launched into the PCF to about 17 pJ, which was large enough to form a higher-order soliton and create a short fundamental soliton through a fission process. The wavelength of this soliton shifts through RIFS toward the red side all along the PCF, resulting in a large shift at the output end. As seen in part (d) of Fig. 7.5, soliton's central wavelength has shifted from 800 to 864 nm over a length of just 3.8 m. Although some energy is left around 800 nm, it does not form another soliton and has a relatively minor impact on the probe pulse. We launched probe pulses at three wavelengths separated by 10 nm (645, 635 and 625 nm) and varied pump-probe delays to probe the soliton's trajectory. Theoretically, it has been shown that soliton's dynamics can be affected by energetic probe pulses [93]. We kept the energy of probe pulses relatively small to ensure that the spectra of pump pulses were not affected by them. This energy in our experiment is estimated to be below 0.5 pJ, respectively. Measured output spectra as a function of pump-probe delay (positive delay means that the pump arrives later than the probe) are shown for three probe wavelengths in parts (a), (b), and (c) of Fig. 7.5.

For probe wavelengths of 645 nm and 635 nm, we see a similar pattern. A red-shifted reflected pulse is formed after a specific delay, the red-shift becomes smaller as delay increases, and eventually becomes negligible when delay becomes relatively large. This trend is in good agreement with the simulations shown in Fig. 7.3. Notice that the maximum delay for which we can observe temporal reflection is different for different probe wavelengths. This is so because different probe wavelengths reflect off different portions of the soliton's trajectory.

When the probe's wavelength is 625 nm, the behavior is somewhat different. We still see a red-shifted peak with a decreasing red shift as delay increases. The difference is that this red-shifted peak does not merge with the original probe pulse's spectrum when delay becomes large. To understand this behavior, we note that probe pulses at wavelengths of 645 and 635 nm travel slower than the incident pump pulse, but faster than the output soliton. Thus, by changing the pump-probe delay, it is possible for the reflection to occur where the soliton and probe pulse have the same speed. On the space-time diagram shown in Fig. 7.1, the soliton and probe pulse's trajectory become parallel to each other. In this situation, reflected pulse's spectrum merges into the incident spectrum. In contrast, the 625-nm probe pulse travels slower than the output soliton

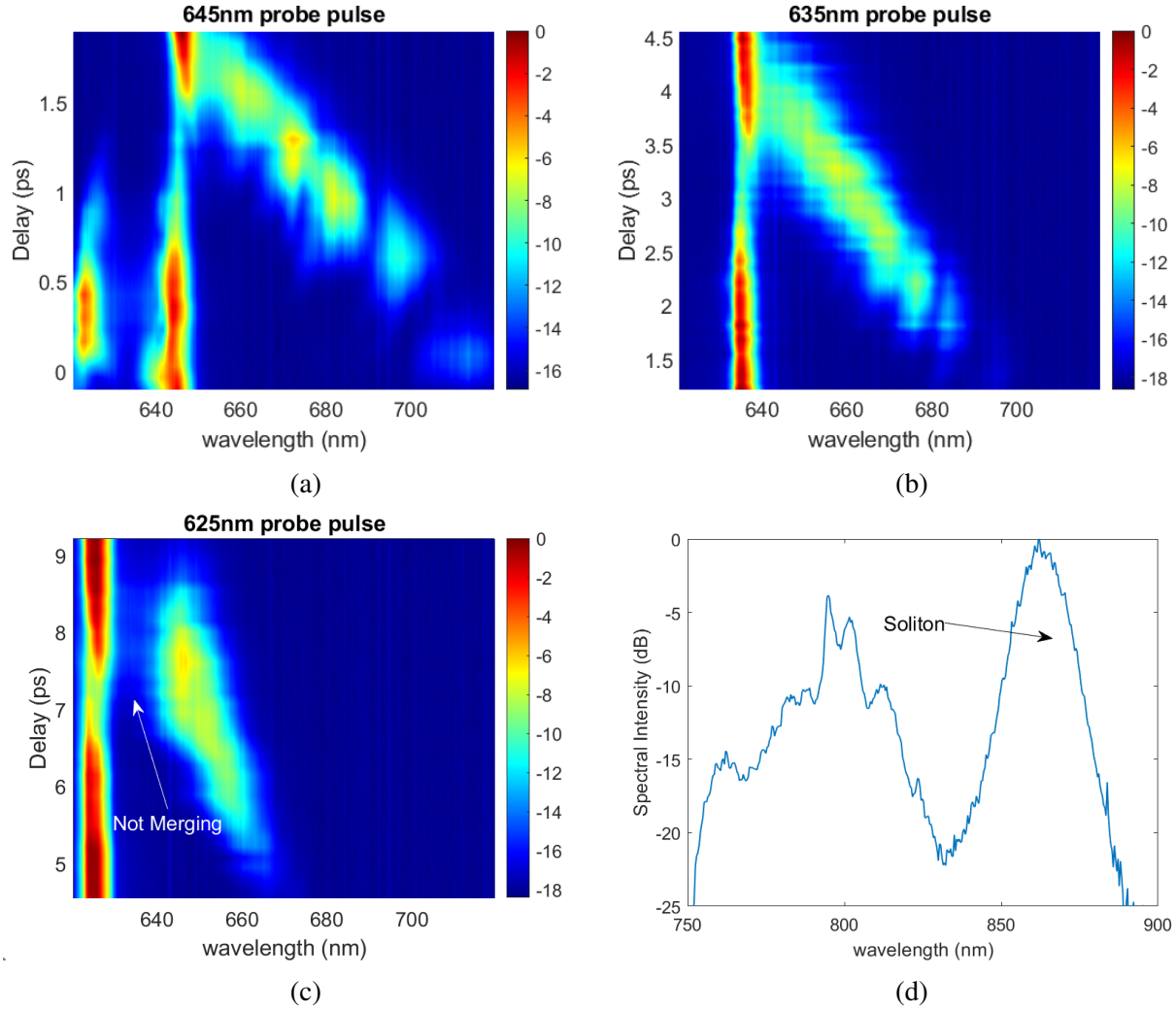

Figure 7.5: Measured output spectra for different pump-probe delays when the incident probe's central wavelength was (a) 645 nm, (b) 635 nm and (c) 625 nm. Spectral intensity is shown in logarithmic scale relative to the probe's peak spectral intensity. (d) Output spectrum in the pump's spectral region.

all along the PCF length. As a result, their trajectories never become parallel. This is the reason why the reflected pulse's spectrum does not merge into the incident spectrum when the probe's wavelength is 625 nm.

As we discussed earlier, the delay-dependent spectra shown in Fig. 7.5 contain information about trajectory of the soliton inside the PCF. Here we briefly describe the approach we used for this purpose and refer to the Appendix for more details. The trajectory we want to extract specifies the soliton's wavelength (or speed) as a function of propagation distance. However, without knowing this trajectory, the location of pump-probe collision can not be determined for a given pump-probe delay. To solve this dilemma, we derive a differential equation, Eq. (S10), in the Appendix using the phase-continuity relation in Eq. (2.9). This equation gave us a reasonable estimate of the trajectory. When we used this estimate in our simulations, we found that the predicted wave-

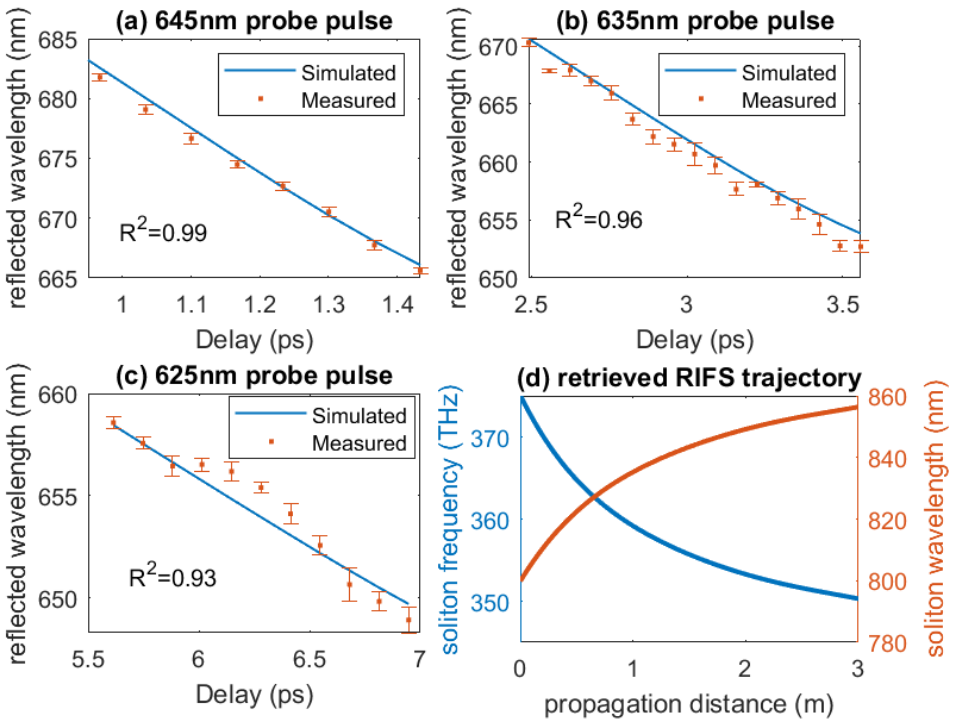

Figure 7.6: (d) Retrieved trajectory of the soliton's wavelength based on the measured delay dependence of the reflected pulse spectra. Numerically predicted wavelength of the reflected pulse wavelength based on the retrieved trajectory for probe pulses launched at wavelengths (a) 645 nm, (b) 635 nm, and (c) 625 nm. Measured results are also shown for comparison.

lengths did not agree well with the measured data. The reason is that the phase-continuity relation assumes reflection to occur at one location, while the probe pulses of finite duration interact with the pump over a range. We adjusted the trajectory estimated from phase-continuity relation with an iterative approach to obtain a better fit between the experimental data and numerical simulations.

The retrieved trajectory of the soliton's central wavelength is shown in part (d) of Fig. 7.6 with a red line; the blue line shows trajectory of the soliton's central frequency. The space-time trajectory can be deduced from the spectral trajectory using the measured dispersion data of the PCF in Fig. 3. We were not able to probe the trajectory over the first 0.5 m of the PCF, where the Raman soliton is produced through the fission process. A parabolic function was used in this region (see supplemental material for details). The shape of the the trajectory depends on the Raman-induced red shift occurring continuously all along the fiber. Interestingly, Fig. 7.6 shows that the rate of RIFS begins to saturate near the PCF's output end. This is because higher-order dispersive effects perturb the Raman soliton and force it to radiate some energy in the form of dispersive waves [28]. This trend can also be seen in the simulations shown in Fig. 7.2a.

To quantify how well the retrieved trajectory matches the actual soliton's trajectory, we performed simulations of the temporal reflection process for the three probe wavelengths (For details, see the supplement). We compare the numerical results with the measured data in parts (a), (b), and (c) of Fig. 7.6. The agreement is quantified by the R^2 values, $R^2 = 1$ indicating a perfect fit. As seen there, the agreement becomes worse for 625-nm probe pulses. The reason can be understood

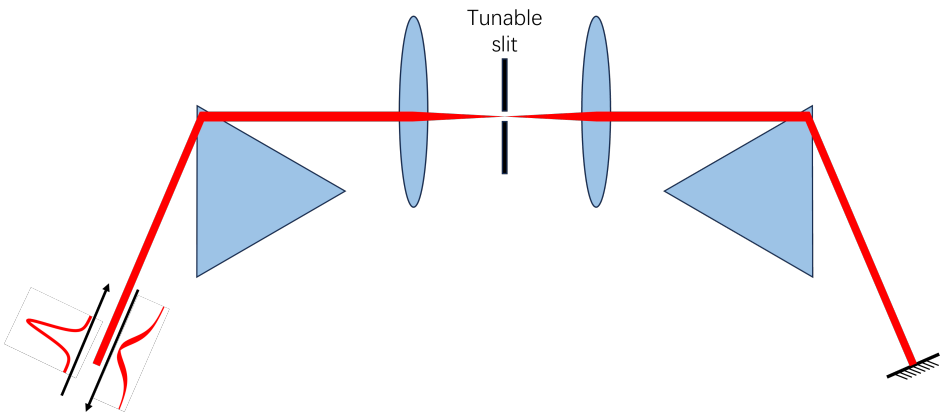

Figure 7.7: 4-f pulse shaper containing two prisms, two lenses, and a mirror. A tunable slit is placed at the Fourier plane of the 4f system for spectral manipulation. One of the prisms is mounted on a translational stage for dispersion control.

from part (c) of Fig. 7.5. As seen there, the red shift is much smaller at this wavelength and varies less rapidly with the delay, both of which make it harder to deduce the center wavelength of the reflected pulse accurately.

7.3 Impact of Pump Pulse Dynamics

The experiment and simulation above focused on the interaction of the probe pulse with a Raman soliton. This Raman soliton is formed through soliton fission, as shown in Fig. 6.2 during the first 0.5 m. After the Raman soliton is formed, it maintains its solitonic shape. When the probe pulse is reflected from the Raman soliton, the reflected pulse's spectrum usually has a clean shape (a single smooth spectral peak as in Fig. 7.3). The experiment described in the previous section focused on the interaction of the probe pulse with the pump pulse after the soliton fission process was complete, and the pump pulse behaved as a fundamental soliton. In this section, we perform some studies on the interaction of the probe pulse with the pump pulse during the initial stage of the pump pulse propagation, where the nonlinear dynamics of the pump pulse affect the temporal reflection.

The easiest way to control the nonlinear dynamics of the pump pulse is to control the input pump pulse shape. When we compare the simulation result from Fig. 6.2 with the one shown in Fig. 7.2a, we can see that the pump pulse in the previous one undergoes a soliton fission process to generate a fundamental soliton, while the latter one directly behaves as a fundamental soliton from the start, while the output Raman shift in the two cases are similar. The reason for this difference comes from the difference in the input pump pulse shape. In the example of Fig. 6.2, the input pump pulse has a sech shape, with FWHM of 110fs and a soliton order of about 4.6. While in the example shown in Fig. 7.2a, the input pump pulse has a sech shape with FWHM of 28 fs, with its power corresponding to a fundamental soliton. These two examples show that the initial stage of pump pulse propagation dynamics is influenced by the input pump pulse shape.

Experimentally, we added a 4-f pulse shaper into the pump pulse beam path to adjust the input

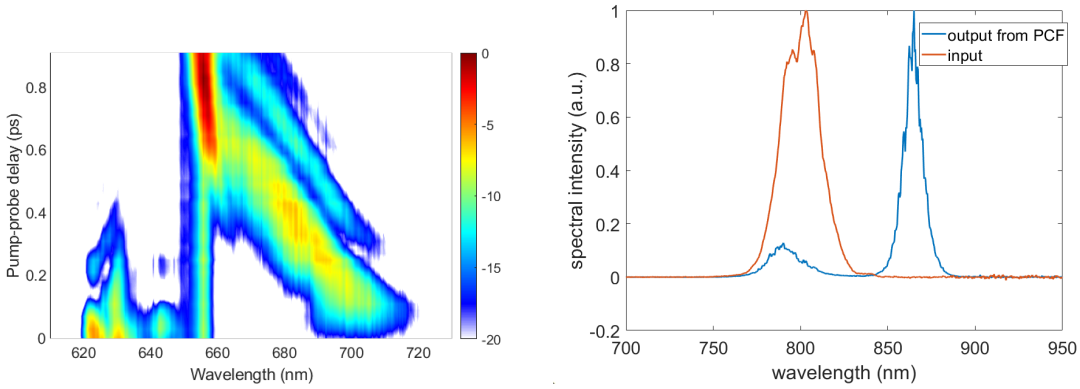

(a) (b)

Figure 7.8: (a) Experimental spectra of the probe pulse at the PCF output obtained for different pump-probe delays. (b) Spectra of the pump pulse at the input and output ends of the PCF.

pump pulse shape. This pulse shaper is shown in Fig. 7.7. It is a double-pass 4f system containing two prisms, two lenses, and a mirror. One prism separates spatially different spectral components of the pulse, and the second prism brings them together after spectral filtering through a tunable slit. A geometrical path difference of different spectral components introduces some dispersion into the system, which can be controlled by translating one of the prism [94]. In this case, we can adjust both the spectral width of the pump pulse as well as the spectral chirp, allowing for the shaping of the input pump pulse.

7.3.1 Pump Pulse as a Fundamental Soliton

First, we conducted experiment when the pump pulse launched into the fiber behaves mostly as a fundamental soliton. To achieve this, the slit in the pulse shaper was made wide enough that the pump's spectrum was not filtered. A prism in the pulse shaper was adjusted to compensate for the material's dispersion. We varied the initial delay of the pump pulse from the probe using the translation stage in Fig. 6.3 and recorded the spectra at the PCF's output end with a spectrometer.

Fig. 7.8b shows the input pump pulse spectrum compared with the output pump pulse spectrum from the PCF. As before, we observed an output Raman peak centered at 865nm. To make the pump pulse behave mostly as a fundamental soliton, we adjusted the pulse shaper to minimize the amount of energy in the original 800-nm region, which depends on the mismatch between the input pulse and the fundamental soliton. In our experiments, the energy of the pump pulse coupled into the PCF is estimated to be about 14.3 pJ, and 82% of this energy is converted into a Raman soliton that evolves as a fundamental soliton (about 12 pJ at the output). The reason that the efficiency of energy converted into the Raman soliton is significantly higher than the result shown in Fig. 7.5d is that in this experiment, we added the pulse shaper to compensate for the dispersion in the beam path, and also at the time of the previous experiment with the results shown in Fig. 7.5d, the laser in our system wasn't operating in the correct condition, leading to a poor pulse shape. We had the laser fixed before we performed the experiment shown in this section.

By sending in a probe pulse centered at 655nm with a spectral FWHM of 5nm, we can reflect

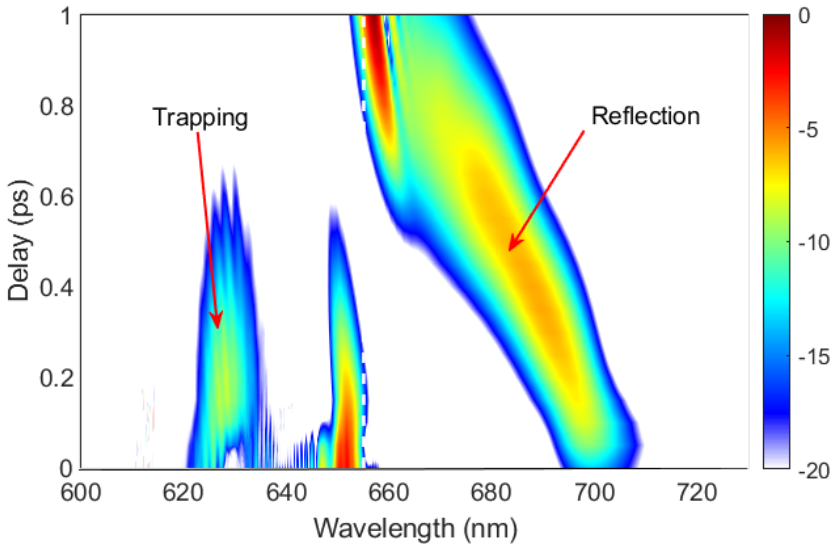

Figure 7.9: Numerical simulations showing how output probe spectrum changes with the initial pump-probe delay. Positive delay implies that the pump is trailing the probe. The White dashed line is the central wavelength of the input probe pulse.

off the pump pulse during the initial stage of propagation (before 0.5m) where the potential soliton fission dynamics may play an important role. Similar to before, we scanned the input pump-probe delay and measured the output spectrum. The result is shown in Fig. 7.8a. As the pump-probe delay increases, the main reflected spectrum shifts to the blue side in a continuous fashion. There is a secondary reflection signal that lies above the main reflected spectrum. Its origin was traced to an unusual shape of the input probe pulse. When using the sum frequency generation of the probe pulse with the pump pulse for synchronization, we found that the main probe pulse has a smaller sub-pulse that trails the main pulse by about 0.2 ps, which agrees with the offset of the two reflection spectra shown in Fig. 7.8a. This sub-pulse also reflects off the pump pulse and creates this secondary reflection peak. As a result, the secondary reflection spectral peak is mostly a replica of the main reflection spectral peak. We will not be focusing on this reflection peak in the remainder of this section.

We also performed a numerical simulation that corresponds to the measurement shown in Fig. 7.8a. We launched a fundamental soliton with 28fs FWHM as the pump pulse, which produced an output Raman shift that matches our experimental observation. Then, the simulated output probe spectrum's dependence on the initial pump-probe delay is shown in Fig. 7.9. We obtained a similar behavior as in the experimental result. The important feature is that as the delay increases, the spectrum of the reflected pulse changes continuously and smoothly, without multiple reflection peak structures. The reason is that an input fundamental soliton does not go through the soliton fission process, and it keeps the fundamental solitonic shape throughout its propagation. For the probe pulse, this soliton forms a "smooth mirror", which results in a "smooth" reflection as shown in Fig. 7.8a and Fig. 7.9.

Next, we focus on the impact of pump-pulse parameters on the temporal reflection of a probe pulse. More specifically, we consider two parameters, namely the width and the chirp of pump pulses, and compare the results with the ideal case of launching a fundamental soliton.

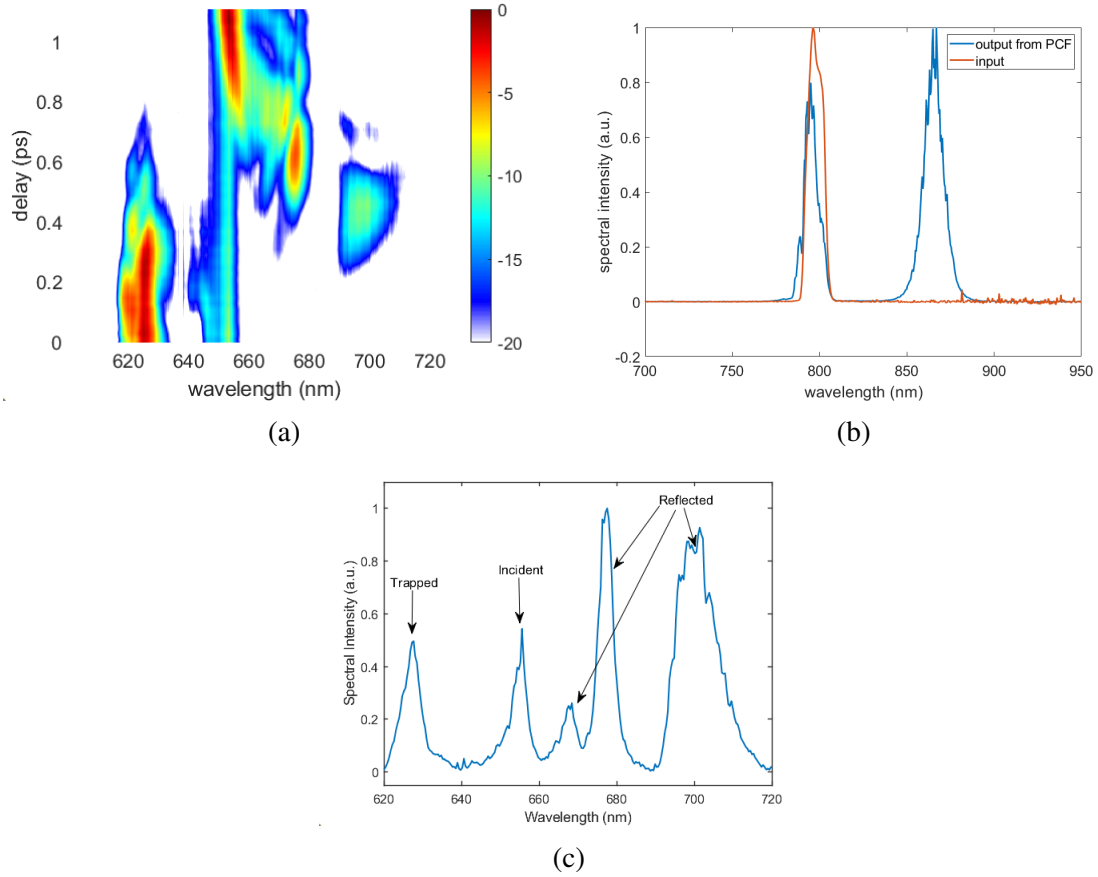

Figure 7.10: Experimental results for wide pump pulses. (a) Spectra of probe pulses at the PCF output as the relative delay is varied. (b) Spectra of probe pulses at the input and output ends of the fiber. (c) Output spectrum obtained for a pump-probe delay of 0.5 ps. Three of the five peaks correspond to three reflected pulses.

7.3.2 Effect of Wider Pump Pulses

We make the pump pulse wider by cutting down its spectral width by controlling the slit width inside the pulse shaper (see Fig. 7.7). The width of pump pulses was close to 162 fs when we reduced the spectral bandwidth to 11 nm. We used the frequency-resolved optical gating (FROG) technique to measure the width of input pump pulses. We also adjusted pulse's energy such that we obtain the same amount of Raman-induced red shift at the PCF's output. The probe pulses remains the same as before, and their spectrum is centered at 655 nm.

The experimental data for wider pump pulses is shown in the top row of Fig. 7.10 in the same format used for the narrower pump pulses in Fig. 7.8. The input pump spectrum in part (b) is narrower (width 11 nm). The output spectrum has again two peaks, one at 800 nm, and the other at the red-shifted wavelength. The only difference is that more energy remains in the 800 nm region (37% of input energy compared to 12% in Fig. 7.8b). This is because our wider pump pulse has a larger pulse energy and forms a higher-order soliton after entering the PCF. After a short distance, it breaks into multiple pulses of different widths through a fission-like process [28]. The shortest pulse evolves into a Raman soliton that shifts rapidly toward the red side.

The probe pulse spectra obtained when tuning the initial pump-probe delay are shown in Fig. 7.10a. When we compare them to the probe spectra in Fig. 7.8, we notice similarities but also important differences. In the case of narrower soliton-like pulses shown in Fig. 7.8a, a single reflected pulse is formed for any initial pump-probe delay. In contrast, multiple reflected pulses can form for wider pump pulses in a limited range of pump-probe delay. An example is shown in Fig. 7.10c for a specific delay of 0.5 ps. As seen there, temporal reflection results in three distinct spectral peaks that correspond to three reflected pulses.

To understand the physics better, we performed numerical simulations for wider pump pulses used in the experiment, and the results are shown in Fig. 7.11. For better accuracy, we used the shape of pump pulses deduced with the FROG technique for our simulations. The energy of the pump pulse was set to 18 pJ to ensure that the output Raman soliton matches with what we experimentally observed. This energy is equal to the energy of an $N = 2.5$ soliton with the same temporal FWHM (162 fs). The simulations in Fig. 7.11a show features similar to those observed experimentally in Fig. 7.10a. In particular, multiple reflected pulses indeed form for specific pump-probe delays.

Fig. 7.11c shows the temporal and spectral evolution of pump and probe pulses over the first 1-m-length of the PCF. We only show the first 1m of propagation here because the interaction of the pump pulse and probe pulse only takes place in this region. The input delay is chosen 0.35 ps for this case. The pump pulse breaks into multiple pulses through soliton fission at a distance of about 15 cm. During the fission stage, the pump pulse has a complex intensity pattern, which produces a complex time dependence of the refractive index for the probe pulse. In the case shown in Fig. 7.11c, the probe pulse interacts with different parts of the pump pulse at two distances, resulting in two reflected pulses with different spectral shifts. By comparing the results obtained for a fundamental soliton with those obtained for a higher-order soliton, we can conclude that the process of temporal reflection is sensitive to minute details of the evolution of the pump pulse. This is the reason why the output spectrum of probe pulses contains information about the propagation dynamics of the pump pulse.

7.3.3 Effect of Chirped Pump Pulses

We next consider the case of chirped pump pulses. A simple way to chirp short pulses is to pass them through a dispersive delay line that broadens each pulse while also introducing some frequency chirp. We again use our pulse shaper for this purpose. The slit in the pulse shaper remains fully open, and no spectral filtering takes place. However, one of the prisms inside the pulse shaper is adjusted to introduce some positive chirp on the pump pulse. Before sending this pulse into the PCF, we characterize it with our FROG setup. The measured width is about 97 fs and corresponds to adding 1130 fs^2 of group-delay dispersion to a sech-shape pulse with 22-nm spectral width. The amount of pump pulse energy that couples into the PCF is also adjusted to ensure that the Raman soliton has the same 865-nm wavelength at the PCF's output as before.

The experimental results for chirped pump pulses are shown in Fig. 7.12. Part (a) shows the output probe's output spectra measured while varying the relative pump-probe delay. Part (b) compares the spectrum of the pump pulse at the input and output ends of the PCF. Similar to the case of wide pump pulses, the chirping of the pump pulse increases energy remaining at the input wavelength of 800 nm but by a smaller amount.

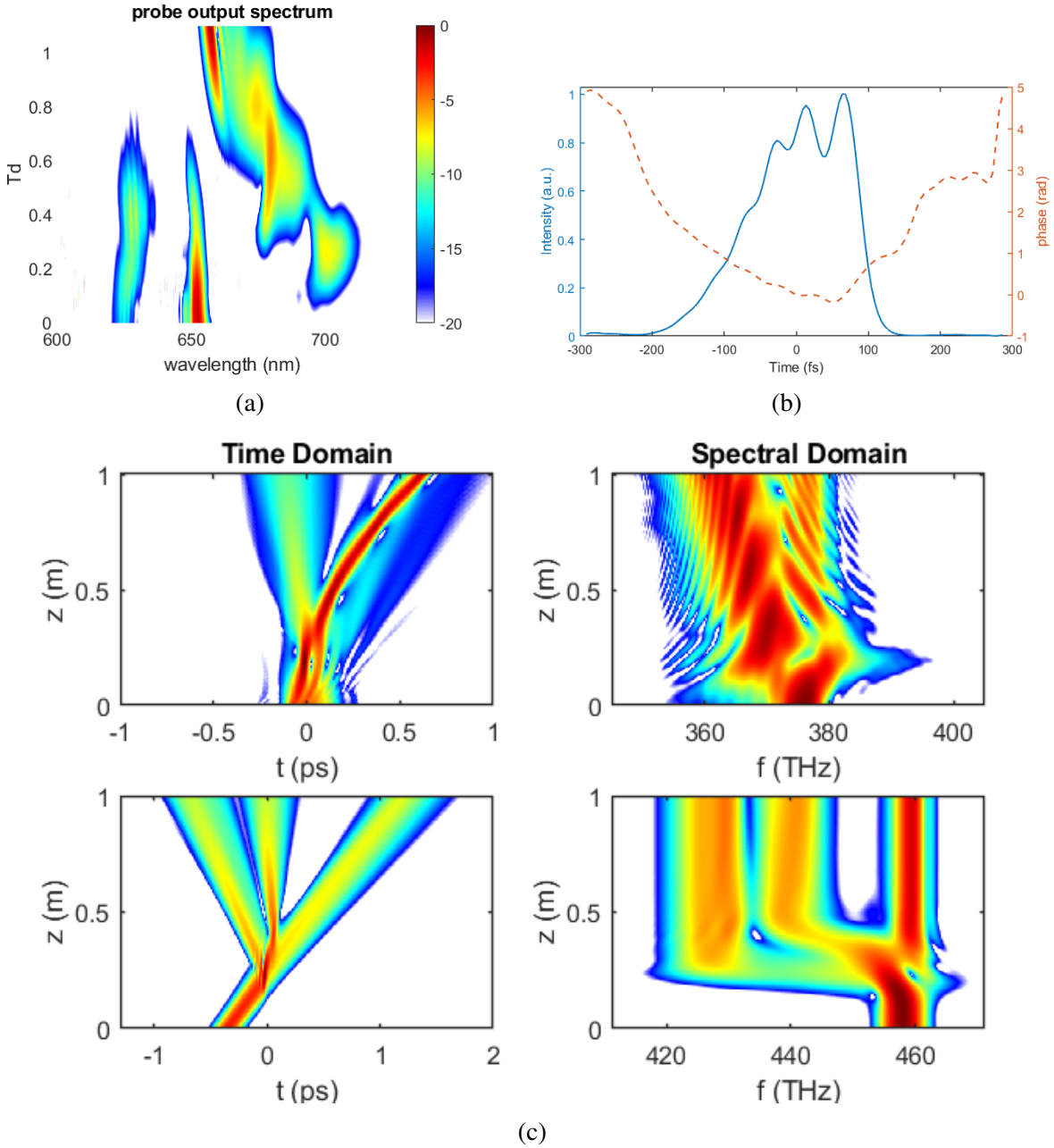

Figure 7.11: Simulation results for wide pump pulses. (a) Spectra of probe pulses at the PCF output as the relative delay is varied. (b) Shape and chirp of the input pump pulse deduced with the FROG technique. (c) Evolution of the pump and probe pulses over the 1-m-length of the PCF.

The probe pulse spectra in part (a) of Fig. 7.12 show a pattern different from the two earlier cases where an unchirped pump pulse forms a fundamental or a higher-order soliton. We expect these differences to result from a different evolution pattern occurring for chirped pump pulses. To confirm this expectation, we performed numerical simulations using the measured shape and phase of input pump pulses, and the results are shown in Fig. 7.13. Part (a) of this figure shows the output probe spectra as a function of pump-probe delay. Part (b) shows the shape and phase of input pump

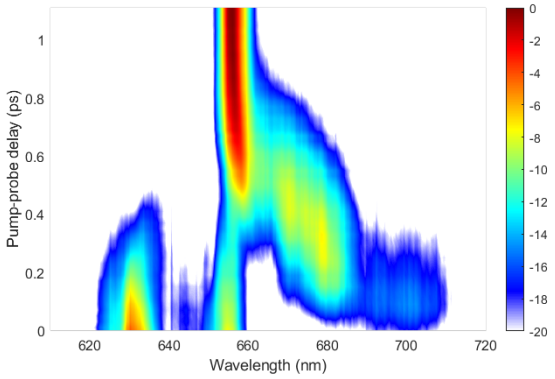

(a)

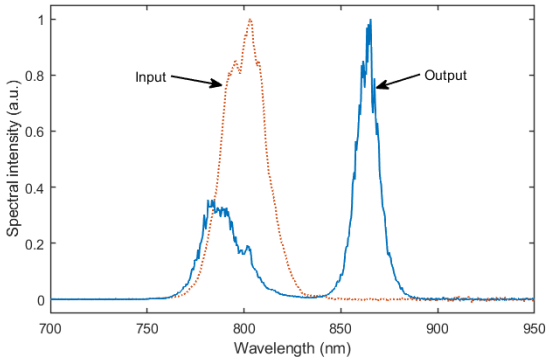

(b)

Figure 7.12: Experimental results for chirped pump pulses. (a) Measured probe spectra at the PCF output as the relative pump-probe delay is varied from 0 to 1 ps. (b) Pump spectra at the input and output ends of the PCF.

pulses obtained with our FROG setup. Part (c) shows the temporal and spectral evolutions of the pump (top) and probe (bottom) pulses over the first 1 m of PCF.

A comparison of the simulated probe spectra with our experimental results in Fig. 7.12a shows a relatively good agreement. In particular, two reflected pulses are produced at different wavelengths when the pump-probe delay is < 0.2 ps. The temporal and spectral evolution of the pump and probe pulses is shown in Fig. 7.13c over the first 1 m of the PCF for a pump-probe delay of 0.15 ps. As seen there, the pump pulse is compressed considerably within the first 10 cm of PCF. Most of its energy forms a fundamental soliton whose spectrum shifts toward the red side, while the remaining energy propagates as a dispersive wave. The probe pulse collides and undergoes two temporal reflections from different parts of the pump pulse. The wavelength of these reflected pulse shifts by different amounts, resulting in the formation of two spectral peaks after a distance of 10 cm. We observed a similar behavior in our experiments when the pump-probe delay was small.

One more feature is noteworthy. Compared with the case of the pump pulse forming a higher order soliton, the Raman soliton for chirped pump pulses is generated at a shorter distance. This implies that temporal reflection of the probe pulse should happen for smaller pump-probe delays. This is indeed what is observed when we compare the experimental results in Fig. 7.10a with those

in Fig. 7.12a. Comparing the observed behavior in the three cases of pump pulses (a fundamental soliton, a higher-order soliton, and a highly chirped pulse), we can conclude that temporal reflection is sensitive to different evolution dynamics of pump pulses occurring inside the PCF. This is the reason why measured probe spectra at the PCF's output can be used to deduce information such as the deceleration of pump pulses initiated by the spectral shift induced by intrapulse Raman scattering.

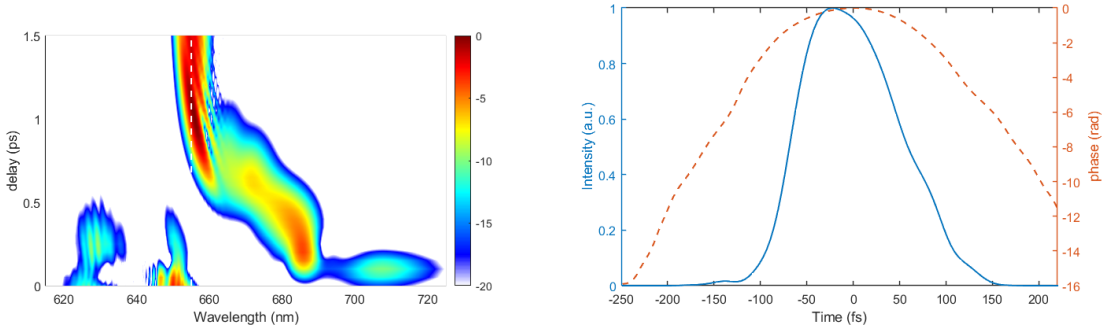

(a) (b)

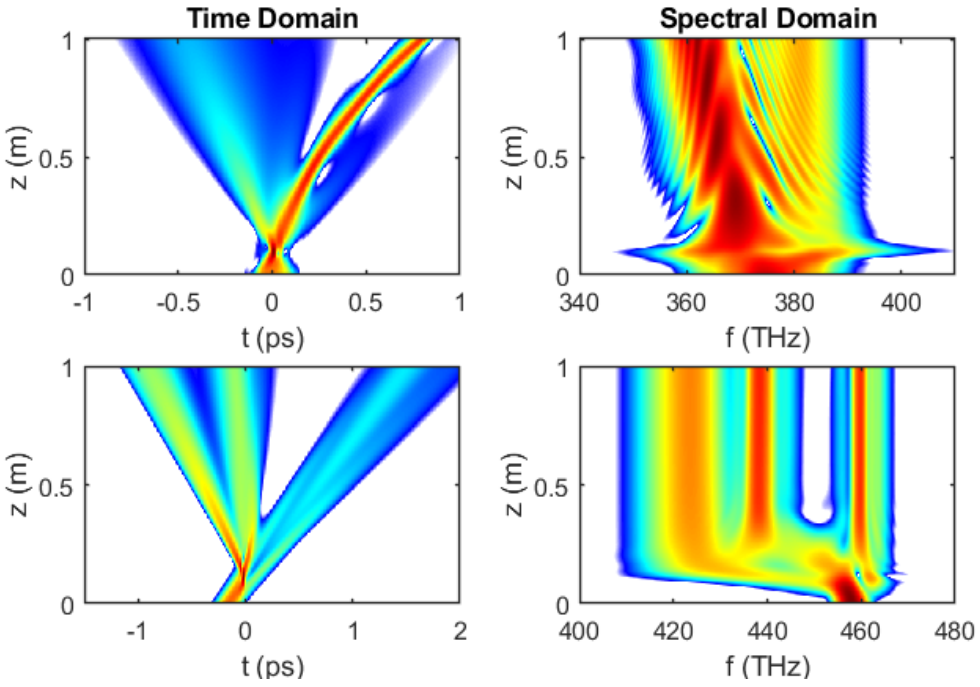

(c)

Figure 7.13: Simulation results for chirped pump pulses. (a) Spectra of probe pulses at the PCF output as the relative delay is varied. (b) Shape and chirp of the input pump pulse deduced with the FROG technique. (c) Evolution of the pump and probe pulses over the 1-m-length of the PCF.

7.4 Discussion and Conclusion

When a short pump pulse propagates as a soliton inside an optical fiber, it creates a moving high-index region through the optical Kerr effect. In this case, the phenomenon of intrapulse Raman scattering provides a speed-changing mechanism for the solitons by red-shifting the soliton's spectrum in a continuous fashion. If a probe pulse is launched into the same fiber with a delay such that it approaches the soliton at some location within the fiber, another pulse is generated through temporal reflection whose wavelength differs considerably from that of the probe pulse. As one would expect, the process of temporal reflection and the spectral shift produced by it depend on the speed of the speed at that specific location. In this work, we propose and demonstrate that the trajectory of the decelerating soliton can be probed using temporal reflection of probe pulses with different delays.

Although we demonstrated the proposed technique for probing a soliton's trajectory, we believe that it can be used as a diagnostic tool for many other optical processes. For example, it may be possible to use a similar technique for probing the dispersive properties of a tapered waveguide. Tapering of a waveguide produces changes in its transverse size all along the length of the waveguide. When a short pulse is launched into a tapered waveguide such as an optical fiber, its speed changes along the fiber's length. Similar to the case of RIFS studied in this paper, the reflected pulse's wavelength would depend on the dispersive properties of the fiber at the location where the pump and probe pulses collide. The tapering approach is more versatile than the RIFS studied here because one has more control over the nature and magnitude of speed changes.

We also studied the dependence of temporal reflection on several parameters of the pump pulse that affected its nonlinear propagation dynamics. We found that the temporal reflection of probe pulses exhibited unexpected novel features when pump pulses were made wider through spectral filtering without much chirp. Similar but different features were observed when pulses were chirped through a dispersive delay line without any spectral filtering. In both cases, two or more reflected pulses were produced at different wavelengths in a specific range of initial pump-probe delays. Numerical simulations reveal that the origin of such novel features is related to a complex nonlinear evolution of pump pulses inside the PCF. The observed novel effects can be interpreted as scattering of the probe wave from the pump's intensity pattern. Similar to how scattering can be used as a diagnostic tool in other branches of physics, we expect that the effect of temporal reflection may be developed as a diagnostic tool for more complicated nonlinear optical processes, such as supercontinuum generation in optical fibers.

Chapter 8

Summary and Future Work

In this dissertation, I have presented my theoretical and experimental work on the topic of temporal reflection of a light pulse at a moving boundary inside a dispersive medium such as an optical fiber.

Theoretically, I developed a method for analyzing the temporal reflections on boundaries of different shapes. I then focused on the effects of a decelerating boundary on temporal reflection, revealing interesting phenomena such as temporal focusing, collimation as well as mode coupling in a bending temporal waveguide.

Experimentally, I performed the experiments to demonstrate temporal reflection inside an optical fiber. Using a short pump pulse to create a decelerating boundary, the effects of temporal pulse trapping were observed, which agreed with our theoretical analysis. I also showed that temporal reflection can be used for probing the behavior of the pump pulse during its propagation.

A future direction of this work is to explore the possibility of realizing the same phenomenon with other physical mechanisms. For example, the refractive index can be changed through the electric-optical effect in a material such as lithium niobate. In this case, by applying an external time-varying voltage, the index experienced by the optical wave is modified. This can be achieved using a traveling wave phase modulator. The obstacle, however, is that the microwave signal used to drive the modulator usually does not turn on fast enough, and the index boundary created is, therefore, not sharp enough to realize efficient reflection. The microwave's bandwidth is usually limited by the signal generator and transmission cables used for sending the microwave signal into the phase modulator. One possible solution for this challenge is to directly generate a transient voltage signal on the phase modulator. We can bridge the transmission lines of the phase modulator, which guides the microwave that modifies the refractive index of the optical waveguide, with a photoconductive switch [95] made of a semiconductor. By sending a short, strong light pulse into this semiconductor, it can be turned from a nearly insulating state to a conducting state, effectively shortening the two transmission lines. As a result, a fast transient voltage can be generated directly on the modulator. It may be possible to achieve temporal reflection of another optical pulse from the boundary of index change created by such a fast transient voltage.

Appendix A

Derivation of q Transformation Law of a Gaussian Pulse

This appendix is a detailed derivation of Gaussian pulse's transformation law when reflected by a Raman soliton (Eq. (4.32)). The symbols are consistent with the discussion in Chapter 4.

When the incident pulse (Eq. (4.24)) is Gaussian, we can use:

$$A_i(0,\tau) = \exp -\frac{1}{2}\Big(\frac{\tau - T_d}{T_2}\Big)^2 \exp -i\delta(\tau - T_d). \tag{A.1}$$

The propagated field can be derived exactly using Eq. (4.24):

$$A_i(z,\tau) = \frac{T_0}{\sqrt{q(z)}} \exp -\frac{(\tau - T_d - \beta_{22}\delta z)^2}{2q(z)} \exp -i\delta(\tau - T_d) + \frac{i\beta_{22}\delta^2 z}{2}, \tag{A.2}$$

where $q(z) = T_2^2 - i\beta_{22}z$ is the complex q parameter.

Then, we need to calculate $A_i(z, az^2)$ and expand it near z_0. Note that z_0 is determined by the quadratic equation:

$$az_0^2 - T_d - \beta_{22}\delta z_0 = 0 \tag{A.3}$$

When expanding, we can approximate $q(z)$ by $q(z_0)$. For other terms, we keep terms up to second-order in $z - z_0$ and neglect all higher-order terms.

$$\begin{aligned} A_i(z, az^2) \approx & \frac{T_0 e^{\frac{i\beta_{22}\delta^2 z_0}{2} - i\delta a z_0^2 + i\delta T_d}}{\sqrt{q(z_0)}} \exp -(\frac{(2az_0 - \beta_{22}\delta)^2}{2q(z_0)} + i\delta a)(z - z_0)^2 \\ & \times \exp i(\frac{\beta_{22}\delta^2}{2} - 2\delta a z_0)(z - z_0) \end{aligned} \tag{A.4}$$

Then, neglecting the phase terms and constants, we do a Fourier transform about z:

$$\begin{aligned} F(k_z) &\propto \int A_i(z, az^2) \exp ia\delta_r (z-z_0)^2 \exp(-ik_z z) dz \\ &\propto \exp(-ik_z z_0) \exp -\frac{(k_z - (\beta_{22}\delta^2/2 - 2az_0\delta))^2}{4[\frac{(2az_0-\beta_{22}\delta)^2}{2q(z_0)} - ia(\delta_r - \delta)]} \\ &= \exp(-ik_z z_0) \exp -\frac{(k_z - (\beta_{22}\delta^2/2 - 2az_0\delta))^2}{4[\frac{(2az_0-\beta_{22}\delta)^2}{2q(z_0)} - 2i\frac{a}{\beta_{22}}(2az_0 - \beta_{22}\delta)]}. \end{aligned} \tag{A.5}$$

Now, we calculate $\tilde{A}_r(\omega)$, neglecting the $\beta_{22}\omega - 2az_0$ term (does not change much within the pulse spectrum) and the $e^{-iaz_0^2\omega}$ term (only leads to a temporal offset) to obtain:

$$\begin{aligned} \tilde{A}_r(\omega) &\propto F(\frac{\beta_{22}\omega^2}{2} - 2az_0\omega) \\ &\propto \exp -\frac{1}{2}(i\beta_{22}z_0 + \frac{1}{\frac{1}{q(z_0)} - \frac{8ia}{\beta_{22}^2(\delta_r - \delta_i)}})(\omega - \delta_r)^2. \end{aligned} \tag{A.6}$$

Note that $\tilde{A}_r(\omega)$ is defined at $z = 0$, thus we have:

$$\begin{aligned} q_r(z_0) &= q_r(0) - i\beta_{22}z_0 \\ &= i\beta_{22}z_0 + \frac{1}{\frac{1}{q(z_0)} - \frac{8ia}{\beta_{22}^2(\delta_r - \delta_i)}} - i\beta_{22}z_0 \\ &= \frac{1}{\frac{1}{q(z_0)} - \frac{8ia}{\beta_{22}^2(\delta_r - \delta_i)}}. \end{aligned} \tag{A.7}$$

Finally, we arrive at the Gaussian pulse transformation law:

$$\frac{1}{q_r(z_0)} = \frac{1}{q_i(z_0)} - \frac{8ia}{\beta_{22}^2(\delta_r - \delta_i)}. \tag{A.8}$$

Appendix B

Dispersion Measurement of Photonic Crystal Fiber

Experimentally, we performed measurements of the dispersion profile of the photonic crystal fiber (PCF) used for the temporal reflection experiment. This information is then used for theoretical modeling of temporal reflection, which is compared with the experimental results.

The technique used for the measurement is called white light interferometry [91, 92]. The setup is shown in Fig. B.1.

The setup is a Michelson interferometer using a white light laser as the light source (NKT Photonics). One arm is the reference arm, with a mirror mounted on a translational stage for delay control. The second arm is the test arm. In the test arm, the laser is focused into a piece of PCF (about 10 cm long). The Fresnel reflection from the front and back ends of the PCF are collected by the lens. The reflected light pulses from the reference arm and test arm are combined and sent into an OSA. The spectrum measured by the OSA shows interference in the spectral domain, and it can be used for extraction of the dispersion profile of the PCF.

Here, we give an analysis of this technique in the frequency domain. Suppose the light field at the input of the interferometer is $\tilde{E}_{in}(\omega)$. The light field after combining the reference arm and test arm can be written in the following expression:

$$\begin{aligned}\tilde{E}_{out}(\omega) =& \sqrt{R_{ref}}\tilde{E}_{in}(\omega)e^{i(\phi_0(\omega)+\frac{2\omega z}{c})} \\ &+ \sqrt{R_f}\tilde{E}_{in}(\omega)e^{i\phi_1(\omega)} + \sqrt{R_b}\tilde{E}_{in}(\omega)e^{i(\phi_1(\omega)+2\beta(\omega)L)}. \end{aligned} \tag{B.1}$$

In Eq. (B.1), the three terms correspond to the fields from the reference arm, reflection from the front end of the PCF, and the reflection from the back end of the PCF respectively. R_{ref}, R_f and R_b are coefficients describing the ratio of the energy that gets transmitted through each path. These coefficients should be only weakly dependent on the optical frequency, and they can be regarded as frequency-independent in the interferometry experiment. In each path, we need to consider the phase delay. In the reference arm, the phase term is written as $\phi_0(\omega)+\frac{2\omega z}{c}$. Here, z is the position of the translational stage, and $\phi_0(\omega)$ is the phase when the translational stage is set at position 0. For the front surface reflection, the phase change is given by $\phi_1(\omega)$. For the back surface reflection, the phase change has an additional $2\beta(\omega)L$, where $\beta(\omega)$ is the propagation constant of the mode of the PCF, and L is the length of the PCF sample.

At the spectrum analyzer, we measured the spectral intensity $S_{out}(\omega) = |\tilde{E}_{out}(\omega)|^2$. Apparently, in the spectral intensity, we will have interference from the three terms in Eq. (B.1). We first look

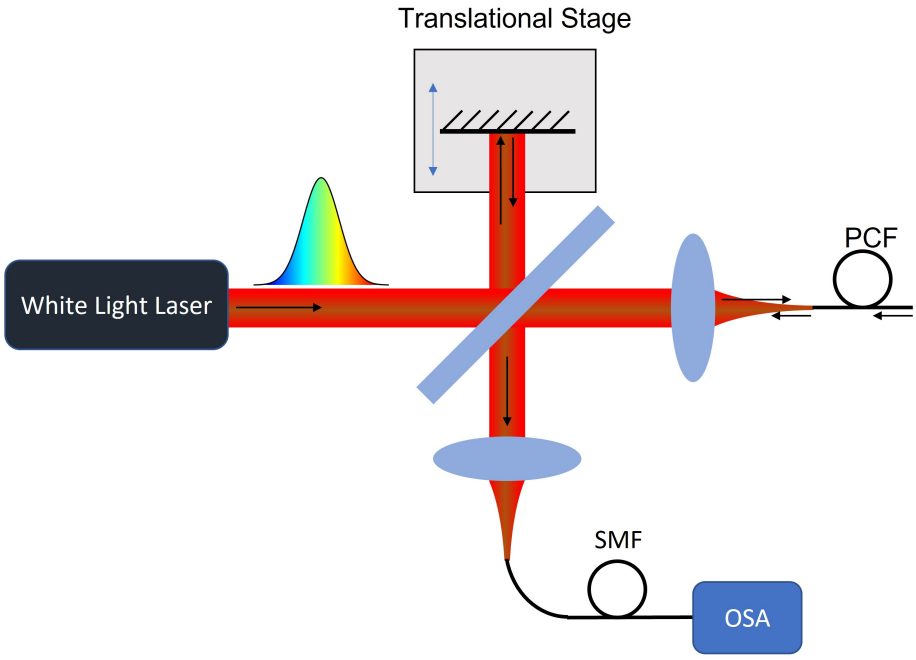

Figure B.1: Setup of dispersion measurement using white light interferometry. PCF: photonic crystal fiber. OSA: optical spectrum analyzer. SMF: single mode fiber.

at the interference term from the reference arm and the reflection from the front surface of PCF:

$$\begin{aligned} S_{ref,f}(\omega) &= \sqrt{R_{ref}}\tilde{E}_{in}(\omega)e^{i(\phi_0(\omega)+\frac{2\omega z}{c})} \times (\sqrt{R_f}\tilde{E}_{in}(\omega)e^{i\phi_1(\omega)})^* + c.c. \\ &= 2\sqrt{R_{ref}R_f}S_{in}(\omega)\cos\left(\phi_0(\omega)+2\frac{\omega z}{c}-\phi_1(\omega)\right). \end{aligned} \tag{B.2}$$

In the equation above, we defined $S_{ref,f}(\omega)$ as the terms involving the interference between the reference arm and the reflection from the PCF's front end. These terms can be obtained by expanding the measured spectral intensity $S_{out}(\omega)$ using Eq. (B.1). From Eq. (B.2), we see the interference in the spectral domain. The local period of interference can be estimated in the following equation:

$$\frac{d\left(\phi_0(\omega)+2\frac{\omega z}{c}-\phi_1(\omega)\right)}{d\omega}\Delta\omega = 2\pi, \tag{B.3}$$

where $\Delta\omega$ is the period of the interference fringes in the spectrum. Define $\tau_{0,1} = d\phi_{0,1}/d\omega$, which are the group delays of the optical elements in each path (delay caused by the translational stage is not included). Then, we arrive at:

$$(\tau_0 + \frac{2z}{c} - \tau_1)\Delta\omega = 2\pi. \tag{B.4}$$

The first term on the left-hand side is the group delay difference of the two arms (including the contribution from the translational stage). Experimentally, the measurement of the spectrum has a finite resolution in ω. When the group delays are too big, the period of interference is so small

that the measurement system will simply wash them out and no interference can be measured. The interference can only be observed when the translational stage's position is set such that the total group delay of the reference arm is very close to that of the light reflecting from the front end of the PCF. For a measurement resolution of $\Delta\lambda = 2$ nm at a wavelength of $\lambda = 800$ nm, the offset of the position of the stage from the zero-delay position should be within 0.16 mm. This number shows that the interference between the front-end and back-end reflections cannot be observed, as they have such a big delay difference (fiber is about 10 cm long). Also, the reference arm can only interfere with at most one reflection from the PCF, either the front reflection or the back reflection depending on the position of the translational stage. Thus, if we first consider that the translational stage is set at a position such that the reference light can interfere with the front-end reflection, the back-end reflection can simply be regarded as an incoherent background. Then, the measured spectrum can be expressed by:

$$\begin{aligned} S_{out}(\omega) =& (R_{ref} + R_f + R_b) S_{in}(\omega) \\ &+ 2\sqrt{R_{ref} R_f} S_{in}(\omega) \cos\left(\phi_0(\omega) + 2\frac{\omega z}{c} - \phi_1(\omega)\right). \end{aligned} \tag{B.5}$$

We can extract the fringes by performing a measurement of the reference arm alone, giving us $S_{ref}(\omega) = R_{ref} S_{in}(\omega)$, and performing a measurement of the test arm alone, giving us $S_{test}(\omega) = (R_f + R_b) S_{in}(\omega)$. Then, we perform the analysis:

$$F = \frac{S_{out} - S_{in} - S_{test}}{2\sqrt{S_{in} * S_{test}}} = \sqrt{\frac{R_f}{R_f + R_b}} \cos\left(\phi_0(\omega) + 2\frac{\omega z}{c} - \phi_1(\omega)\right). \tag{B.6}$$

The quantity F contains the spectral interference fringes. To see how we can extract the dispersion from this measurement, in Fig. B.2, we show an example of the experimentally measured F. We clearly see the spectral fringes from the interference. At the shorter wavelength side of Fig. B.2, we see that the fringe visibility drops to almost zero. This is because the local fringe period approaches the resolution of the spectrum analyzer. We have also identified a special point in the data, which we call the stationary phase point. Let's denote it as ω_s. This point satisfies the following relation:

$$\left.\frac{d\left(\phi_0(\omega) + 2\frac{\omega z}{c} - \phi_1(\omega)\right)}{d\omega}\right|_{\omega_s} = 0, \tag{B.7}$$

which leads to the following relation:

$$\frac{2z}{c} = \tau_1(\omega_s) - \tau_0(\omega_s). \tag{B.8}$$

This equation simply means that the group delay at the stationary phase point is matched between the two beams. Because of the dispersion of the optical elements, there is a distinct stationary phase point at each position of the translational stage, and the location of this point also depends on the position of the translational stage. Thus, we measure the stationary phase point ω_s while varying z. From Eq. (B.8), we obtain the function $\tau_1(\omega) - \tau_0(\omega)$. One advantage of using this stationary phase point instead of directly measuring the phase of the fringe itself is that this stationary phase point is more robust against small perturbations.

Similarly, we can then adjust the position of the translational stage such that the reference light interferes with the back-end reflection from the PCF. By performing the same measurement, we obtain the fringe function:

$$F' = \sqrt{\frac{R_b}{R_f + R_b}} \cos\left(\phi_0(\omega) + 2\frac{\omega z}{c} - \phi_1(\omega) - 2\beta(\omega)L\right). \tag{B.9}$$

An example of data is shown in Fig. B.3. We also observe the spectral interference as in the previous case. The difference is that we have two stationary phase points. This happens because the PCF has a normal dispersion region and an anomalous dispersion region. As a result, the group velocity matching condition can be satisfied for two wavelengths.

For this case, the stationary phase points satisfy the following relation:

$$\frac{2z}{c} = \tau_1(\omega_s) + 2\beta_1(\omega_s)L - \tau_0(\omega_s), \tag{B.10}$$

where $\beta_1 = d\beta/d\omega$ is the inverse of the group velocity of the mode of the PCF. In the same way, we can measure the stationary phase points while scanning the position of the translational stage. We thus obtain the function $\tau_1(\omega) + 2\beta_1(\omega)L - \tau_0(\omega)$. With the knowledge of $\tau_1(\omega) - \tau_0(\omega)$, we can obtain the function $\beta_1(\omega)$, which completely determines the group velocity dispersion of the PCF. The result is shown in Fig. 6.1 by showing the group index of the PCF as a function of wavelength.

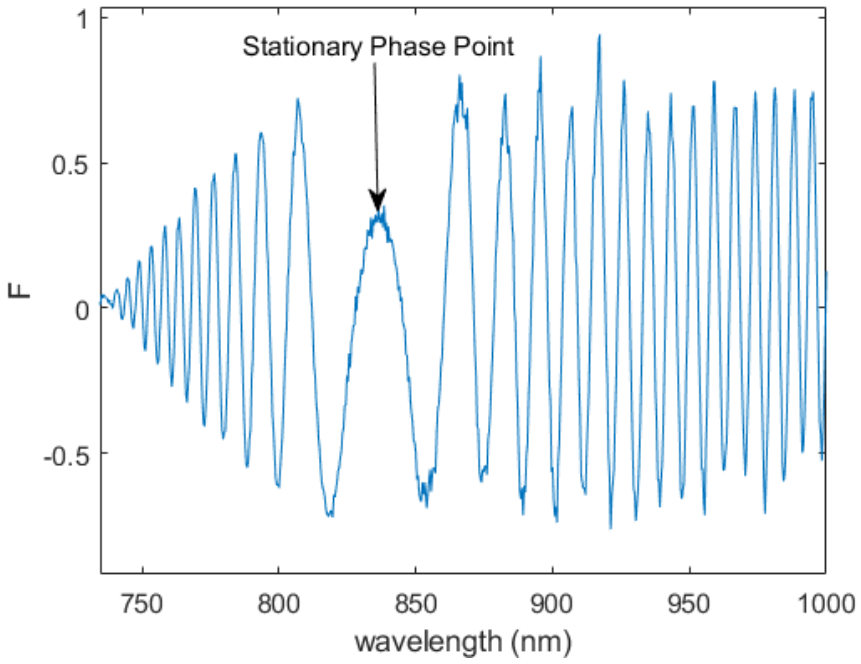

Figure B.2: Spectral fringes from experiments. A stationary phase point can be observed

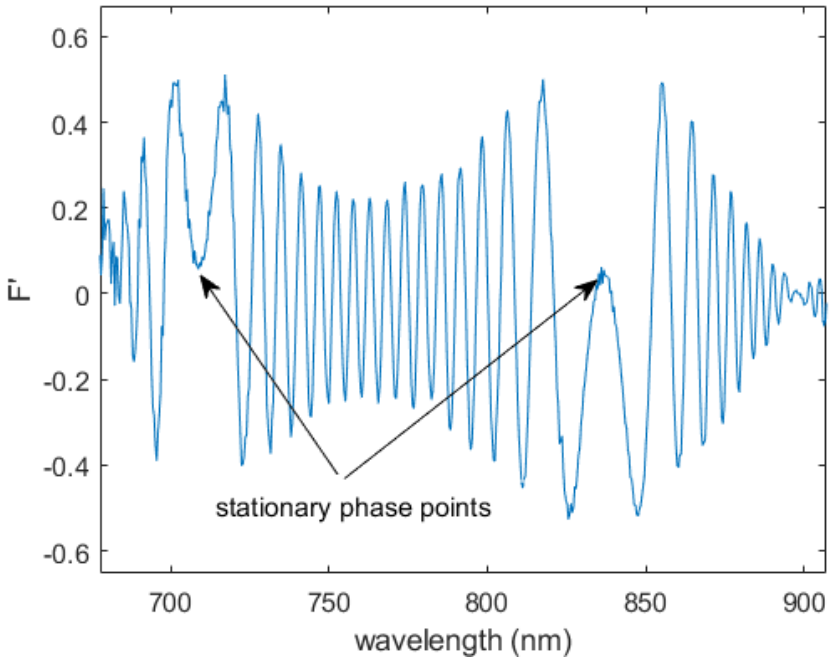

Figure B.3: Spectral fringes from interference between the reference light and back end reflection of PCF.

Appendix C

Extraction of Raman Soliton Trajectory

In Chapter 7, we showed that we retrieved the Raman soliton's trajectory based on the reflected pulse spectrum as we scanned the relative pump-probe delay at the input. The retrieved trajectory is shown in Fig. 7.6. In this appendix, we provide additional details about the modeling of temporal reflection from a decelerating soliton representing a high-index barrier. We also discuss how we inferred the soliton's trajectory from the measured spectral data.

Soliton's Evolution inside the PCF

The evolution of a short optical pulse inside any optical fiber is governed by Eq. (7.2) of the main text. This equation includes the effects of intrapulse Raman scattering through the nonlinear term N_R, which depends on the Raman response function h_R. Numerical solutions of this equation show that the soliton's spectrum shifts to the red side inside the PCF in a continuous manner (see Fig. 7.2a). Here, we use a semi-analytic approach for solving this equation and assume that the soliton maintains its sech-shape inside the PCF but acquires a Raman-induced frequency shift (RIFS) that decelerates the soliton and delays it. Both the frequency shift and temporal delay of the Raman soliton can be included by writing the solution of Eq. (7.2) in the form

$$A_s(z,\tau) = \sqrt{P_s(z)}\,\mathrm{sech}\Big(\frac{\tau-\tau_s(z)}{T_s(z)}\Big)e^{-i\delta_s(z)\tau+i\phi(z)}, \tag{C.1}$$

where $\delta_s(z)$ is the RIFS and $\tau_s(z)$ is the delay caused by this shift. The peak power P_s and the width T_s of the soliton can also vary with z.

Based on the dispersion properties of the fiber, the time delay satisfies the simple equation,

$$\frac{d\tau_s}{dz} = \Delta\beta_1(\delta_s), \tag{C.2}$$

where $\Delta\beta_1$ is the change in the propagation constant because of the RIFS. It can be written as

$$\Delta\beta_1(\delta_s) = \beta_1(\omega_s+\delta_s) - \beta_1(\omega_s) = \sum_{k\geq 2}\frac{\beta_k^{(s)}}{(k-1)!}\delta_s^{k-1}. \tag{C.3}$$

where we used the Taylor expansion of β. As (C.2) establishes a relation between the soliton's delay and RIFS, if we know $\delta_s(z)$, we can integrate this equation to obtain $\tau_s(z)$. Similarly, if we know $\tau_s(z)$, we can calculate $\Delta\beta_1(\delta_s(z))$ by differentiating it and find $\delta_s(z)$ by using the polynomial in (C.3) with the known dispersion parameters.

The soliton's peak power and its width are related by the area theorem stating that the nonlinear and dispersion lengths must be equal [28], i.e.,

$$\gamma P_s = |\beta_2(\omega_s + \delta_s)|/T_s^2. \tag{C.4}$$

As the number of photons N contained within a soliton should also remain the same (assuming negligible radiation), we have the relation

$$N = \frac{\int |A_s|^2 dt}{\hbar(\omega_s + \delta_s)} = \frac{2P_s T_s}{\hbar(\omega_s + \delta_s)}. \tag{C.5}$$

The value of N can be estimated by measuring the soliton's energy $E_s = 2P_s T_s$ at the output end of the fiber. Using (C.4) and (C.5), we can find the soliton's peak power and its width for any value of frequency shift δ_s. In other words, All quantities appearing in (C.1) can be determined at any location within the fiber if either $\tau_s(z)$ or $\delta_s(z)$ is known. Our goal is to use the spectral data to infer the trajectory of $\delta_s(z)$ or $\tau_s(z)$ based on the measured spectra for the reflected pulse. This trajectory does not always agree with numerical simulations of Eq. (7.2), because the modeling of the Raman effect is based on a phenomenological Raman response function, and as a result, it is very difficult to accurately predict the Raman soliton's trajectory purely from simulation.

Wavelength of Reflected Pulse

Let us first discuss how we can calculate the wavelength of the reflected probe pulse along the soliton's trajectory. We assume that $\tau_s(z)$ is known. In the reference frame moving with the soliton, $t = 0$ corresponds to the soliton's peak at $z = 0$. The peak of the probe pulse is at $t = -T_d$, where $T_d > 0$ is the delay of the soliton relative to the probe pulse. As the probe pulse propagates through the fiber, its center follows the trajectory:

$$\tau_p(z) = -T_d + \Delta\beta_1^{(p)} z. \tag{C.6}$$

Temporal reflection occurs when the trajectories of the soliton and probe pulse intersect at some distance inside the fiber. Denoting this distance as z_c, the two pulses collide when

$$\tau_p(z_c) = \tau_s(z_c). \tag{C.7}$$

This equation can be solved when the soliton's trajectory $\tau_s(z)$ is known.

We calculate the central frequency of the reflected pulse using the phase continuity relation given in Eq. (1). Transforming this equation into the moving frame, we obtain

$$\frac{\kappa(\delta_r)}{\delta_r} = \left.\frac{d\tau_s}{dz}\right|_{z=z_c}, \tag{C.8}$$

where $\delta_r = \omega_r - \omega_p$ is the frequency shift during temporal reflection and κ is defined as

$$\kappa(\delta_r) = \Delta\beta_1^{(p)}\delta_r + \sum_{k\geq 2}\frac{\beta_k^{(p)}}{k!}\delta_r^k. \tag{C.9}$$

The reflected pulse's frequency shift δ_r can be calculated from (C.8). During this calculation, we use the velocity of the soliton at the collision point, which amounts to neglecting any deceleration during the reflection process. This is a reasonable approximation. The dashed line in Fig. 7.3 was obtained with this method.

Determination of soliton's trajectory

The previous section provided a way of calculating the reflected pulse's frequency for a known soliton's trajectory. In this section, we consider the inverse problem: how can one extract a soliton's trajectory based on the measured delay dependence of the reflected pulse's spectrum? Mathematically, this dependence can be expressed by the function $\delta_r(T_d)$. From (C.6) and (C.7), the initial delay of a probe pulse colliding with the soliton at position z should be $T_d = \Delta\beta_1^{(p)}z - \tau_s(z)$. Using this relation, (C.8) becomes a first-order differential equation for the soliton's trajectory:

$$\frac{d\tau_s}{dz} = \frac{\kappa(\delta_r(\Delta\beta_1^{(p)}z - \tau_s))}{\delta_r(\Delta\beta_1^{(p)}z - \tau_s)} \tag{C.10}$$

(C.10) allows one to extract the trajectory of the soliton, $\tau_s(z)$, from the delay dependence of reflected pulse's spectrum. Typically, data taken for a single probe's wavelength allows one to retrieve only a portion of this trajectory. The entire trajectory is retrieved by stitching together the results obtained with several probes at different wavelengths. The trajectory obtained this way is shown in Fig. C.1. Different parts of this trajectory are obtained from different probe wavelengths. The trajectory over the first 0.5m was found using a parabolic function because the higher-order soliton creates a Raman soliton through the fission process over this distance.

To show the effectiveness of the preceding method, we performed simulations for the temporal reflection of a probe pulse by solving Eq. (4) numerically using the soliton's amplitude in the form of (C.1). The solitons parameters appearing in (C.1) were calculated from the trajectory retrieved using (C.10). The results are shown in Fig. C.2. Although the trend looks correct, calculated wavelengths of reflected pulses differ somewhat from measured values because of the approximations made.

To improve the predicted values of wavelengths, we used an iterative approach. We used the trajectory obtained from (C.10) as a starting point and minimized the discrepancy between the measured and simulated results with few iterations. This procedure gave us the retrieved RIFS trajectory shown in Fig. 9(d). Using this trajectory, we compare the experimental results with our simulated results in Fig. C.3, showing an overall excellent agreement.

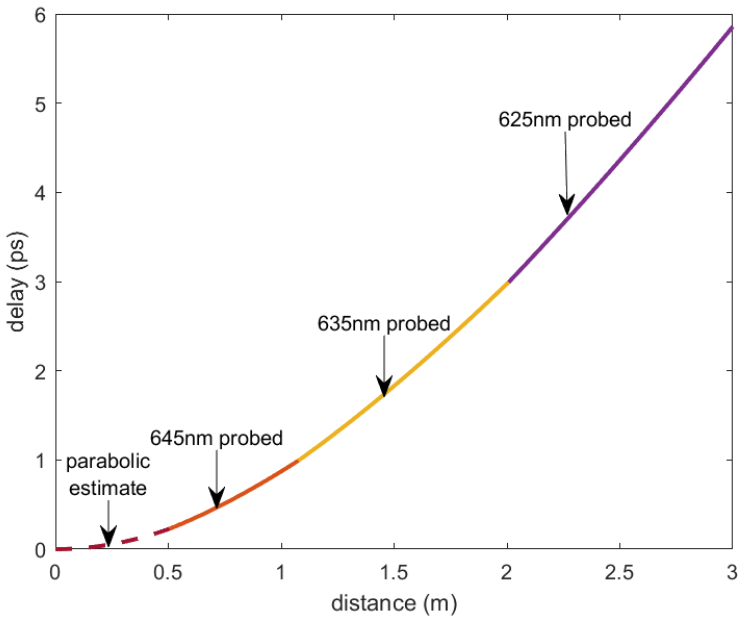

Figure C.1: Soliton trajectory obtained from (C.10). Different parts of the trajectory are obtained from measurements using different probe wavelengths. The first 0.5m is estimated with a parabolic shape.

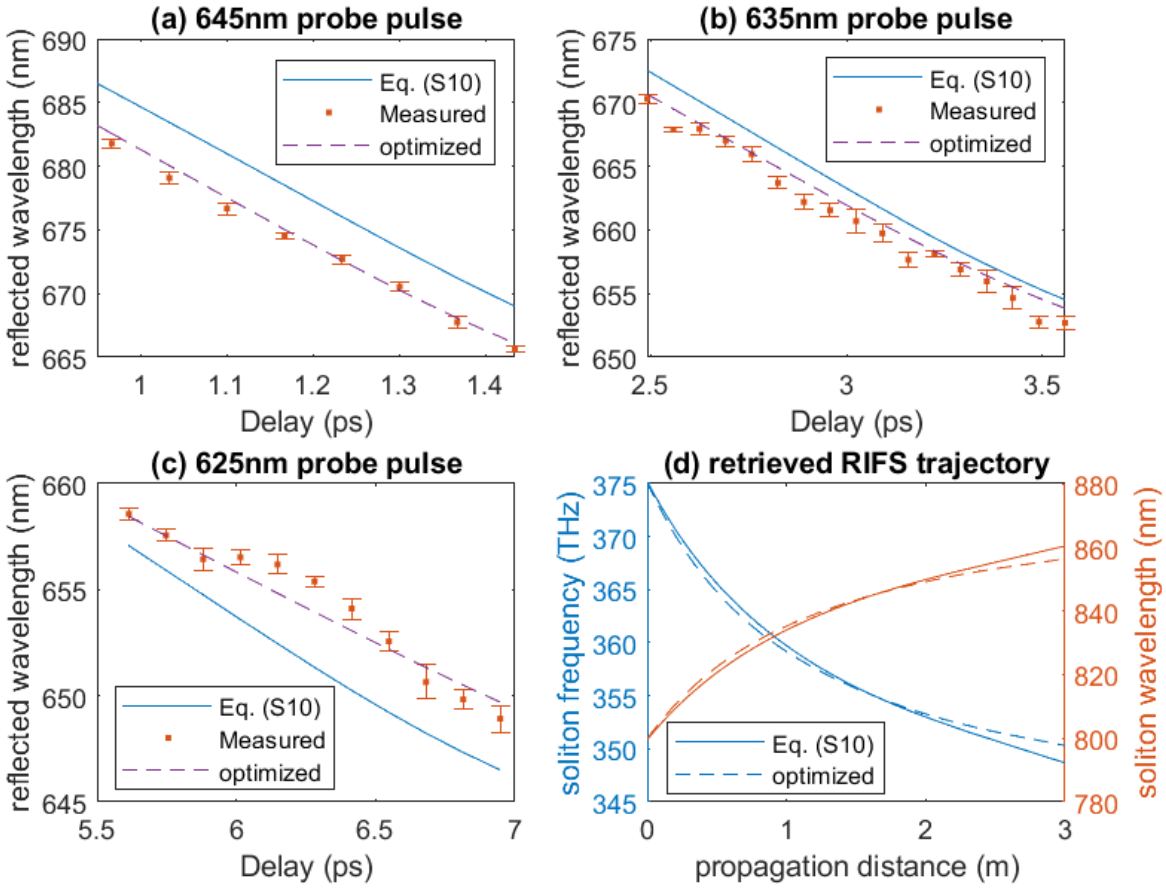

Figure C.2: (a), (b) and (c): Simulated reflected wavelength based on the trajectory obtained with Eq. (C.10) and the optimized trajectory. (d) The trajectory obtained by Eq. (C.10) and the optimized trajectory.

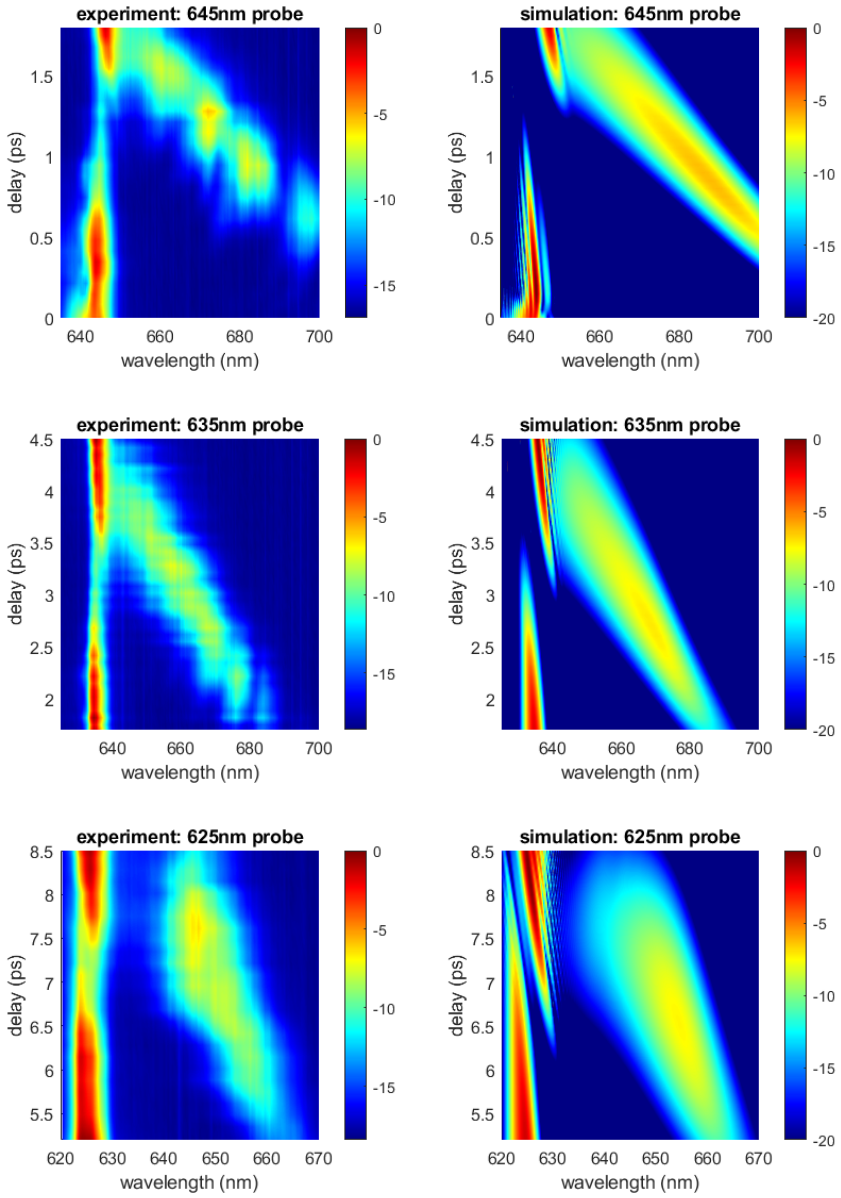

Figure C.3: Comparison of the output probe pulse spectrum. The left column shows the measured data. The right column shows the simulation result based on the retrieved RIFS trajectory through optimization.

Appendix D

Simulation Code

In this appendix, I provide an example of simulation code. This code simulates the pulse propagation using Eq. (2.28). It is written in MATLAB.

There are two files to run the simulation. The main script is the one that defines the input parameters. It calls a function file that performs the simulation and returns the results. The results are then visualized by the main script.

Main script: TemporalReflectionSim.m:

```
% propagation length is in km, time is in ps, wavelength is in m
clear;
c=3e8;
Nt=2^14;% number of points in the time window
Nz=200;% number of points in the propagation direction

ratio_E=0.05;%ratio of the energy of probe pulse relative to pump pulse
lam2_FWHM=5e-9;%spectral FWHM of probe pulse in m
Td=1.2;%pump delay relative to probe


Tmax=10;% maximum time in the time window (time window width is twice of this)
dt=2*Tmax/Nt;
tau=(-Nt/2:Nt/2-1)*dt;% time window variable
nu_max=1/2/dt;

lam_ref=800e-9;% reference wavelength (corresponds to omega_0), wavelength uses SI unit
omega_ref=2*pi*c/lam_ref/1e12;% reference angular frequency in 1/ps

% dispersion parameters, beta(n)=beta_n in the equation. beta(1) is not
% used. Unit is in km and ps
beta=[0;-13.3;0.07;-5e-05];

gamma=1*105;% nonlinear coefficient in 1/W/km
lam1=800e-9;% input pump pulse central wavelength
```

```
lam2=645e-9;% input probe pulse central wavelength

% include possible attenuation (as a function of wavelength). not used in this example
lam_att=[610,1600]*1e-9;
alphadB=0*[90,90];

domega2=2*pi*c/lam2^2*lam2_FWHM/2/sqrt(log(2))/1e12;
T2=1/domega2;% pulse width parameter for the probe pulse

T1=1*16e-3;% pump pulse width (not FWHM)

distance=3.75e-3;% total propagation length in km

% frequency offset from the reference frequency of the pump and probe pulses
delta_nu1=c*(1/lam1-1/lam_ref)/1e12;
delta_nu2=c*(1/lam2-1/lam_ref)/1e12;

P1=abs(beta(2,1))/gamma/T1^2;% input pump pulse peak power, use fundamental soliton here

tau_shock=lam_ref/2/pi/c*1e12;% defined as 1/omega_0, for self-steepening term

A1=1*sqrt(P1)*sech(tau/T1);% input pump pulse shape
A2=exp(-0.5*(tau+Td).^2/T2^2);% probe pulse shape

% rescale probe pulse shape such that the ratio of its energy to the pump
% pulse's energy is ratio_E
A2=sqrt(ratio_E*sum(abs(A1).^2)/sum(abs(A2).^2))*A2;

% define the total input pulse envelope used in the simulation equation
A=1*A1.*exp(-1i*2*pi*delta_nu1*tau)+1*A2.*exp(-1i*2*pi*delta_nu2*tau);

% visualize the input pulse shape
figure,
yyaxis left,
plot(tau,abs(A1).^2);
ylabel('pump pulse intensity (W)');

yyaxis right,plot(tau,abs(A2).^2);
ylabel('probe pulse intensity (W)');
xlabel('\tau (ps)');

%% numerically solve the propagation equation
[AT,AW,omega,Z]=GNLSE_loss_ode45(lam_ref,tau,A,lam_att,1*alphadB,beta,1*gamma,1*tau_shoc
%% visualize the results
tlim=[-1,5];% time window for plotting
```

```
clim=[-35,0];% colorplot limit (in dB)
flim=[330,490];% frequency window for plotting (actual optical frequency in THz)

IT=abs(AT).^2;
ITmax=max(max(IT));
lIT=10*log10(IT/ITmax);
IW=abs(AW).^2;
IWmax=max(max(IW));
lIW=10*log10(IW/IWmax);% calculate the power (temporal and spectral) in dB

% color plot of the total pulse (pump and probe)
figure,subplot(2,1,1);
imagesc(tau,Z*1e3,lIT);
set(gca,'YDir','normal');
colorbar;
colormap (1-jet);
xlabel('t (ps)');
ylabel('z (m)');
xlim(tlim);
caxis(clim);
subplot(2,1,2);
imagesc(omega_ref/2/pi+omega/2/pi,Z*1e3,lIW);
set(gca,'YDir','normal');
colorbar;
colormap (1-jet);
xlabel('f (THz)');
ylabel('z (m)');
xlim(flim);
caxis(clim);
if exist('flag_scan','var')==1
    saveas(gcf,foldername+"\"+figname1);
    close all;
end
%% filtering out the pump and probe separately
filter=zeros(1,Nt);
Nu_range=80;
% filter the probe pulse
filter((omega+omega_ref)/2/pi>405 & (omega+omega_ref)/2/pi<515)=1;
AT_filtered=0*AT;
AW_filtered=0*AW;
for k=1:Nz
AW_filtered(k,:)=AW(k,:).*filter;
AT_filtered(k,:)=fft(ifftshift(AW_filtered(k,:)))/Nt/dt;
end
```

```
% the remaining is the pump pulse
AT_filtered_out=AT-AT_filtered;
AW_filtered_out=AW-AW_filtered;

IT_filtered=abs(AT_filtered).^2;
ITmax_filtered=max(max(IT_filtered));
lIT_filtered=10*log10(IT_filtered/ITmax_filtered);
IW_filtered=abs(AW_filtered).^2;
IWmax_filtered=max(max(IW_filtered));
lIW_filtered=10*log10(IW_filtered/IWmax_filtered);

IT_filtered_out=abs(AT_filtered_out).^2;
ITmax_filtered_out=max(max(IT_filtered_out));
lIT_filtered_out=10*log10(IT_filtered_out/ITmax_filtered_out);
IW_filtered_out=abs(AW_filtered_out).^2;
IWmax_filtered_out=max(max(IW_filtered_out));
lIW_filtered_out=10*log10(IW_filtered_out/IWmax_filtered_out);

figure,subplot(2,2,1);
imagesc(tau,Z*1e3,lIT_filtered_out);
set(gca,'YDir','normal');
colorbar;
colormap jet;
xlabel('t (ps)');
ylabel('z (m)');
title('Pump Temporal');
xlim(tlim);
caxis(clim);
subplot(2,2,2);
imagesc(omega_ref/2/pi+omega/2/pi,Z*1e3,lIW_filtered_out);
set(gca,'YDir','normal');
colorbar;
colormap jet;
title('Pump Spectral');
xlabel('f (THz)');
ylabel('z (m)');
xlim([330,400]);
caxis(clim);

subplot(2,2,3);
imagesc(tau,Z*1e3,lIT_filtered);
set(gca,'YDir','normal');
colorbar;
colormap jet;
title('Probe Temporal');
```

```
xlabel('t (ps)');
ylabel('z (m)');
xlim(tlim);
caxis(clim);
subplot(2,2,4);
imagesc(omega_ref/2/pi+omega/2/pi,Z*1e3,lIW_filtered);
set(gca,'YDir','normal');
colorbar;
colormap jet;
title('Probe Spectral');
xlabel('f (THz)');
ylabel('z (m)');
xlim(omega_ref/2/pi+delta_nu2+[-1,1]/2*Nu_range);
caxis(clim);

% plot the spectrum with wavelength
lam_sim=2*pi*c./(omega_ref+omega)/1e3;
lam_lim=[600,900];
figure,plot(lam_sim,IW(end,:));
xlabel('wavelength (nm)');
ylabel('spectral intensity (a.u.)');
xlim(lam_lim);
if exist('flag_scan','var')==1
    saveas(gcf,foldername+"\"+figname3);
    close all;
end
\end{lstlisting}

The function file GNLSE\_loss\_ode45.m:
\begin{lstlisting}
    function [AT,AW,omega,Z]=GNLSE_loss_ode45(lambda_ref,tau,A1,lam_att,alphadB,beta,gam
%lambda0 is in m, beta is in ps and km
%lambda (m) and alphadB defines the wavelength dependent attenuation in dB/km
dtau=tau(2)-tau(1);
Nt=length(tau);
n_beta=size(beta,1);
Tmax=Nt*dtau/2;

omega = fftshift((pi/Tmax)*(-Nt/2:Nt/2-1));
% fftshift the frequency so that no need to perform fftshift after doing fft for the pul

omega_ref=2*pi*3e8/(lambda_ref)/1e12;%in THz
D1=zeros(size(omega));
% use the dispersion parameters to construct the dispersion operator in the frequency do
for k=2:n_beta
```

```
    D1=D1+1i*beta(k,1)/factorial(k)*omega.^k;
end

% take into account of the possible attenuation (wavelength dependent)
alpha_temp=alphadB/10*log(10);
lam_temp=lam_att*1e9;
c=3e8;
alpha=interp1(lam_temp,alpha_temp,2*pi*c./((omega_ref+omega)*1e12)*1e9,'linear',0);
D1=D1-alpha/2;

% construct the Raman response function hR
fb=1*0.21;
taub=96e-3;
fR=1*0.245;
tau1=12.2e-3;
tau2=32e-3;
hR_new=(1-fb)*(1/tau1^2+1/tau2^2)*tau1*exp(-tau/tau2).*sin(tau/tau1)
    +fb*(2*taub-tau)/taub^2.*exp(-tau/taub);
hR_new(tau<0)=0;

function R=rhs(z,AW)
% evaluate the right hand side of Eq. (2.31), AW in this function actually
% corresponds to B(z,omega).

AT_temp=fft(AW.'.*exp(D1*z));% get the temporal pulse shape

% evaluate the nonlinear operator in the time domain

% convolution of the pulse intensity with Raman response function
conv=real(Nt*fftshift(dtau*fft(ifft(hR_new).*ifft(abs(AT_temp).^2))));

% terms inside the final braket in Eq. (2.25)
temp=AT_temp.*((1-fR)*abs(AT_temp).^2+fR*conv);

% perform derivative in the frequency domain
deriv=fft(-1i*omega.*ifft(temp));
N=ifft(1i*gamma*temp-gamma*tau_shock*deriv);% nonlinear operator

% obtain the right hand side of Eq. (2.31)
R=N.*exp(-D1*z);
R=R(:);
end

% === define function to print ODE integrator status
function status = report(z, y, flag) %
```

```
  status = 0;
  if isempty(flag)
    fprintf('%05.1f %% complete\n', z/distance*100);
  end
end

% === setup and run the ODE integrator
Z = linspace(0, distance, Nz);  % select output z points
% === set error control options
options = odeset('RelTol', 1e-5, 'AbsTol', 1e-12, ...
                 'NormControl', 'on', ...
                 'OutputFcn', @report);

% use ode45 solver to solve for the propagation
AW_ini=ifft(A1);
[Z,AW]=ode45(@rhs,Z,AW_ini,options);
% the solved result AW is actually B defined in Eq. (2.30)

 for i=1:length(Z)
     AW(i,:)=AW(i,:).*exp(D1*Z(i));% convert B to A in freq domain
     AT(i,:)=fft(AW(i,:));% obtain A in time domain
     AW(i,:)=fftshift(AW(i,:))*Nt*dtau;% scale the unit
 end
 omega=ifftshift(omega);% do a final fft shift of omega, which is returned
end
```

Bibliography

[1] Emanuele Galiffi, Romain Tirole, Shixiong Yin, Huanan Li, Stefano Vezzoli, Paloma A Huidobro, Mário G Silveirinha, Riccardo Sapienza, Andrea Alù, and John B Pendry. Photonics of time-varying media. *Advanced Photonics*, 4(1):014002, 2022.

[2] Christophe Caloz and Zoé-Lise Deck-Léger. Spacetime metamaterials—part i: general concepts. *IEEE Transactions on Antennas and Propagation*, 68(3):1569–1582, 2019.

[3] Christophe Caloz and Zoe-Lise Deck-Leger. Spacetime metamaterials—part ii: Theory and applications. *IEEE Transactions on Antennas and Propagation*, 68(3):1583–1598, 2019.

[4] Mahmoud A Gaafar, Toshihiko Baba, Manfred Eich, and Alexander Yu Petrov. Front-induced transitions. *Nature Photonics*, 13(11):737–748, 2019.

[5] Frederic R Morgenthaler. Velocity modulation of electromagnetic waves. *IRE Transactions on Microwave Theory and Techniques*, 6(2):167–172, 1958.

[6] Yonatan Sharabi, Alex Dikopoltsev, Eran Lustig, Yaakov Lumer, and Mordechai Segev. Spatiotemporal photonic crystals. *Optica*, 9(6):585–592, 2022.

[7] Yonatan Sharabi, Eran Lustig, and Mordechai Segev. Disordered photonic time crystals. *Physical Review Letters*, 126(16):163902, 2021.

[8] A Boltasseva, VM Shalaev, and M Segev. Photonic time crystals: from fundamental insights to novel applications: opinion. *Optical Materials Express*, 14(3):592–597, 2024.

[9] Eran Lustig, Ohad Segal, Soham Saha, Colton Fruhling, Vladimir M Shalaev, Alexandra Boltasseva, and Mordechai Segev. Photonic time-crystals-fundamental concepts. *Optics Express*, 31(6):9165–9170, 2023.

[10] Victor Pacheco-Peña and Nader Engheta. Antireflection temporal coatings. *Optica*, 7(4):323–331, 2020.

[11] JT Mendonça, A Guerreiro, and Ana M Martins. Quantum theory of time refraction. *Physical Review A*, 62(3):033805, 2000.

[12] Angus Prain, Stefano Vezzoli, Niclas Westerberg, Thomas Roger, and D Faccio. Spontaneous photon production in time-dependent epsilon-near-zero materials. *Physical Review Letters*, 118(13):133904, 2017.

[13] Vincent Bacot, Matthieu Labousse, Antonin Eddi, Mathias Fink, and Emmanuel Fort. Time reversal and holography with spacetime transformations. *Nature Physics*, 12(10):972–977, 2016.

[14] Hady Moussa, Gengyu Xu, Shixiong Yin, Emanuele Galiffi, Younes Ra'di, and Andrea Alù. Observation of temporal reflection and broadband frequency translation at photonic time interfaces. *Nature Physics*, 19(6):863–868, 2023.

[15] Xuchen Wang, Mohammad Sajjad Mirmoosa, Viktar S Asadchy, Carsten Rockstuhl, Shanhui Fan, and Sergei A Tretyakov. Metasurface-based realization of photonic time crystals. *Science Advances*, 9(14):eadg7541, 2023.

[16] Zhaoli Dong, Hang Li, Tuo Wan, Qian Liang, Zhaoju Yang, and Bo Yan. Quantum time reflection and refraction of ultracold atoms. *Nature Photonics*, 18(1):68–73, 2024.

[17] Yiyu Zhou, M Zahirul Alam, Mohammad Karimi, Jeremy Upham, Orad Reshef, Cong Liu, Alan E Willner, and Robert W Boyd. Broadband frequency translation through time refraction in an epsilon-near-zero material. *Nature Communications*, 11(1):2180, 2020.

[18] Eran Lustig, Ohad Segal, Soham Saha, Eliyahu Bordo, Sarah N Chowdhury, Yonatan Sharabi, Avner Fleischer, Alexandra Boltasseva, Oren Cohen, Vladimir M Shalaev, et al. Time-refraction optics with single cycle modulation. *Nanophotonics*, 12(12):2221–2230, 2023.

[19] BW Plansinis, WR Donaldson, and GP Agrawal. What is the temporal analog of reflection and refraction of optical beams? *Physical Review Letters*, 115(18):183901, 2015.

[20] Thomas G Philbin, Chris Kuklewicz, Scott Robertson, Stephen Hill, Friedrich Konig, and Ulf Leonhardt. Fiber-optical analog of the event horizon. *Science*, 319(5868):1367–1370, 2008.

[21] Karen E Webb, Miro Erkintalo, Yiqing Xu, Neil GR Broderick, John M Dudley, Goëry Genty, and Stuart G Murdoch. Nonlinear optics of fibre event horizons. *Nature Communications*, 5(1):4969, 2014.

[22] SF Wang, Arnaud Mussot, Matteo Conforti, A Bendahmane, XL Zeng, and Alexandre Kudlinski. Optical event horizons from the collision of a soliton and its own dispersive wave. *Physical Review A*, 92(2):023837, 2015.

[23] Brent W Plansinis, William R Donaldson, and Govind P Agrawal. Temporal waveguides for optical pulses. *J. Opt. Soc. Am. B*, 33(6):1112–1119, 2016.

[24] Brent W Plansinis, William R Donaldson, and Govind P Agrawal. Cross-phase-modulation-induced temporal reflection and waveguiding of optical pulses. *J. Opt. Soc. Am. B*, 35(2):436–445, 2018.

[25] JT Mendonça and PK Shukla. Time refraction and time reflection: two basic concepts. *Physica Scripta*, 65(2):160, 2002.

[26] Yuzhe Xiao, Drew N Maywar, and Govind P Agrawal. Reflection and transmission of electromagnetic waves at a temporal boundary. *Optics Letters*, 39(3):574–577, 2014.

[27] Robert W. Boyd. *Nonlinear optics*. Academic Press, 4th edition, 2019.

[28] Govind P Agrawal. *Nonlinear fiber optics*. Academic Press, 6th edition, 2019.

[29] David J Griffiths. *Introduction to electrodynamics*. Cambridge University Press, 2023.

[30] Diego M Solís, Raphael Kastner, and Nader Engheta. Time-varying materials in the presence of dispersion: plane-wave propagation in a lorentzian medium with temporal discontinuity. *Photonics Research*, 9(9):1842–1853, 2021.

[31] Zeki Hayran, Aobo Chen, and Francesco Monticone. Spectral causality and the scattering of waves. *Optica*, 8(8):1040–1049, 2021.

[32] Zoé-Lise Deck-Léger, Nima Chamanara, Maksim Skorobogatiy, Mário G Silveirinha, and Christophe Caloz. Uniform-velocity spacetime crystals. *Advanced Photonics*, 1(5):056002–056002, 2019.

[33] Charles Ciret, François Leo, Bart Kuyken, Gunther Roelkens, and Simon-Pierre Gorza. Observation of an optical event horizon in a silicon-on-insulator photonic wire waveguide. *Optics Express*, 24(1):114–124, 2016.

[34] Sophocles J Orfanidis. *Electromagnetic waves and antennas*. Rutgers University New Brunswick, NJ, 2002.

[35] JJ Sakurai and J Napolitano. *Modern Quantum Mechanics*. Cambridge University Press, 3rd edition, 2021.

[36] Roger H Stolen, James P Gordon, WJ Tomlinson, and Hermann A Haus. Raman response function of silica-core fibers. *J. Opt. Soc. Am. B*, 6(6):1159–1166, 1989.

[37] F DeMartini, CH Townes, TK Gustafson, and PL Kelley. Self-steepening of light pulses. *Physical Review*, 164(2):312, 1967.

[38] N Tzoar and M Jain. Self-phase modulation in long-geometry optical waveguides. *Physical Review A*, 23(3):1266, 1981.

[39] Dan Anderson and Mietek Lisak. Nonlinear asymmetric self-phase modulation and self-steepening of pulses in long optical waveguides. *Physical Review A*, 27(3):1393, 1983.

[40] Keith J Blow and David Wood. Theoretical description of transient stimulated Raman scattering in optical fibers. *IEEE Journal of Quantum Electronics*, 25(12):2665–2673, 1989.

[41] PV Mamyshev and Stanislav V Chernikov. Ultrashort-pulse propagation in optical fibers. *Optics Letters*, 15(19):1076–1078, 1990.

[42] Q Lin and Govind P Agrawal. Raman response function for silica fibers. *Optics Letters*, 31(21):3086–3088, 2006.

[43] John R Dormand and Peter J Prince. A family of embedded runge-kutta formulae. *Journal of Computational and Applied Mathematics*, 6(1):19–26, 1980.

[44] P Tournois. Analogie optique de la compression d'impulsion. *CR Acad. Sci*, 258(15):3839–3842, 1964.

[45] P Tournois, JL Vernet, and G Bienvenu. Sur l'analogie optique de certains montages électroniques: Formation d'images temporelles de signaux électriques. *CR Acad. Sci*, 267:375–378, 1968.

[46] SA Akhmanov, AP Sukhorukov, and AS Chirkin. Nonstationary phenomena and space-time analogy in nonlinear optics. *Sov. Phys. JETP*, 28(4):748–757, 1969.

[47] Keisuke Goda and Bahram Jalali. Dispersive Fourier transformation for fast continuous single-shot measurements. *Nature Photonics*, 7(2):102–112, 2013.

[48] Tomasz Jannson. Real-time Fourier transformation in dispersive optical fibers. *Optics Letters*, 8(4):232–234, 1983.

[49] J Azaña, LR Chen, MA Muriel, and PWE Smith. Experimental demonstration of real-time Fourier transformation using linearly chirped fibre Bragg gratings. *Electronics Letters*, 35(25):2223–2224, 1999.

[50] Brian H Kolner. Active pulse compression using an integrated electro-optic phase modulator. *Applied Physics Letters*, 52(14):1122–1124, 1988.

[51] AA Godil, BA Auld, and DM Bloom. Time-lens producing 1.9 ps optical pulses. *Applied Physics Letters*, 62(10):1047–1049, 1993.

[52] Brian H Kolner. Space-time duality and the theory of temporal imaging. *IEEE Journal of Quantum Electronics*, 30(8):1951–1963, 1994.

[53] José Azaña, Naum K Berger, Boris Levit, and Baruch Fischer. Spectro-temporal imaging of optical pulses with a single time lens. *IEEE Photonics Technology Letters*, 16(3):882–884, 2004.

[54] David J Griffiths and Darrell F Schroeter. *Introduction to Quantum Mechanics*. Cambridge University Press, 2018.

[55] Julien de Rosny and Mathias Fink. Overcoming the diffraction limit in wave physics using a time-reversal mirror and a novel acoustic sink. *Physical Review Letters*, 89(12):124301, 2002.

[56] Amnon Yariv. Three-dimensional pictorial transmission in optical fibers. *Applied Physics Letters*, 28(2):88–89, 1976.

[57] Mehmet Fatih Yanik and Shanhui Fan. Time reversal of light with linear optics and modulators. *Physical Review Letters*, 93(17):173903, 2004.

[58] Fritz Goos and Hilda Hänchen. Ein neuer und fundamentaler versuch zur totalreflexion. *Annalen der Physik*, 436(7-8):333–346, 1947.

[59] Konstantin Y Bliokh, Ilya V Shadrivov, and Yuri S Kivshar. Goos–Hänchen and Imbert–Fedorov shifts of polarized vortex beams. *Optics Letters*, 34(3):389–391, 2009.

[60] Fabien Bretenaker, Albert Le Floch, and Laurent Dutriaux. Direct measurement of the optical Goos-Hänchen effect in lasers. *Physical Review Letters*, 68(7):931, 1992.

[61] Xi Chen, Xiao-Jing Lu, Pei-Liang Zhao, and Qi-Biao Zhu. Energy flux and Goos–Hänchen shift in frustrated total internal reflection. *Optics Letters*, 37(9):1526–1528, 2012.

[62] JS Russell. Report of the 14th meeting of the british association for the advancement of science, york, 1844. 1844.

[63] J. Denschlag, J. E. Simsarian, D. L. Feder, Charles W. Clark, L. A. Collins, J. Cubizolles, L. Deng, E. W. Hagley, K. Helmerson, W. P. Reinhardt, S. L. Rolston, B. I. Schneider, and W. D. Phillips. Generating solitons by phase engineering of a Bose-Einstein condensate. *Science*, 287(5450):97–101, 2000.

[64] Jonathan S Alden, Adam W Tsen, Pinshane Y Huang, Robert Hovden, Lola Brown, Jiwoong Park, David A Muller, and Paul L McEuen. Strain solitons and topological defects in bilayer graphene. *Proceedings of the National Academy of Sciences*, 110(28):11256–11260, 2013.

[65] AM Kosevich, VV Gann, AI Zhukov, and VP Voronov. Magnetic soliton motion in a nonuniform magnetic field. *Journal of Experimental and Theoretical Physics*, 87:401–407, 1998.

[66] Hermann A Haus and William S Wong. Solitons in optical communications. *Reviews of Modern Physics*, 68(2):423, 1996.

[67] Yuri S Kivshar and Govind P Agrawal. *Optical solitons: from fibers to photonic crystals*. Academic press, 2003.

[68] Linn F Mollenauer and James P Gordon. *Solitons in optical fibers: fundamentals and applications*. Elsevier, 2006.

[69] Mark J Ablowitz and Peter A Clarkson. *Solitons, nonlinear evolution equations and inverse scattering*, volume 149. Cambridge University Press, 1991.

[70] Aleksei Shabat and Vladimir Zakharov. Exact theory of two-dimensional self-focusing and one-dimensional self-modulation of waves in nonlinear media. *Sov. Phys. JETP*, 34(1):62, 1972.

[71] Ping Kong Alexander Wai, CR Menyuk, HH Chen, and YC Lee. Soliton at the zero-group-dispersion wavelength of a single-model fiber. *Optics Letters*, 12(8):628–630, 1987.

[72] Y Kodama and K Nozaki. Soliton interaction in optical fibers. *Optics Letters*, 12(12):1038–1040, 1987.

[73] Chandrasekhara Venkata Raman. A new radiation. *Indian Journal of Physics*, 2:387–398, 1928.

[74] RW Hellwarth. Third-order optical susceptibilities of liquids and solids. *Progress in Quantum Electronics*, 5:1–68, 1977.

[75] N Tang and RL Sutherland. Time-domain theory for pump–probe experiments with chirped pulses. *J. Opt. Soc. Am. B*, 14(12):3412–3423, 1997.

[76] James P Gordon. Theory of the soliton self-frequency shift. *Optics Letters*, 11(10):662–664, 1986.

[77] J Santhanam and Govind P Agrawal. Raman-induced spectral shifts in optical fibers: general theory based on the moment method. *Optics Communications*, 222(1-6):413–420, 2003.

[78] Lev Davidovich Landau and Evgenii Mikhailovich Lifshitz. *Quantum mechanics: non-relativistic theory*, volume 3. Elsevier, 2013.

[79] Nikolaos K Efremidis, Zhigang Chen, Mordechai Segev, and Demetrios N Christodoulides. Airy beams and accelerating waves: an overview of recent advances. *Optica*, 6(5):686–701, 2019.

[80] S Robertson and U Leonhardt. Frequency shifting at fiber-optical event horizons: the effect of Raman deceleration. *Physical Review A*, 81(6):063835, 2010.

[81] Andriy V Gorbach and Dmitry V Skryabin. Light trapping in gravity-like potentials and expansion of supercontinuum spectra in photonic-crystal fibres. *Nature Photonics*, 1(11):653–657, 2007.

[82] Norihiko Nishizawa and Toshio Goto. Characteristics of pulse trapping by use of ultrashort soliton pulses in optical fibers across the zero-dispersion wavelength. *Optics Express*, 10(21):1151–1159, 2002.

[83] Norihiko Nishizawa and Toshio Goto. Pulse trapping by ultrashort soliton pulses in optical fibers across zero-dispersion wavelength. *Optics Letters*, 27(3):152–154, 2002.

[84] Weibin Wang, Hua Yang, Pinghua Tang, Chujun Zhao, and Jing Gao. Soliton trapping of dispersive waves in photonic crystal fiber with two zero dispersive wavelengths. *Optics Express*, 21(9):11215–11226, 2013.

[85] Dane R Austin, C Martijn de Sterke, Benjamin J Eggleton, and Thomas G Brown. Dispersive wave blue-shift in supercontinuum generation. *Optics Express*, 14(25):11997–12007, 2006.

[86] S Hill, CE Kuklewicz, U Leonhardt, and F König. Evolution of light trapped by a soliton in a microstructured fiber. *Optics Express*, 17(16):13588–13601, 2009.

[87] Dmitry V Skryabin and Andrey V Gorbach. Colloquium: Looking at a soliton through the prism of optical supercontinuum. *Reviews of Modern Physics*, 82(2):1287, 2010.

[88] Rodislav Driben, Fedor Mitschke, and Nickolai Zhavoronkov. Cascaded interactions between Raman induced solitons and dispersive waves in photonic crystal fibers at the advanced stage of supercontinuum generation. *Optics Express*, 18(25):25993–25998, 2010.

[89] Di Zhu, Changchen Chen, Mengjie Yu, Linbo Shao, Yaowen Hu, CJ Xin, Matthew Yeh, Soumya Ghosh, Lingyan He, Christian Reimer, et al. Spectral control of nonclassical light pulses using an integrated thin-film lithium niobate modulator. *Light: Science & Applications*, 11(1):327, 2022.

[90] Laura J Wright, Michał Karpiński, Christoph Söller, and Brian J Smith. Spectral shearing of quantum light pulses by electro-optic phase modulation. *Physical Review Letters*, 118(2):023601, 2017.

[91] Petr Hlubina, Marcin Szpulak, Dalibor Ciprian, Tadeusz Martynkien, and Wacław Urbańczyk. Measurement of the group dispersion of the fundamental mode of holey fiber by white-light spectral interferometry. *Optics Express*, 15(18):11073–11081, 2007.

[92] TM Kardaś and Czesław Radzewicz. Broadband near-infrared fibers dispersion measurement using white-light spectral interferometry. *Optics Communications*, 282(22):4361–4365, 2009.

[93] A Demircan, Sh Amiranashvili, and Gunter Steinmeyer. Controlling light by light with an optical event horizon. *Physical Review Letters*, 106(16):163901, 2011.

[94] RL Fork, OE Martinez, and JP Gordon. Negative dispersion using pairs of prisms. *Optics Letters*, 9(5):150–152, 1984.

[95] Ewelina Majda-Zdancewicz, Marek Suproniuk, M Pawłowski, and M Wierzbowski. Current state of photoconductive semiconductor switch engineering. *Opto-Electronics Review*, 26(2):92–102, 2018.